UNIVERSITÀ DEGLI STUDI DI TRIESTE

XXIX CICLO DEL DOTTORATO DI RICERCA IN

Scienze della terra e meccanica dei fluidi

Modelling Techniques to Monitor Injection of Carbon Dioxide in Deep Saline Aquifers

Settore scientifico-disciplinare: **Geo/11 - Geofisica Applicata**

DOTTORANDO / A
Federico Da Col

COORDINATORE
PROF. Pierpaolo Omari

SUPERVISORE DI TESI
PROF. Aldo Vesnaver

CO-SUPERVISORI DI TESI
PROF. José Maria Carcione
DOTT. Davide Gei

ANNO ACCADEMICO 2015/2016

Contents

List of Figures

Chapter 1

Motivation - A Partial Solution to Global Warming

There is strong scientific evidence that human activities are interacting with the biogeochemistry of our planet, as stated in the latest report from the Intergovernmental Panel on Climate Change (Tignor et al. (2013)). In fact, emissions of carbon dioxide have a relevant impact on the carbon cycle. The main effects of this are an increase of global average temperatures, which has accelerated in the past two decades, as shown in 1.1 (a). Most of the heat has been absorbed by the oceans, leading to thermal expansion, which combined with the increased melting of the glaciers (see, for example, the global glacier inventory by Arendt et al. (2012))) give place to the rise in average sea level shown in Figure 1.1 (b). Furthermore, dissolution of the CO_2 in the sea water causes a decrease in the pH of the oceans, with harsh consequences on the biosphere (Falkowski et al. (2000)). Emissions of CO_2 occur mainly because of human activities which involve burning of fossil fuels; since these remain the main source of energy (Tignor et al. (2013), Figure 1.1 (c)), a reduction of the emissions looks unlikely in the foreseeable future. It has been assessed that CO_2 is by far the largest contributor to forcing the energy balance of the planet (see Figure 1.2.2).

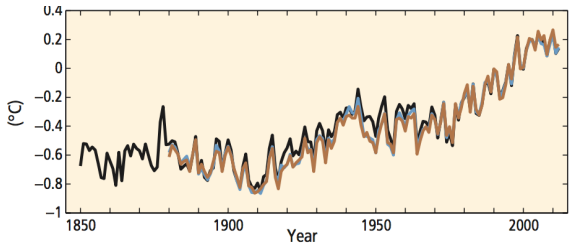

(a) Variation of global mean temperatures

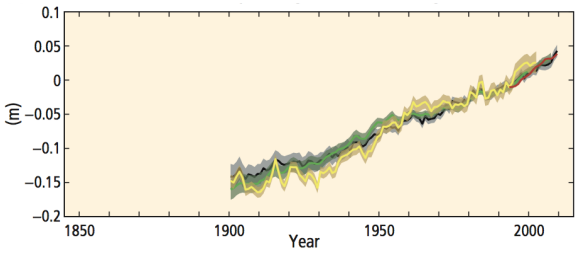

(b) Variation in global average sea level

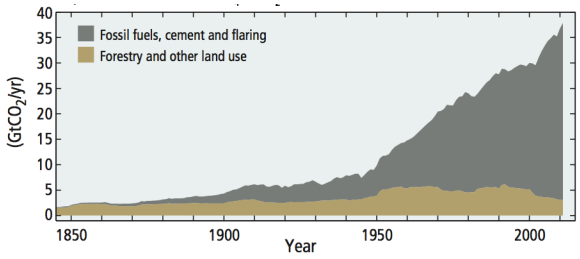

(c) Global anthropogenic CO_2 emissions

Figure 1.1: Plots of the (a) variation of average surface temperature, (b) sea level and (c) anthropogenic CO_2 yearly emissions. After Tignor et al. (2013)

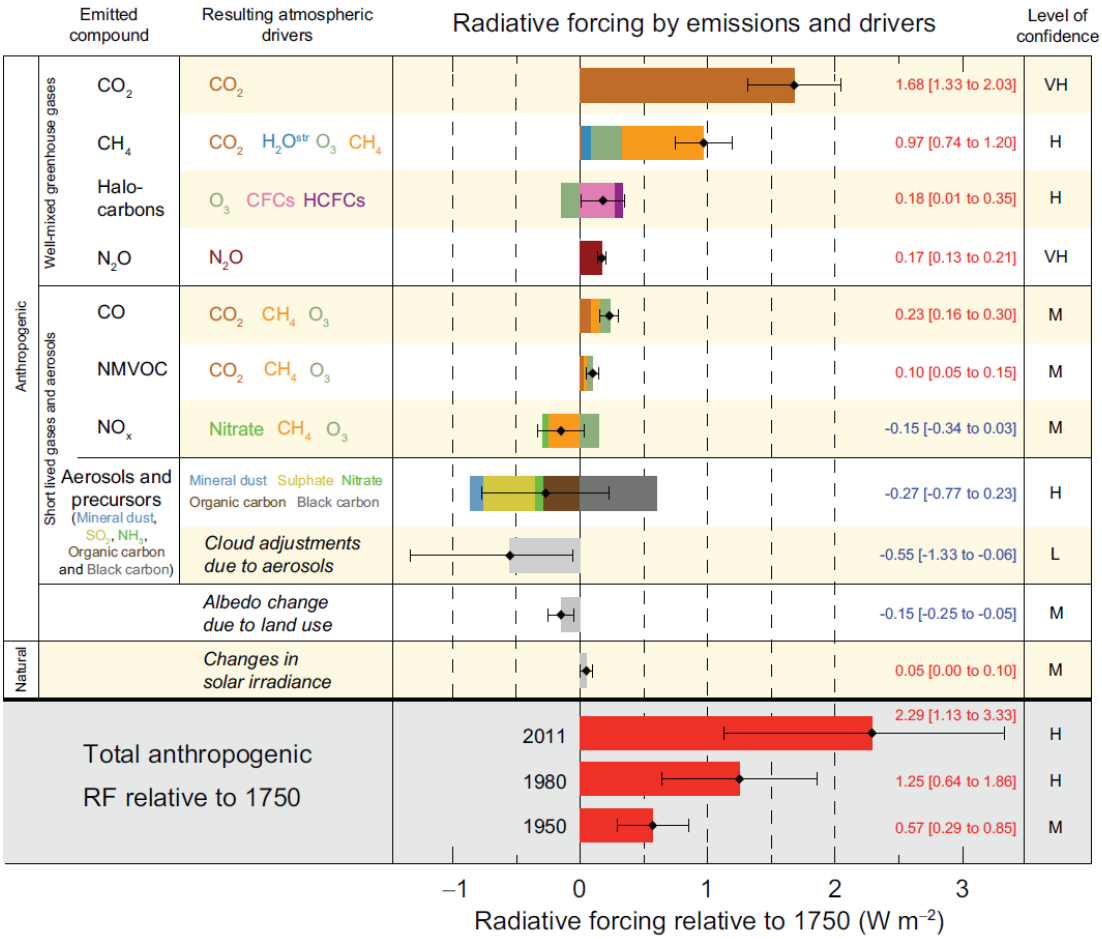

Figure 1.2: Main drivers in forcing the energy balance of the Earth and level of confidence (vh = very high (>95%), h = high (>80%), m = medium (>66%) and l=low (<33%)). CO_2 is the largest contributor. After Tignor et al. (2013), chapter 8

For this reason, other options have been explored to compensate, at least partially, for the excess carbon. Carbon can be stored by means of several biological and chemical reactions; for instance, reforestation and wetland restoration are two efficient ways to remove carbon from the atmosphere using the biological reactions inside the vegetation (Bonan (2008)). Another, yet more questionably effective solution, is to encourage growth of phytoplankton and algae by fertilising the ocean with iron or urea (Smetacek et al. (2012); Matear and Elliott (2004)).

Finally, injecting CO_2 in deep geological formations has been proven to be a viable solution several years ago (see for example, Zweigel et al. (2004) and Arts et al. (2004)). Three main target formations have been identified (Friedmann (2007)):

- unminable coal seams (Bromhal et al. (2005), Shi and Durucan (2005)). *Enhanced coalbed methane recovery* produce producing the methane stored in the microporous coal by injecting CO_2 in the coalbed. This will be adsorpted by the coal, leading to a desorption of the methane, which will therefore become free. As a consequence, unless the coal is mined, the CO_2 will be stored safely for very long periods of time. It has been pointed out

that the amount of CO_2 stored may be negligible when compared to that in deep saline aquifers and not significant to fight climate change.

- depleted oil and gas reservoirs (Holloway (2001), Kovscek and Wang (2005)). Studies on the effects of injection of CO_2 in oil and gas fields date back to well before the scientific community became interested in carbon sequestration. In fact, some oil and gas fields may need injection of fluids to increase pressure and improve the amount of extractable hydrocarbon (*Enhanced Oil/Gas Recovery*). One of the most commonly used fluids is supercritical CO_2, most of which will remain in the reservoir after the end of the operations. Therefore, even though it does not present the highest storage capacity, the profitability of the method makes it one the most viable options for carbon storage

- deep saline aquifers (Pruess and Garcia (2002),Bruant et al. (2002)), which have the highest storage potential and are treated extensively in this thesis.

What concerns the most when it comes to carbon sequestration are the chances of leakages, which would vanish our efforts to remove it from the atmosphere as well as constitute an environmental and health hazard. In the case of geological repositories, the main threat is that overpressure could lead to fracturing of the caprock, letting the CO_2 flow upwards and acidify shallower, possibly freshwater aquifers, or even reach the surface. It is therefore essential to monitor the propagation of the CO_2 plume and the fractures it generates. The presence of CO_2 causes significant changes in the properties of the bulk. In fact, it is very resistive, making electromagnetic methods a viable tool to detect its presence. Furthermore, it alters the elastic properties of the medium (Carcione et al. (2006), Carcione et al. (2012)), leading to significant changes in seismic velocities. It is therefore possible to detect the presence of carbon dioxide in a brine-saturated formation by means of seismic experiments. In order to do this, deep understanding of the physics and chemistry involved in the process are necessary. In this thesis we present modelling techniques of all steps of a carbon storage experiment. In Chapter 2 we present the physical principles and the numerical solutions to model two-phase flow and the physical and chemical processes which trap the CO_2 permanently in the aquifer. Furthermore, the algorithm used to compute synthetic seismograms accounting for the anelasticity in presence of two fluids is outlined. Then, in Chapters 3 and 4, two examples are presented.

In the first, carbon dioxide is injected in a complex, heterogenous aquifer, part of an anticlinal structure, in which two wells are drilled. The injection is simulated using a commercial finite-difference solver. The seismic velocities and attenuation factors are then computed using White's mesoscopic theory. The monitoring is performed by means of a cross-hole seismic experiment. The synthetic seismograms are computed with a full-wave solver and we detect the velocity anomalies by means of a tomographic inversion of direct waves.

Chapter 4 presents a synthetic example of a passive seismic monitoring technique. The aim is to map the presence of CO_2 by detecting the location of micro-cracks emitting seismic energy.

In fact, overpressure due to the presence of the carbon dioxide may lead to a sharp decrease in the stiffness of the medium, which can then fail, emitting energy in the form of seismic waves. Pressure build-up is simulated with a semi-analytical solution. After determining time, location and intensity of the microseismic sources, the propagation of the waves is computed with a viscoelastic code. Finally, we present a reverse-time migration focusing algorithm to re-locate these sources and therefore the CO_2 plume.

Chapter 2

Physical Principles

2.1 Flow in Porous Media

2.1.1 One-Phase Flow

Henry Darcy was an engineer in charge of studying the development of water supply for the city of Dijon, France, in year 1856. In particular his aim was to improve the efficiency of the sand filters for water purification. He therefore set up an apparatus consisting of a cylindrical tank, filled with sand, with a nozzle on the bottom and a tank full of water on top of it, as schematically shown in figure 2.1. He then changed the size of the grains composing the sand, measuring the variations of the flux in the nozzle. He came to the conclusion that the flux would be proportional to the cross-sectional area of the sand container times the loss in piezometric head, divided by the height of the sandbox.

$$Q \propto A\frac{\Delta h}{L}. \tag{2.1}$$

We define the seepage velocity, or Darcy velocity, as the ratio between the flux and sectional area of the nozzle. The constant of proportionality K is then the hydraulic conductivity

$$u = \frac{Q}{A} = K\frac{\Delta h}{L}. \tag{2.2}$$

As stated above, in Darcy's law we consider the piezometric head, instead of the hydraulic head , since we assume that seepage velocities are low enough to consider the kinetic energy as negligible. This is a common assumption when it comes to reservoir modelling. See, for example, Peaceman (2000)

$$H = Z + \frac{p}{\rho g} + \frac{v^2}{2g} \simeq Z + \frac{p}{\rho g} = h. \tag{2.3}$$

A modern notation of Darcy's law makes use of the intrinsic permeability κ of the medium as

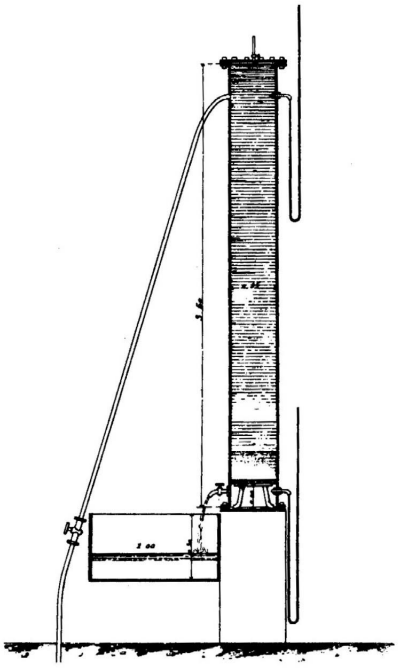

Figure 2.1: Schematic representation of a Darcy flow, after Darcy (1856).

a constant of proportionality. It is experimentally proven that (Nutting (1930))

$$\frac{K}{\rho g} = \kappa\eta, \tag{2.4}$$

where η is the viscosity of the fluid. Darcy's law becomes then, in 3D

$$\overline{u} = -\frac{\overline{\overline{\kappa}}}{\eta}\left(\nabla p - \rho\overline{g}\right); \tag{2.5}$$

Here the the intrinsic permeability $\overline{\overline{\kappa}}$ is a 3x3 symmetrical tensor, accounting for the possible anisotropy of the medium.

$$\begin{bmatrix} \kappa_{xx} & \kappa_{yx} & \kappa_{zx} \\ \kappa_{yx} & \kappa_{yy} & \kappa_{zy} \\ \kappa_{zx} & \kappa_{zy} & \kappa_{zz} \end{bmatrix} \tag{2.6}$$

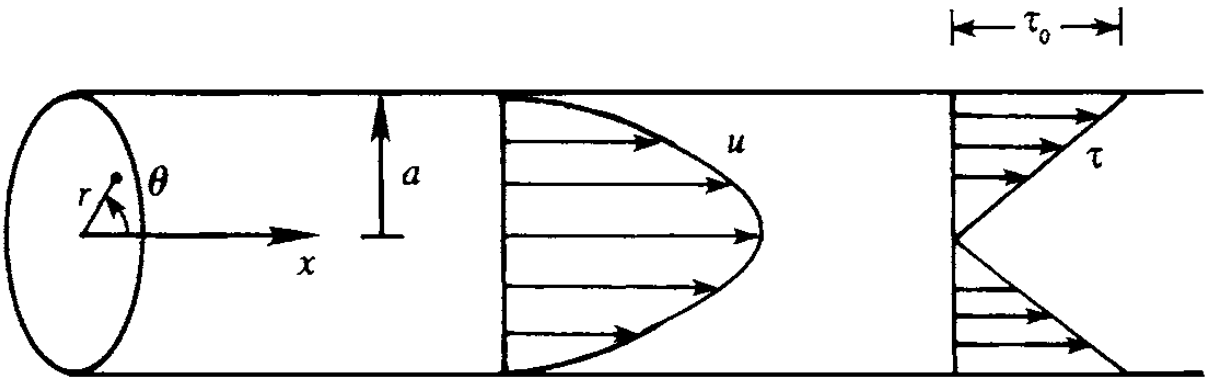

Figure 2.2: Velocity and shear stress profiles for a laminar flow in a infinitely long tube. From Kundu and Cohen (2004)

We note how this equation is very similar to the solution of a laminar flow in a tube, where the average velocity over the cross section is

$$u_{avg} = -\frac{a^2}{8\eta}\frac{dp}{dx}, \tag{2.7}$$

which is the Darcy velocity with $\kappa = R^2/8$. Therefore, a Darcy flow, like the flow in an infinitely long tube, is the result of a balance between forces due to a pressure gradient and viscous forces.

2.1.2 Two-Phase Flow

In a porous medium where more than one fluid is present, saturation will be defined as the ratio between the partial porosity ϕ_γ and the total porosity ϕ. By partial porosity we mean the quantity for which the volume occupied by a certain fluid, identified by the subscript γ, is $\phi_\gamma d\Omega$. Of course, the sum of all partial porosities has to be equal to the total porosity $\phi = \sum_\gamma \phi_\gamma$. Assuming the medium is fully saturated, the sum of the saturations of all the fluids present will have to be equal to 1.

$$S_\gamma = \frac{\phi_\gamma}{\phi}; \quad \sum_{\gamma=1}^{n_{\text{fluids}}} S_\gamma = 1 \tag{2.8}$$

Whenever we have a simultaneous flow of two fluids inside a porous medium, each fluid establishes its own stable flow paths, or channels. Moreover, for each degree of saturation we have a different set of channels; if the the saturation of one of the two fluids drops below a certain threshold, then the channels relative to the flow of that fluid will break down, making the flow impossible. This qualitative description can be described by Darcy's law. In fact, the two fluids will have two different seepage velocities, since the medium will have different permeabilities for each of the two fluids. In order to model this, we have to introduce the concept of wetting and non-wetting phase fluid. Whenever a liquid is placed on a solid and is surrounded by gas, two interfaces form; one between the liquid and the gas and one between

the liquid and the solid, as shown in Figure 2.3. When equilibrium is reached, the forces acting on the drop to spread it on the solid, smooth surface and the opposing cohesive forces balance each other. From this, it is possible to derive that

$$\cos\theta = \frac{\gamma_{gs} - \gamma_{ls}}{\gamma_{lg}}, \tag{2.9}$$

where γ indicates the surface tension between the non-wetting and solid phases (subscript gs), solid and wetting phase fluid (subscript ls) and wetting and non-wetting phase fluids (subscript lg). If the adhesive forces prevail and the liquid drop spreads on the surface, then θ<90° and the surface is said to be wettable by the fluid. Otherwise, if the cohesive forces prevail and each liquid particle is more attracted by its neighbouring liquid particles than by the solid surface, then θ<90° and the surface is said to be non-wettable. For instance, water on glass has a contact angle of approximately 20°, while mercury on glass 150°.

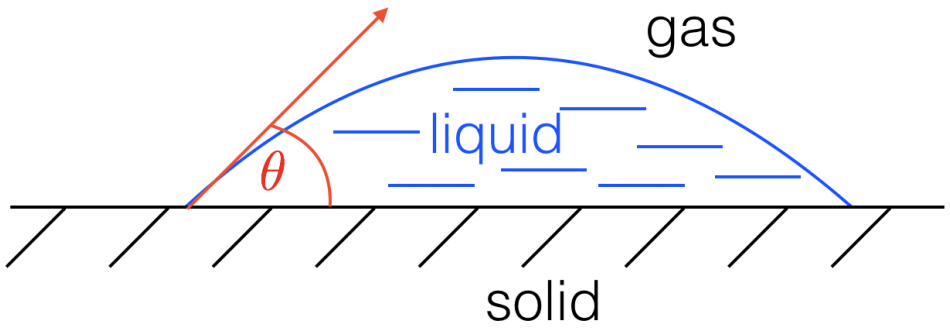

Figure 2.3: Schematic representation of the contact angle between the solid and liquid phases, in presence of gas.

Inside a capillary tube, the wetting phase fluid, that is, the fluid which wets the solid surface more, is that towards which the concavity points, as shown in figure 2.4
The solid matrix of the rock will react differently to the flow of each of the two fluids, giving place to two different Darcy velocities. Following, among others, Peaceman (2000), and indicating with subscripts l and g the wetting and non-wetting phase fluid respectively, we can therefore write

$$\overline{u_l} = -\frac{\kappa_l \overline{\overline{k}}}{\eta_l} \left(\nabla p_l - \rho_l \overline{g}\right), \tag{2.10}$$

$$\overline{u_g} = -\frac{\kappa_g \overline{\overline{k}}}{\eta_g} \left(\nabla p_g - \rho_g \overline{g}\right), \tag{2.11}$$

where κ_g and κ_l are the wetting- and non-wetting phase relative permeabilities respectively.

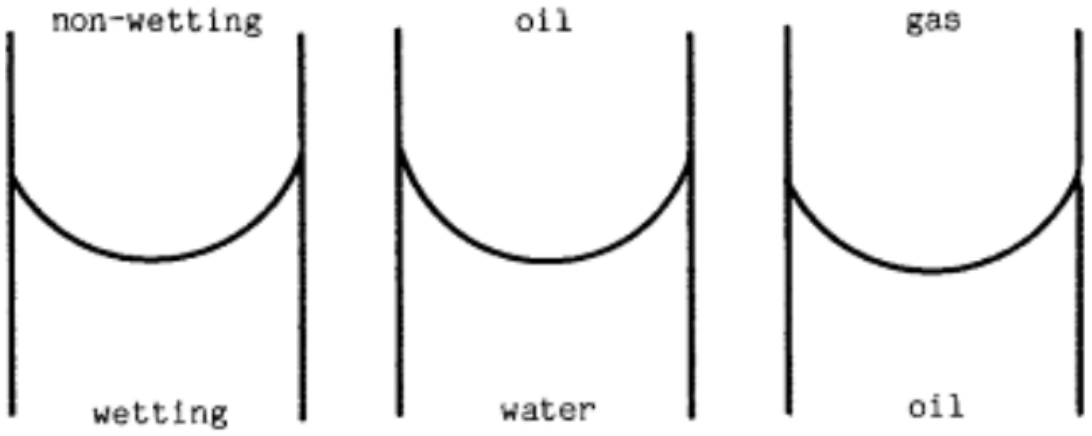

Figure 2.4: Schematic representation of the interface between a wetting and non wetting phase fluid in a capillary tube (after Chavent and Jaffré (1986)).

Following Peaceman (2000), we accept as an experimental fact that these are a function of saturation only and define them as the ratio between the effective permeability to each of the two fluids and the intrinsic permeability of the medium κ.

$$\kappa_g = \frac{\kappa_{eg}}{\kappa} \leq 1 \qquad \kappa_l = \frac{\kappa_{el}}{\kappa} \leq 1 \tag{2.12}$$

When two immiscible fluids come in contact inside a capillary tube or in small pores, the pressure of the non-wetting phase fluid is higher than that of the wetting one. In fact, at the curved interface which forms between them, interfacial tensions give place to the capillary pressure.

$$p_c = p_g - p_l = \frac{2\gamma_{lg}\cos\theta}{r}, \tag{2.13}$$

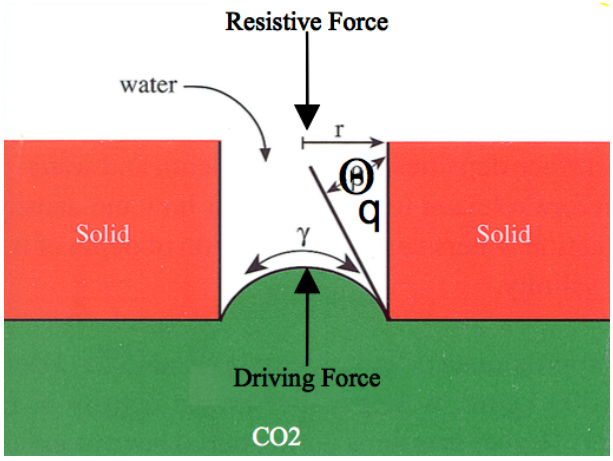

Figure 2.5: Schematic representation of a pore throat in which two fluids are present. After Christopher et al. (2006)

where the interfacial tension between the two fluids γ_{lg} depends on the density difference between the fluids involved, θ is the contact angle between the non-wetting phase fluid and the solid skeleton of the pore and r is the radius of the pore throat. If the "driving force" of the non-wetting phase fluid is greater than the force due to capillary pressure, then it will flow into the pore. This threshold pressure is called capillary entry pressure. In figure 2.5 one can see a graphical representation of this phenomenon.

The relations between capillary pressure and relative permeability with saturation are determined experimentally and several models have been implemented over time to fit them (see, among others, Brooks and Corey (1964), Bruce (1972), Millington and Quirk (1961),Kunze et al. (1968)). In this thesis we use Van Genuchten's (Van Genuchten (1980)). It has been assessed that this model describes rather well the sands and shaly mudstones of the Utsira formation in the Sleipner field (White et al. (2012), Mathias et al. (2009)), on which our synthetic models are based. Van Genuchten's is a four-parameter model, which in the formulation of STOMP software used in this thesis (White et al. (2012), section 2.2) writes as

$$S_e = \frac{S - S_{lr}}{1 - S_{lr}} = \left(\left(1 + \alpha \frac{\sigma^*}{\sigma_{nw}} \left(\frac{P_n - P_w}{\rho_w g} \right) \right)^n \right)^{-m}, \tag{2.14}$$

S_e is defined as the effective saturation, S_{lr} is the residual aqueous saturation, α is the capillary entry head, equivalent to the capillary entry pressure, but expressed in terms of hydraulic head; $h_n = \frac{P_n - P_w}{\rho_w g}$ is the capillary pressure head. σ^* is a reference interfacial tension to remove dimensions from interfacial tension σ_{nw}. Under the Mualem approximation (Mualem (1976b),Mualem (1976a)) the parameter $n = 1 - 1/m$. The relative permeability curves are instead given by

$$\kappa_{r\gamma} = (S_e)^{\frac{1}{2}} \left[1 - \left(1 - (S_e)^{\frac{1}{m}} \right)^m \right]^2, \quad \beta = l, g. \tag{2.15}$$

An example of capillary pressure and relative permeability curves is shown in Figure 2.6.

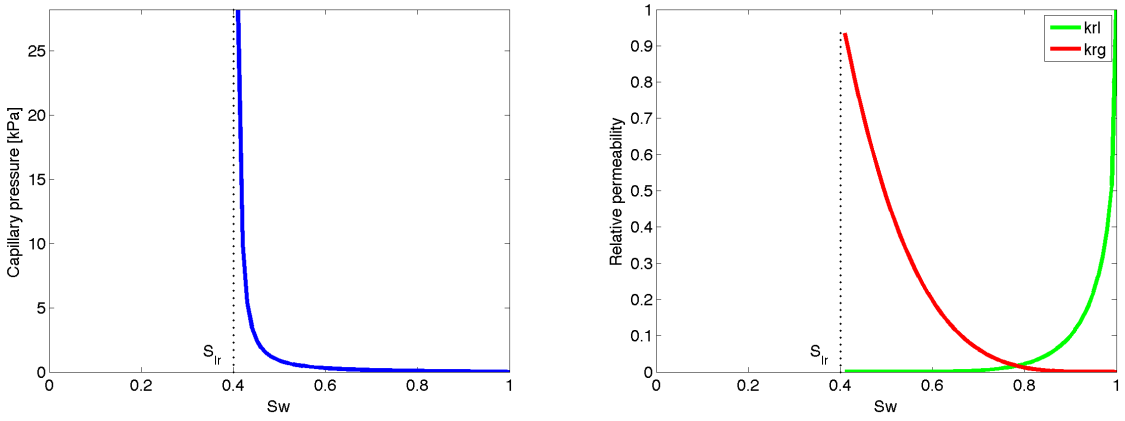

(a) Capillary pressure

(b) Relative permeability

Figure 2.6: Example of typical capillary pressure (a) and relative permeability curves (b) for sandstones.

2.2 STOMP

2.2.1 Conservation Equations

The simulator called Subsurface Transport over Multiple Phases, developed by Mark D. White et al. at the Pacific Northwest National Laboratories, is a finite difference solver of the two-phase flow problem for injection of CO_2 in brine-saturated aquifers. Assuming isothermal conditions, it solves three coupled conservation equations: one for water, one for CO_2 and one for the salt ($NaCl$). Both water and CO_2 are assumed to exist in liquid (γ=l) and gas state (γ=g)

$$\frac{\partial}{\partial t}\left[\sum_{\gamma=l,g}\left(\phi\rho_\gamma S_\gamma \omega_\gamma^i\right)\right] = -\sum_{\gamma=l,g}^{i}\nabla\left(\rho_\gamma\omega_\gamma u_\gamma\right) + \nabla\left(J_\gamma^i\right) + \sum_{\gamma=l,g}\left(\omega_\gamma^i m_\gamma\right), \qquad (2.16)$$

$$\text{for i=}H_20, CO_2 \quad \text{and } j=l, g$$

where ω is the mass fraction of water, u is the Darcy velocity given in equation 2.10, m_γ accounts for eventual sources and J_γ^i accounts for the molecular diffusion, due to concentration gradients, of both the CO_2 in the brine and of vapour in the CO_2:

$$J_\gamma^i = -\phi\rho_\gamma S_\gamma \frac{M^i}{M_\gamma}\left(\tau_\gamma D_\gamma^i\right)\nabla\chi_\gamma^i, \quad \text{for i=}H_20, CO_2, \qquad (2.17)$$

where M is the molecular weight, τ_γ is the tortuosity, D is the diffusion coefficient and χ is the mole fraction. As for salt, STOMP assumes that it is present dissolved in the aqueous phase (l) or precipitated as a solid (s).

$$\frac{\partial}{\partial t}\left[\phi\rho_l s_l\omega_l^s + \phi\rho_p s_p\right] = -\nabla\left(\rho_l\omega_l^s V_l\right) - \nabla\left(J_l^s\right) + \omega_l^s m_l \qquad (2.18)$$

The mass fraction ω_g is computed in the case more than one phase is present at a node. In fact, in STOMP-CO2 three phase conditions are possible: i) aqueous saturated without entrapped gas ii) aqueous and mobile gas iii) aqueous and entrapped gas. Phase equilibria calculations are performed for temperatures up to 100°C following the formulations of Spycher et al. (2003). Plots of the H_2O mole fraction in the gas phase and CO_2 mole fraction in the aqueous phase are shown in Figure 2.2.1 as a function of pressure at 50°C, 90°C and 130°C for a salt mass fraction of 0.1.

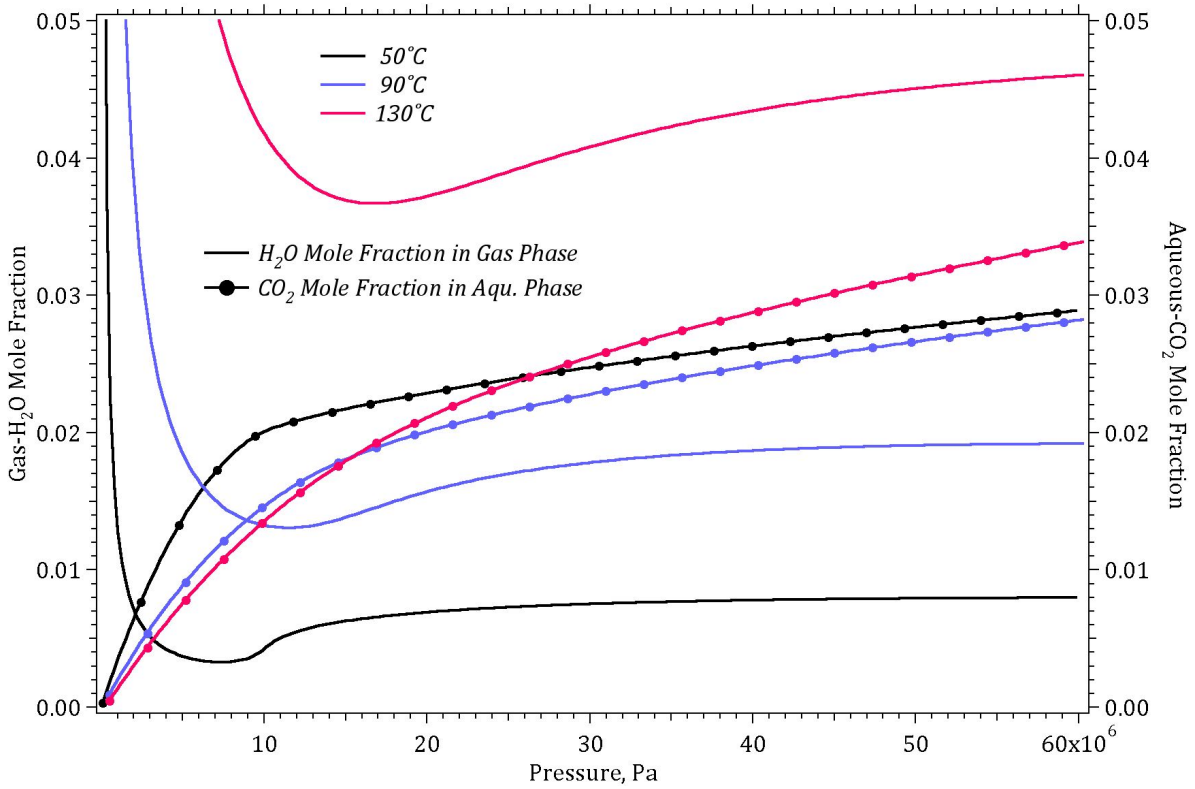

Figure 2.7: Plots of the H_2O mole fraction in the gas phase and CO_2 mole fraction in the aqueous phase for a salt mass fraction of 0.1. Curves for temperatures of 50°C, 90°C and 130°C are shown. After White et al. (2012)

2.2.2 Phase properties

Aqueous density is computed in two steps; first, pure water density is computed as a function of temperature and pressure following the formulation of Meyer et al. (1993). A graph of this formulation for temperatures of 50°C, 90°C and 130°C is shown in Figure 2.8.

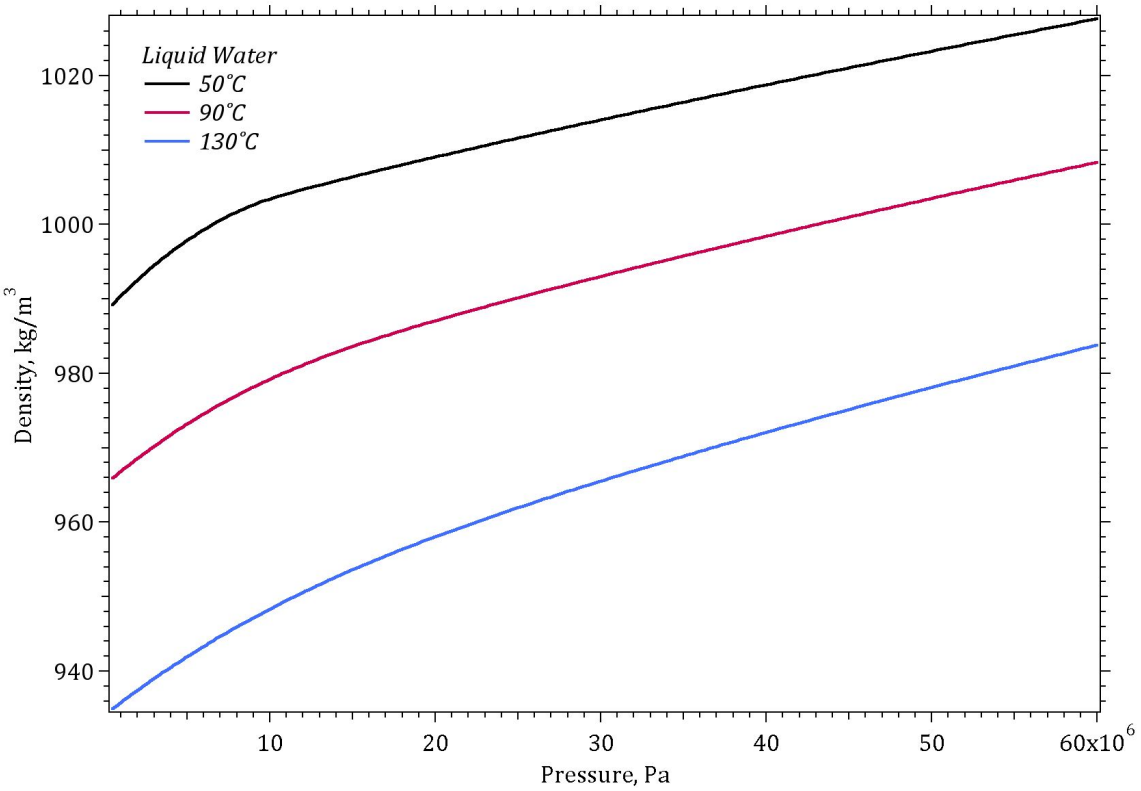

Figure 2.8: Liquid density of pure water as a function of pressure at temperatures of 50°C, 100°C and 150°C. After White et al. (2012)

This is then corrected for the presence of dissolved salt using the formulation of Haas and John (1976). The resulting density profiles as a function of pressure for different values of temperature and salinity are shown in Figure 2.9

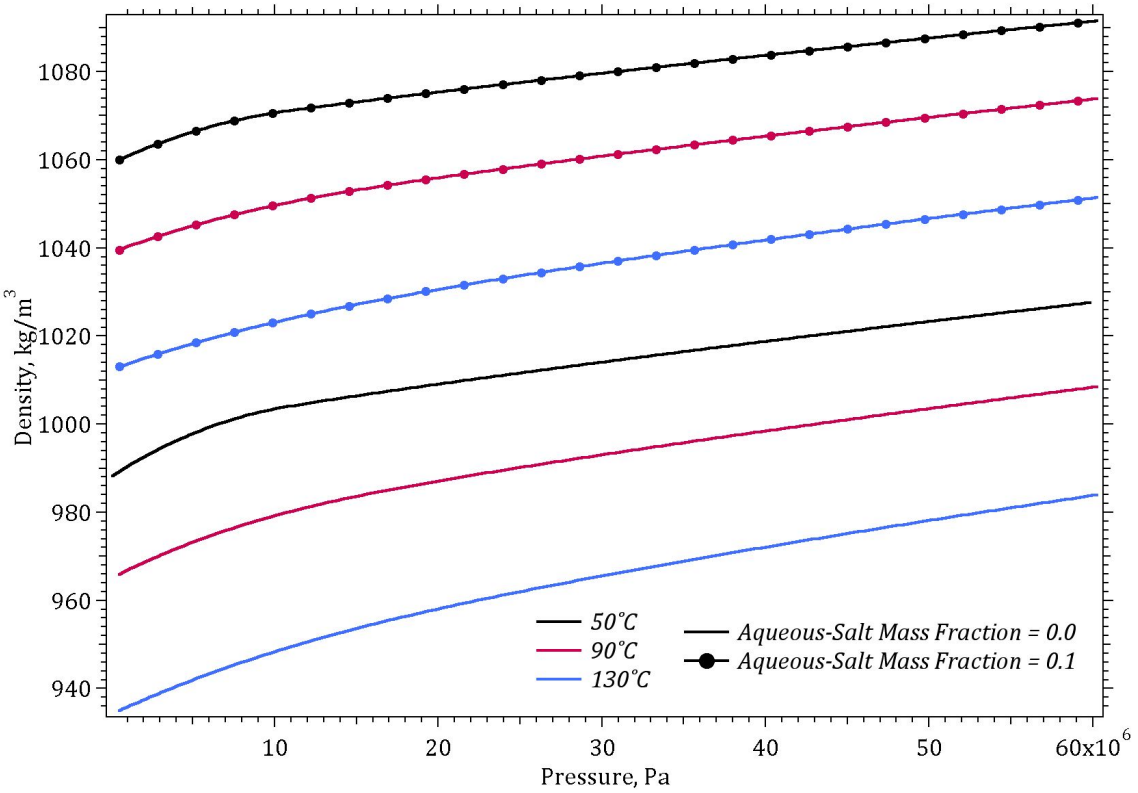

Figure 2.9: Aqueous density as a function of pressure for salt mass fraction of 0.0 and 0.1 at temperatures of 50°C, 90°C and 130°C. After White et al. (2012)

Gas phase densities are computed as the average of pure CO_2 and pure water vapor densities, weighted over the gas mass fraction ω_g

$$\rho_g = \omega_g^{CO_2}\rho_g^{CO_2} + \omega_g^{H_2O}\rho_g^{H_2O}, \tag{2.19}$$

The CO_2 density is computed from a thermodynamic property table, based on the equation of state developed by Span and Wagner (1996). It includes all possible states of the CO_2: subcritical liquid, subcritical gas and supercritical gas up to temperatures of 1100 K and pressures of 800 MPa. A plot of the CO_2 property table used by STOMP can be seen in Figure 2.2.2. The pure water vapour densities, as for pure water, are computed following the steam table formulation by Meyer et al. (1993). The equilibrium densities as a function of temperature in the range 55-145°C and at a constant pressure of 10 MPa are shown in 2.2.2

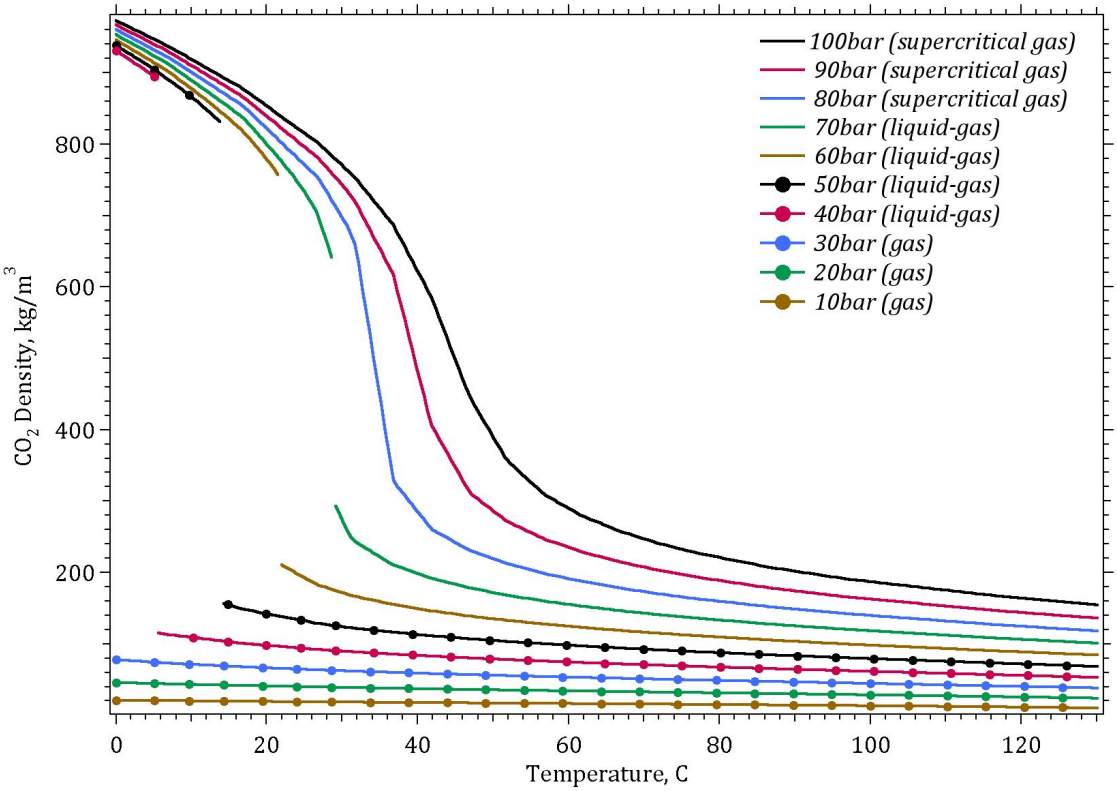

Figure 2.10: CO_2 density as a function of temperature and pressure. After White et al. (2012)

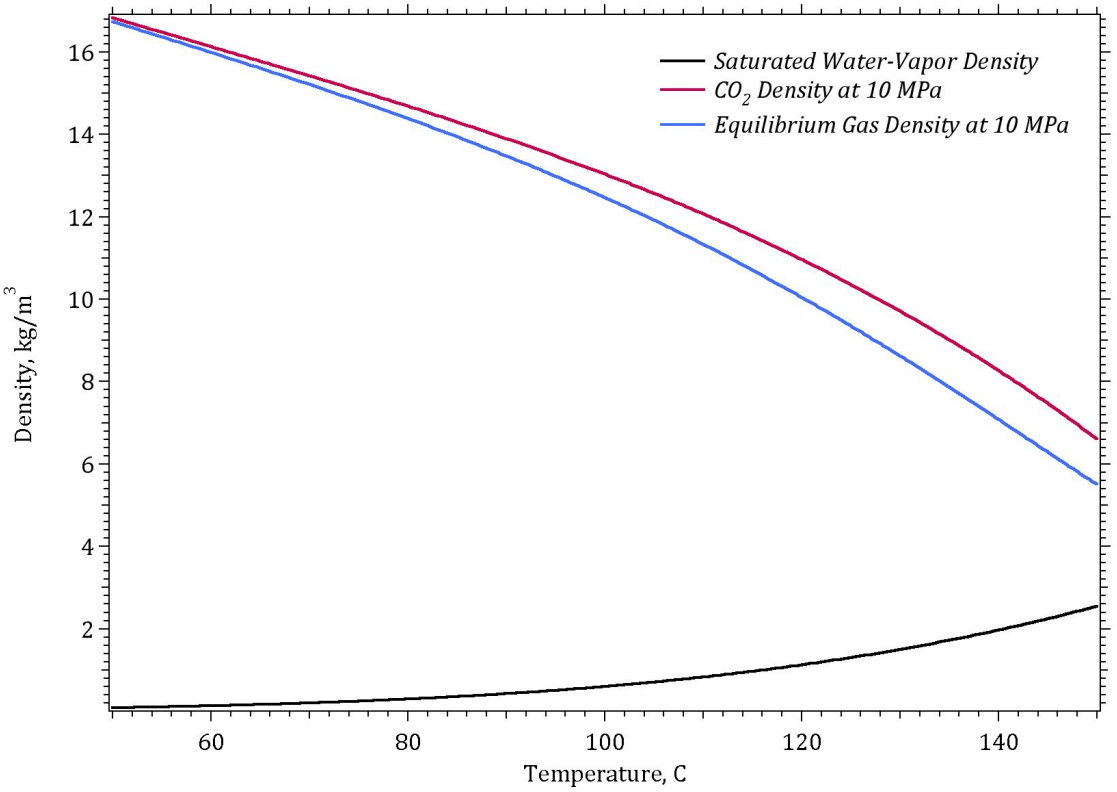

Figure 2.11: Water vapor and gas density as a function of temperature at a constant pressure of 10 MPa. After White et al. (2012)

2.3 Trapping mechanisms

The aim of carbon storage is to irreversibly trap excessive carbon dioxide in the subsurface. This is possible thanks to physical processes and chemical reactions which happen in the aquifer during and after the injection period. Four main mechanisms have been identified, which are unique to saline aquifers and therefore make these formations the most promising for carbon storage; structural, dissolution, capillary and mineral trapping. In this thesis we want to model for times which go from the onset of the injection to a few years after its termination. Therefore only the first three trapping mechanisms will be considered, since these contribute significantly to store the carbon dioxide in the timespan of our interest, while the chemical reactions which lead to precipitation of the CO_2 as mineral occur several hundred thousands of years after the injection has ended. In this section we present the physics of these trapping mechanisms and a few, synthetic, examples simulated with STOMP.

2.3.1 Structural Trapping

A good structural trap for CO_2 storage has similar characteristics to those of a hydrocarbon reservoir. These can be summarised as (Christopher et al. (2006)): i) To increase interfacial tensions and therefore capillary entry pressure, it should be saturated with brine, ii) To contrast buoyancy forces of the lower-density CO_2 it should have small pore throats, i.e. high capillary entry pressure, iii) It should have very low permeability, iv) It should be thick, v) It should not be faulted and laterally continuos, vi) It should be lithologically homogenous. An example of a formation suitable for CO_2 storage is the Sleipner field, which has now been actively used for carbon storage for 18 years and has therefore been widely studied. Its geology has been well characterised by Chadwick et al. (2004) and Arts et al. (2008). The seismic section and its interpretation are shown in figure 2.12. The formation in which the CO_2 is injected is the Utsira sandstone, approximately 280 m thick (top at 820 m and bottom at 1100 m b.s.l.), while the main caprock consists of a silty mudstone layer approximately 200 m thick. The properties of the two rocks are reported in table 2.1, where C_s is the grain compressibility and ρ_s is the grain density.

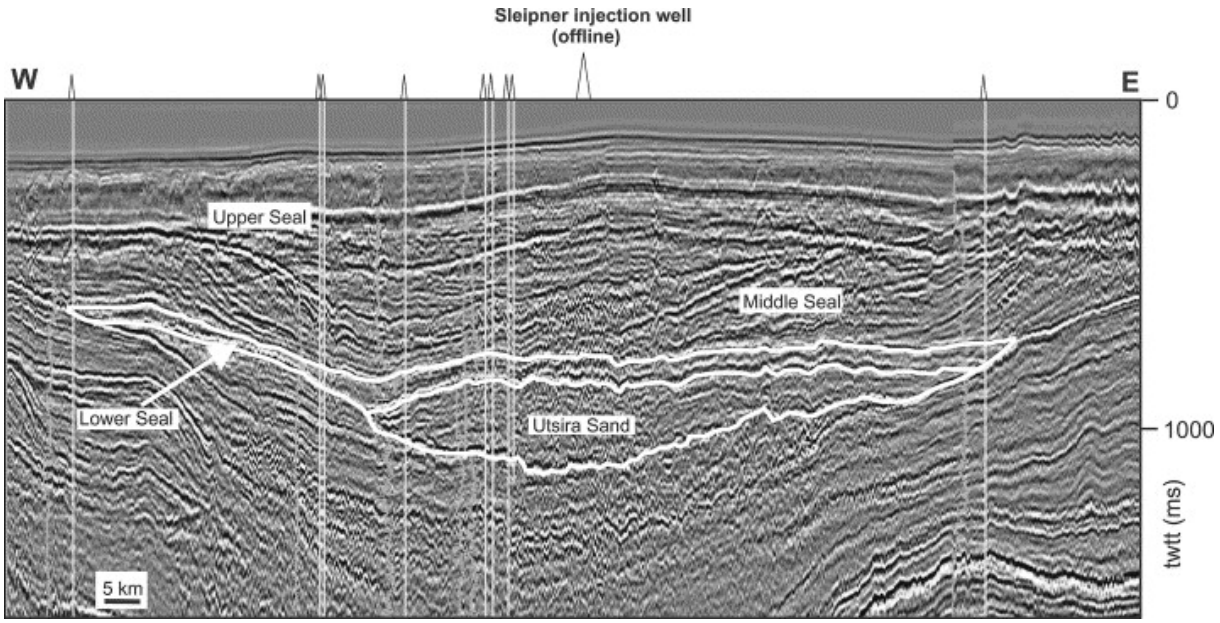

Figure 2.12: Interpreted seismic section of the Utsira sands and the three successive layers of shales acting as caprocks. After Chadwick et al. (2004)

Table 2.1: Properties of the two main rock formations in the Sleipner field.

Rock Type	ϕ	k [D]	Sand/shale ratio	C_s [1/GPa]	ρ_s [kg/m^3]
Sand	0.36	3	0.7-1-0	0.45	2650
Shale	0.10	0.01	0.14	0.45	2650

As an example and as a benchmark test for the STOMP software a simulation was setup in which the conditions of the Sleipner field are considered. The geology has been schematically reproduced as a sandstone formation 180 m thick, in which three very thin (2.5 m) silty mudstone layers are present, as shown in figure 2.14 (a).

Capillary entry heads were set to α=2.735 1/m and 0.140 1/m, for the sandstone and shaly mudstone respectively, equivalent to 62 kPa and 3.5 kPa. For both rocks, van Genuchten parameter n was set to 1.667, which under the Mualem pore distribution approximation gives m=1-1/n=0.4, while residual aqueous saturation was set to 0.2. A plot of the capillary pressure and relative permeability curves is shown in Figure 2.13. Initial conditions were thought to be hydrostatic, with the bottom of the formation at z_b 1120 m b.s.l, assuming an average brine density ρ_b=1040 kg/m^3 we get a pressure P_b=$\rho g z_b$=1.14 MPa. Temperature was considered constant along the entire formation at 37°C. Boundary conditions were set to be Dirichlet for pore pressure at the Western and Eastern boundaries, while no-flow was set at the top and bottom. Pure CO_2 was injected at a rate of 0.1585 kg/s at point x = 0 m and at a height from the bottom of the formation of 22 m, as shown in figure 2.14 (a). In figure 2.14 (b), (c) and (d) gas saturation after 1 month, 1 year and 2 years is displayed. Evidently, the structural trap of

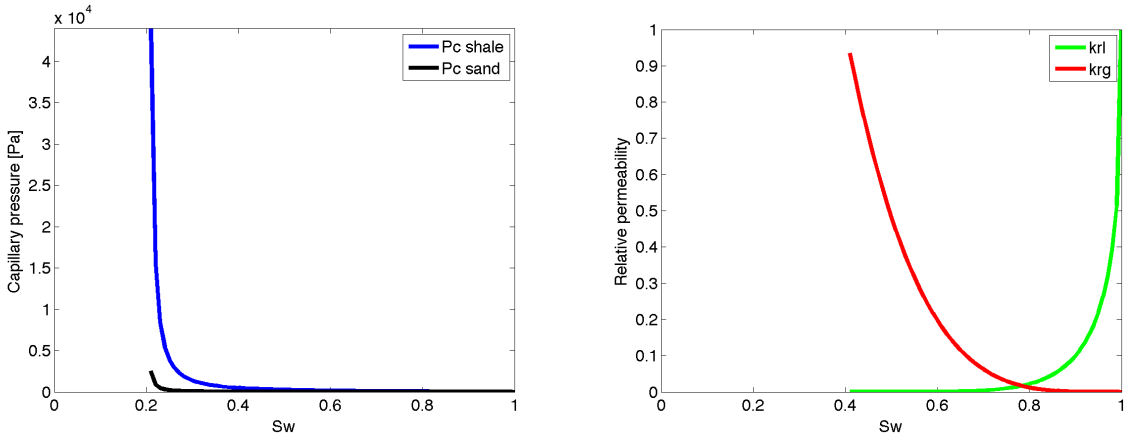

(a) Capillary pressure

(b) Relative permeability

Figure 2.13: Plots of the (a) capillary pressure and (b) relative versus saturation curves used in the simulation.

the very thin, brine saturated, silty musdstone layer, with its very thin pore throats and low permeability was able to confine the buoyant CO_2. We then performed a sensitivity test of the algorithm to a variation of a factor 2 of the capillary entry head parameter in the mudstone layers. In 2.15 (a) we see the capillary pressure curves, while in (b), (c) and (d) we see how the increased size of the pore throats leads to a lower sealing capacity since the CO_2 is now able to migrate to the top of the formation, where the no-flow boundary condition is set.

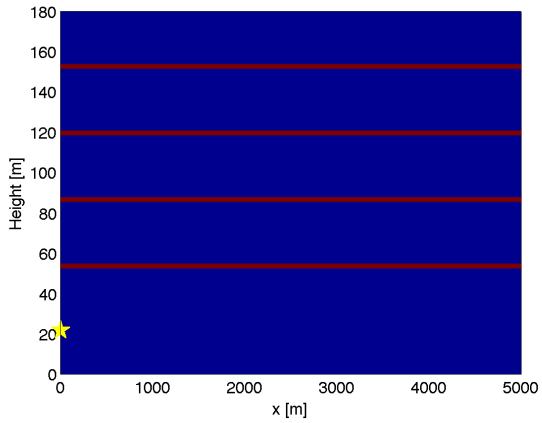

(a) Gas saturation after one month

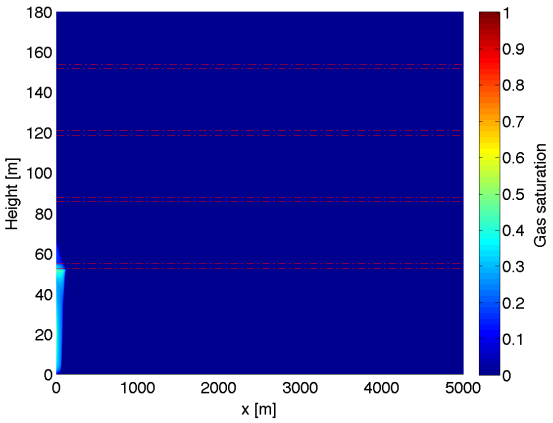

(b) Gas saturation after one month

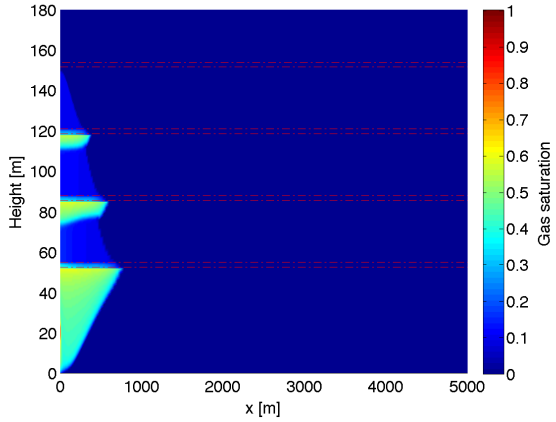

(c) Gas saturation after one year

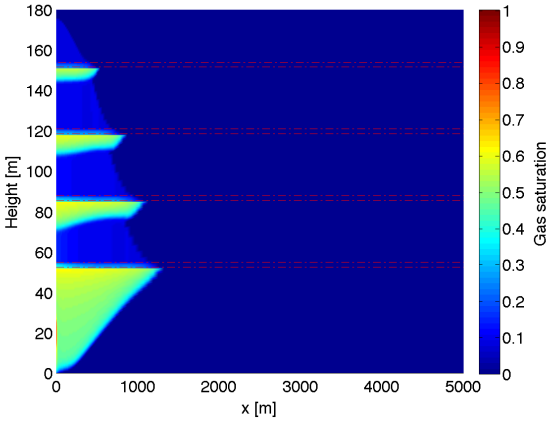

(d) Gas saturation after two years

Figure 2.14: (a) geological setting; the red lines indicate the thin shaly mudstone layers and the star the location of the source. Plots of the gas saturation 30 days (b), 1 year (c) and 2 years (d) after the onset of injection. The dashed red lines indicate the mudstone layers.

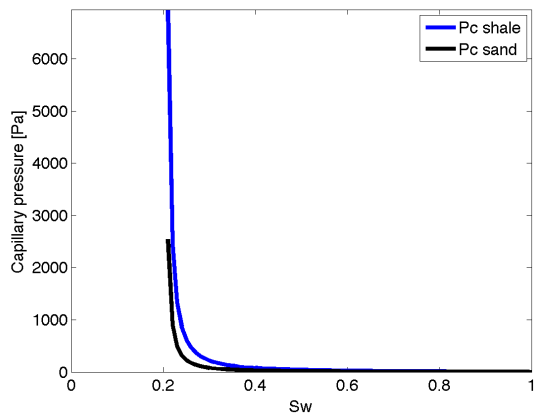

(a) Capillary pressure curves

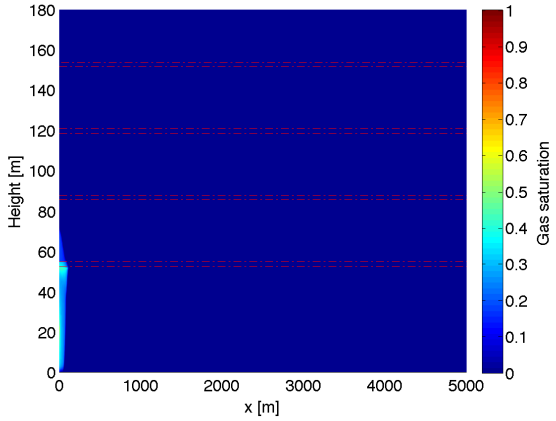

(b) Gas saturation after one month

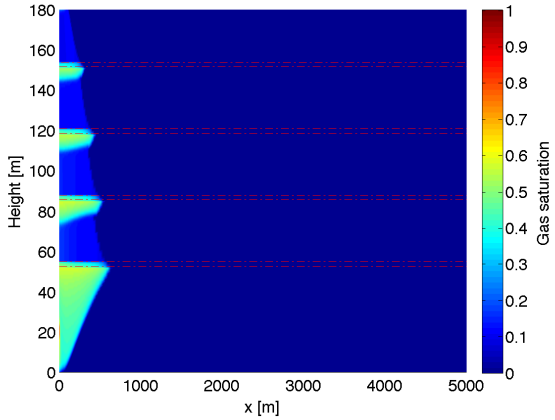

(c) Gas saturation after one year

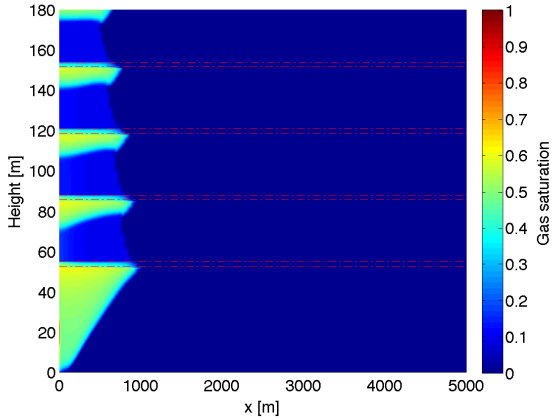

(d) Gas saturation after two years

Figure 2.15: Same plots as in figure 2.15, but with the α parameter increased by a factor of 2 in the shaly mudstone layers. Evidently, the increased size of the pore throats leads to a lower sealing capacity of the mudstone layers.

2.3.2 Capillary Trapping

In section 2.1.1 we presented the capillary pressure and relative permeability curves as a function of saturation. We now have to stress the fact that capillary processes are irreversible. In fact, the curves are hysteretic, that is, different curves apply whether we consider drainage or imbibition processes. This is significant for geological storage of CO_2. In fact, during the injection period we have a drainage-like process in which the carbon dioxide displaces the brine and creates a continuos plume. After the end of the injection, however, the buoyant CO_2 continues to migrate upwards and laterally while the brine invades the CO_2 plume in an imbibition-like process disconnecting it and isolating it into small bubbles and ganglia, which are virtually immobile (Juanes et al. (2006), Hunt et al. (1988)). The gas saturation will therefore be given by the sum of the mobile gas and the trapped gas saturation $S_g = S_{gm} + S_{gt}$. Kumar et al. (2005) found that capillary trapping may be the most important mechanism to store CO_2 in deep saline

aquifers. Hysteresis of the gas relative permeability curve affects the most our simulations. In fact, while also the liquid phase relative permeability curve is hysteretic, since we are dealing with media which are strongly water wet, liquid phase relative permeability can be neglected (Juanes et al. (2006), Oak et al. (1990)). The capillary pressure curve also shows strong hysteresis, however, at the reservoir scale considered in this work its effects are negligible, since the characteristic capillary lengths are much smaller than the grid resolution (Juanes et al. (2006)). Considering only gas-phase relative permeability hysteresis, the most used trapping model is Land's (Land (1968)) which computes the trapped gas saturation S_{gt} as

$$S_{gt} = \frac{S_{gt}}{1 + CS_{gi}}, \tag{2.20}$$

where S_{gi} is the gas saturation at the onset of the reversal imbibition process and C is the Land trapping coefficient, which is computed as

$$C = \frac{1}{S_{gt,max}} - \frac{1}{s_{g,max}} \tag{2.21}$$

where $S_{g,max}$is the maximum gas saturation and $S_{gt,max}$ is the maximum trapped gas saturation. These parameters are clearly presented in 2.16 (a), where the hysteretic gas relative permeability curve used in the following example is shown.

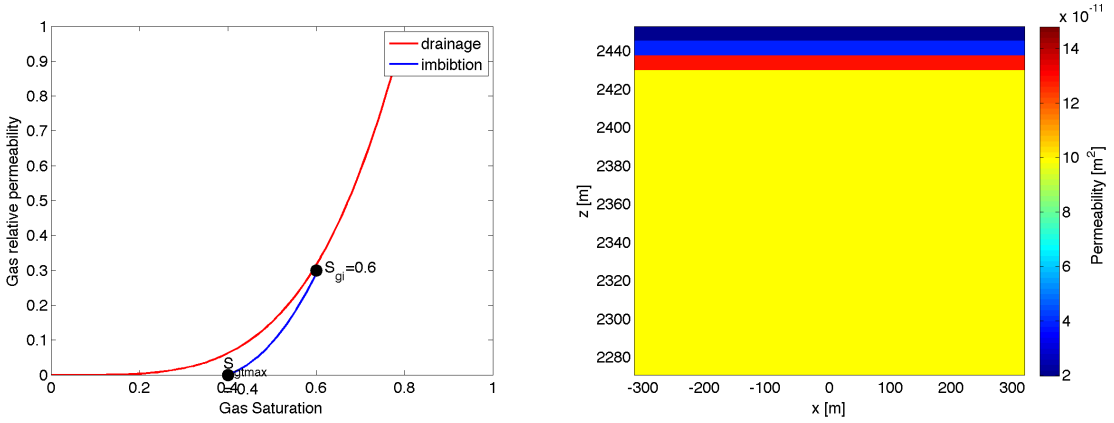

(a) Hysteretic gas relative permeability curve

(b) Permeability cross-section

Figure 2.16: (a) Hysteretic gas relative permeability curve used in the capillary trapping simulation. (b) Cross-section of the formation showing the layering of the permeability.

STOMP is capable of simulating capillary trapping due to the hysteresis of the gas relative permeability curve as in Land's model. We setup a simulation on a 3D domain, consisting of a homogenous aquifer, 650 x 650 m wide in the horizontal directions and 180 m thick. Top of the formation is at 2260 m b.s.l., while the bottom is at 2440 m b.s.l.. The medium is divided with a regular grid of 11 x 11 x 23 nodes. In the horizontal direction, nodes have a spacing of 91 m, except the two nodes closest to the injection well, at x = y = 0, which have a size of

0.2 m. In the vertical direction node spacing is 15 m. Porosity is supposed to be 0.13 on the entire domain, while an impermeable seal is set at the top of the formation as shown in 2.16 (b). Initial conditions are hydrostatic, assuming an average brine density of 1040 kg/m^3. No-flow conditions are set to all boundaries. We inject pure supercritical CO_2 for 2 years at a rate of 21 kg/s from a well at the centre-bottom of the formation. The maximum trapped gas saturation is set to 0.4, as shown in Figure 2.16 (Bennion et al. (2006), experimental data from Pentland et al. (2011) confirm these quantities are reasonable) and the Land C parameter is set to 1.

In figure 2.3.2 one can see a gas saturation and gas trapped saturation at time t=2, 10, 80 and 200 years after the onset of injection. Results confirm that during the injection, capillary trapping may not occur, while its importance is evident already 10 years after the start of the injection, when the brine migrates back. The maximum trapped gas saturation is reached between 50 and 100 years, remaining almost constant even after 200 years, confirming the effectiveness of this irreversible process.

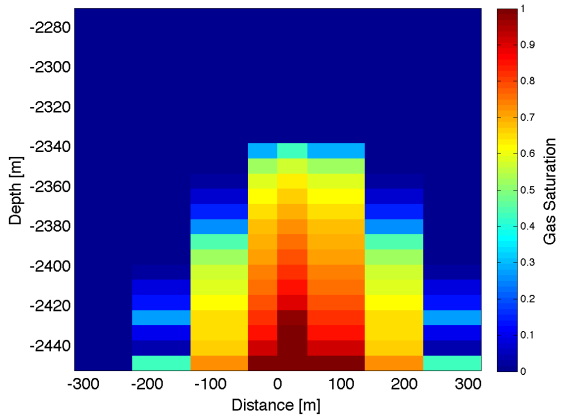

(a) Gas Saturation t=2y

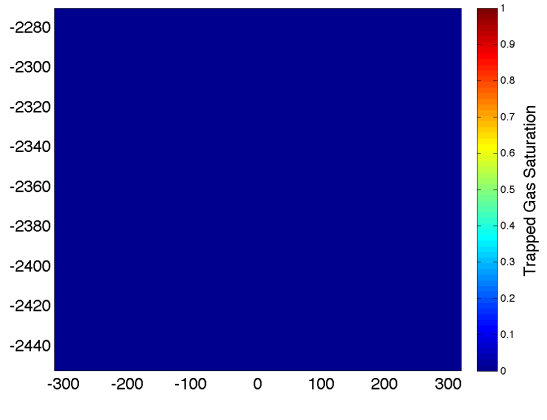

(b) Trapped Gas Saturation t=2y

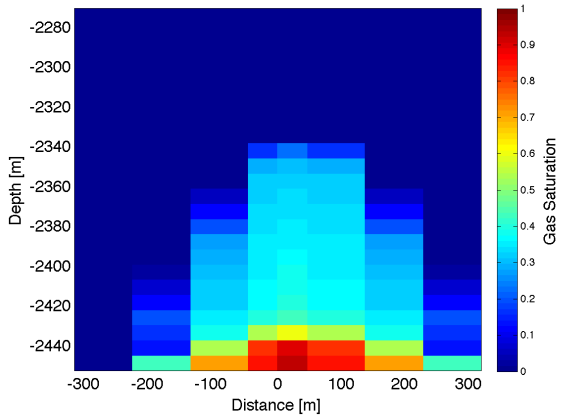

(c) Gas Saturation t=10y

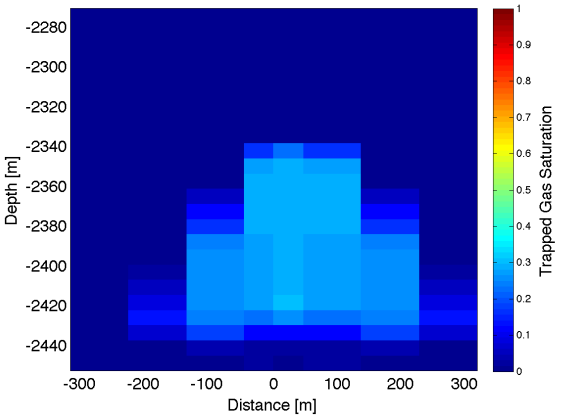

(d) Trapped Gas Saturation t=10y

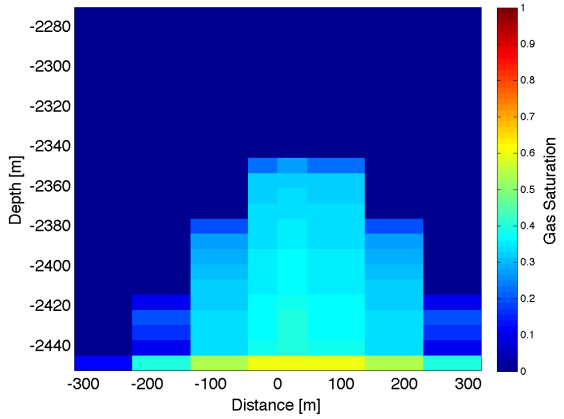

(e) Gas Saturation t=80y

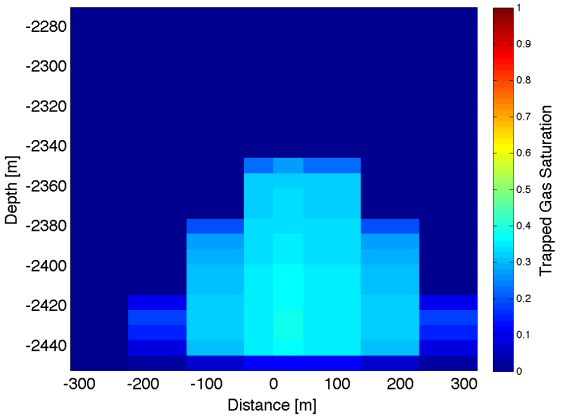

(f) Trapped Gas Saturation t=80y

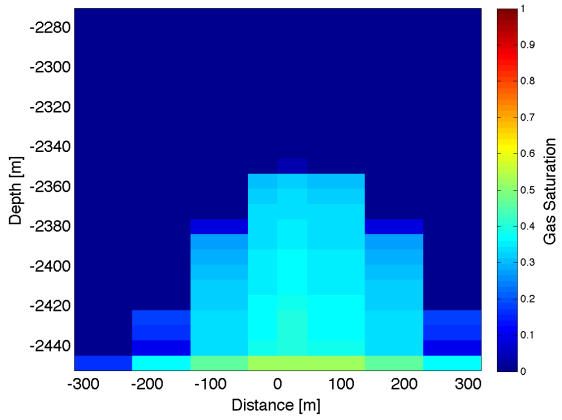

(g) Gas Saturation t=200y

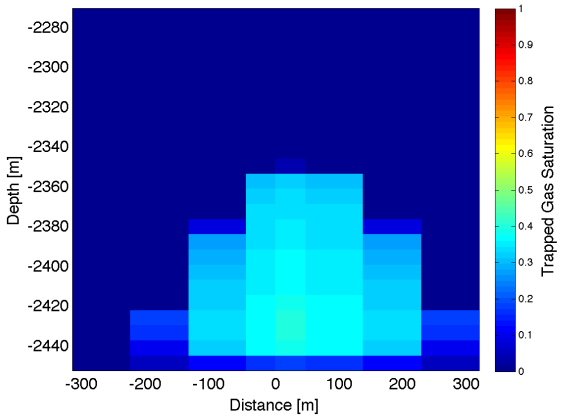

(h) Trapped Gas Saturation t=200y

Figure 2.17: Cross section of the x=y=0 plane showing the gas saturation (a),(c),(e),(g) and trapped gas saturation (b),(d),(f),(h), at the end of the injection (t=2yr) and 10, 80 and 200 years after the onset of the injection.

2.3.3 Dissolution Trapping

Finally, another trapping mechanism, unique to saline aquifers, is the so-called dissolution trapping, due to the dissolution of the CO_2 in the brine by molecular diffusion, following equation 2.17. Ennis-King et al. (2005b) find three main stages at which dissolution plays a role in trapping the CO_2. During the injection the amount of carbon dioxide which will dissolve in the brine will depend mostly on the relative permeability curves and most of all on the residual aqueous saturation, since molecular diffusion will occur mostly in the residual brine. Then, because of buoyancy, it will migrate upwards, until it reaches the caprock; here, in a time of the order of a hundred years (Ennis-King et al. (2005a)), the brine will saturate with carbon dioxide, triggering a density instability. In fact, CO_2 is one of the very few gases which, when dissolved, increases the density of the brine (Moore et al. (1982) observe a 1 % increase). The convective mixing will occur in the form of viscous "fingers" flowing from the caprock downwards. STOMP is able to model this; we setup a simulation in a formation consisting of an homogenous aquifer, 180 m thick and 5500 m wide, with a shaly seal. The properties of the rocks are the same as in the example of structural trapping in section 2.1. The capillary pressure relative permeability curves are Van Genuchten's, with values for α of 2.735 m^{-1} and 0.158 m^{-1} for sands and shales respectively. The residual aqueous saturation is set to 0.4 and the pore size distribution index n to 1.667. We assume initial hydrostatic conditions and no-flow boundary conditions are set at all margins. We inject pure CO_2 for 3 years at a rate of 50 T/yr. In 2.18 we plot the evolution of the aqueous density with time. One can see the buoyant carbon dioxide migrating upwards, reaching the caprock and then the onset of the convective density instability, with the formation of the viscous fingers.

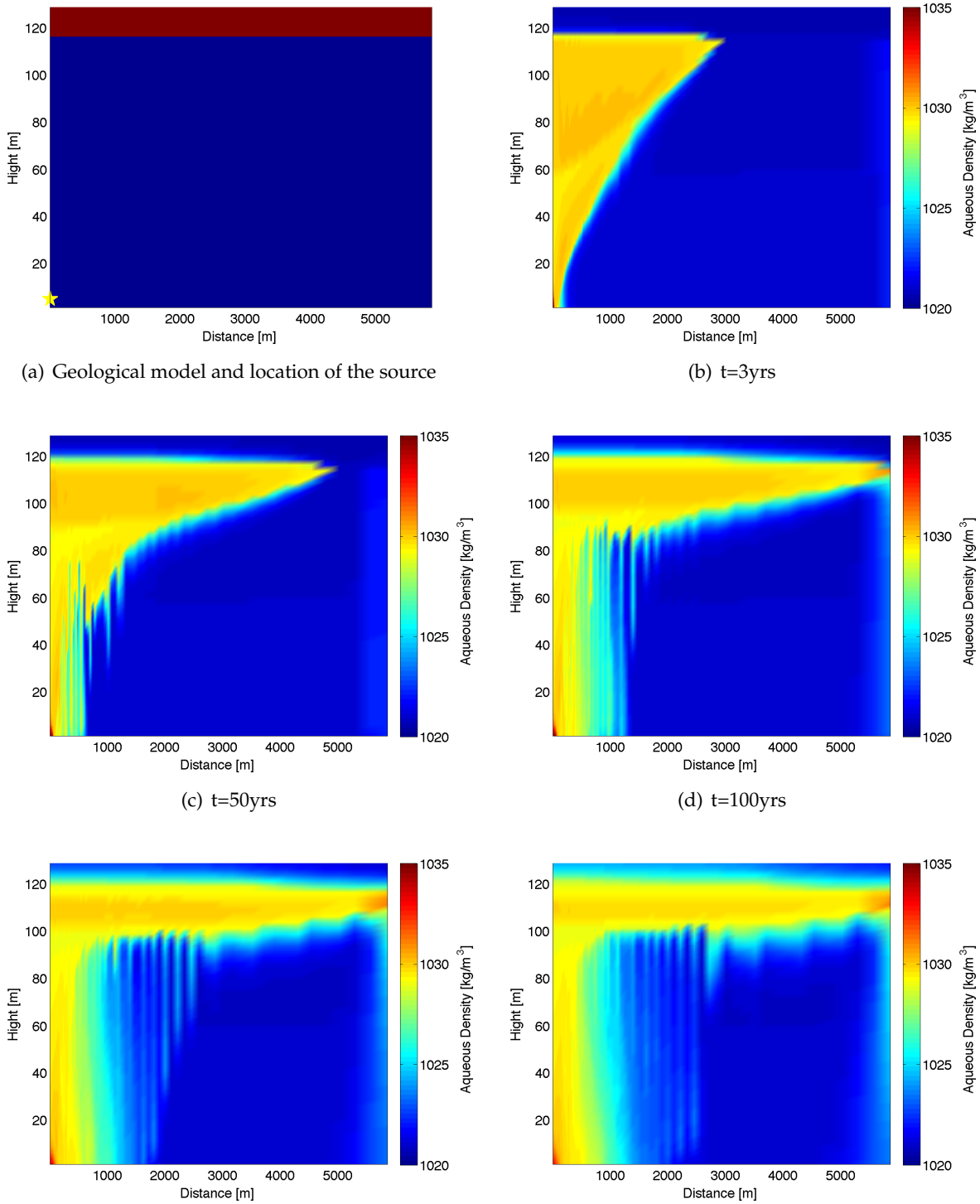

(a) Geological model and location of the source

(b) t=3yrs

(c) t=50yrs

(d) t=100yrs

(e) t=200yrs

(f) t=300yrs

Figure 2.18: (a) Geological model, red indicates the shaly seal and blue the sandstone aquifer. The yellow star indicates the location of the source. (b)-(f) Plots of the aqueous density at different timesteps. Note the formation of the viscous fingers.

2.4 Seismic modelling

2.4.1 Viscoelastic Equations

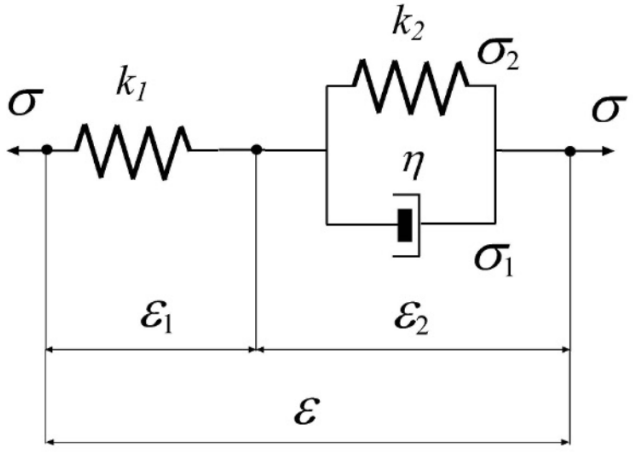

Figure 2.19: Mechanical model for a Zener material. (After Carcione (2015))

To compute the synthetic seismograms, we use a modelling code based on an isotropic and viscoelastic stress-strain relation (chapters 2 and 3 of Carcione (2015), the equations were first introduced in Carcione et al. (1988)). The term anelasticity indicates that once a material starts to vibrate, it will not continue indefinitely. Furthermore, the stress at a fixed point of the medium will depend on the strain at all previous times. We could say that the material has *memory*, which is stronger for recent times and fades away in the remote past. This is modelled by means of a relaxation tensorial function, the components of which decrease in time. It is common to represent anelasticity by means of a mechanical model having as basic elements mechanical, weightless springs and dashpots, which are loosely fitted pistons in fluid-filled cylinders. The mechanical model used in the code is the standard linear solid, or Zener model (Zener (1948)). A schematic representation of the system can be seen in Figure 2.19.
The relations between stress σ and strain ϵ for each of the elements are

$$\begin{aligned} \sigma &= k_1 \epsilon_1, \\ \sigma_1 &= \eta \partial_t \epsilon_2, \\ \sigma_2 &= k_2 \epsilon_2, \end{aligned} \tag{2.22}$$

where k_1 and k_2 are the elastic constants of the springs and η is the viscosity of the fluid in the dashpot. We assume $k_1, k_2, \eta \geq 0$. The total stress and strain of the system will be given by

$$\sigma = \sigma_1 + \sigma_2, \quad \epsilon = \epsilon_1 + \epsilon_2. \tag{2.23}$$

Based on this model, if we assign one relaxation mechanism for bulk (ν=1) and shear (ν=2) anelastic deformations, in the 2D (x,z,) plane we can write the complex Zener modulus as

$$M(\omega)^{(\nu)} = \frac{\tau_\sigma^{(\nu)}}{\tau_\epsilon^{(\nu)}} \left(\frac{1 + i\omega\tau_\epsilon^{(\nu)}}{1 + i\omega\tau_\sigma^{(\nu)}} \right), \quad \nu = 1, 2, \tag{2.24}$$

where ω is the angular frequency and $\tau_\epsilon^{(\nu)}$ and $\tau_\sigma^{(\nu)}$ are the relaxation times. The quality factor Q is given by

$$Q(\omega)^{(\nu)} = \frac{\mathrm{Re}(M)}{\mathrm{Im}(M)} = \frac{1 + \omega^2 \tau_\epsilon^{(\nu)} \tau_\sigma^{(\nu)}}{\omega \left(\tau_\epsilon^{(\nu)} - \tau_\sigma^{(\nu)} \right)}. \tag{2.25}$$

which reaches a minimum $Q_0^{(\nu)}$ at frequency $\omega_0 = 1/\tau 0$, where $\tau_0 = \sqrt{\tau_\epsilon \tau_\sigma}$. We take f_0=$1/\tau_0$ to be the central frequency of the source. From this minimum quality factor we can express relaxation times as

$$\tau_\epsilon^{(\nu)} = \frac{\tau_0}{Q_0^{(\nu)}} \left(\sqrt{2Q_0^{(\nu)} + 1} + 1 \right), \quad \tau_\sigma^{(\nu)} = \tau_\epsilon^{(\nu)} - \frac{2\tau_0}{Q_0^{(\nu)}} \tag{2.26}$$

The complex velocities will be given by

$$v_P = \sqrt{\frac{K + 4\boldsymbol{\mu}/3}{\rho}}, \quad v_S = \sqrt{\frac{\boldsymbol{\mu}}{\rho}} \tag{2.27}$$

$$K = kM^{(1)} \quad \boldsymbol{\mu} = \mu M^{(2)}, \tag{2.28}$$

The unrelaxed moduli k and μ can be obtained as follows: the phase P and S velocities are given by

$$c_p = \left[\mathrm{Re} \left(\frac{1}{v_p} \right) \right]^{-1} \quad c_s = \left[\mathrm{Re} \left(\frac{1}{v_s} \right) \right]^{-1}, \tag{2.29}$$

then, assuming $\mu_m = \rho c_S^2(f_0)$ (Carcione (2015))

$$\mu = \mu_m \left[\mathrm{Re} \sqrt{\frac{1}{M^{(2)}(f_0)}} \right]^2 \tag{2.30}$$

while k can be computed solving

$$\mathrm{Re} \sqrt{\frac{\rho}{kM^{(1)}(f_0) + 4\mu M^{(2)}(f_0)/3}} - \frac{1}{c_p(f_0)} = 0, \tag{2.31}$$

We can express the velocity-stress equations by means of Euler-Newton's equations:

$$\dot{v_x} = \frac{1}{\rho}\left(\sigma_{xx,x} + \sigma_{xz,z}\right) + f_{xx}, \tag{2.32}$$

$$\dot{v_z} = \frac{1}{\rho}\left(\sigma_{xz,x} + \sigma_{zz,z}\right) + f_z, \tag{2.33}$$

where v_x and v_z are particle velocities, σ_{xx}, σ_{zz} and σ_{xz} are components of the stress tensor and f_x and f_z are the body forces. The constitutive equations relating stress and velocity are

$$\dot{\sigma}_{xx} = k(v_{x,x} + v_{z,z} + e_1) + \mu(v_{z,z} - v_{z,z} + e_2) + f_{xx}, \tag{2.34}$$

$$\dot{\sigma}_{zz} = k(v_{x,x} + v_{z,z} + e_1) - \mu(v_{x,x} - v_{z,z} + e_2) + f_{zz}, \tag{2.35}$$

$$\dot{\sigma}_{xz} = \mu(v_{x,z} + v_{z,x} + e_3) + f_{x,z}, \tag{2.36}$$

where f_{ij} are components of the body forces and e_1,e_2 and e_3 are memory variables given by

$$\dot{e_1} = \left(\frac{1}{\tau_\epsilon^{(1)}} - \frac{1}{\tau_\sigma^{(1)}}\right)(v_{x,x} + v_{z,z}) - \frac{e_1}{\tau_\sigma^{((1))}}, \tag{2.37}$$

$$\dot{e_2} = \left(\frac{1}{\tau_\epsilon^{(2)}} - \frac{1}{\tau_\sigma^{(2)}}\right)(v_{x,x} - v_{z,z}) - \frac{e_2}{\tau_\sigma^{(2)}}, \tag{2.38}$$

$$\dot{e_3} = \left(\frac{1}{\tau_\epsilon^{(2)}} - \frac{1}{\tau_\sigma^{(2)}}\right)(v_{x,z} - v_{z,x}) - \frac{e_3}{\tau_\sigma^{(2)}}, \tag{2.39}$$

2.4.2 Algorithm description

Let v_2 be the particle velocity perpendicular to the plane of propagation. Then, we can formulate the propagation of waves in a two-dimensional medium with the following particle-velocity/stress formulation of the equation of motion:

$$\partial_t \bar{\mathbf{v}} = \mathbf{H} \cdot \bar{\mathbf{v}} + \bar{\mathbf{f}}, \tag{2.40}$$

where

$$\bar{\mathbf{v}} = (v_2, \sigma_{32}, \sigma_{12})^\top \quad \bar{\mathbf{f}} = (f, 0, 0)^\top, \tag{2.41}$$

The equation of motion is subject to the initial condition $\bar{\mathbf{v}} = \bar{\mathbf{v}}_0$ and its solution is formally given by

$$\bar{\mathbf{v}}(t) = \exp(t\mathbf{H}) \cdot \bar{\mathbf{v}}_0 + \int_0^t \exp(\tau \mathbf{h}) \cdot \bar{\mathbf{f}}(t-\tau)\mathrm{d}\tau, \tag{2.42}$$

where $\exp(t\mathbf{H})$ is called evolution operator, since its application to the initial state gives the solution at time t. $\mathbf{H}$ is called the propagation matrix, as it contains the material properties and spatial derivatives. Consider constant material properties and substitute in the equation of motion the plane-wave kernel $\exp(i\mathbf{k} \cdot \mathbf{x} - i\omega_c t)$, where $\mathbf{k}$ is the real wavenumber vector, $\mathbf{x}$ is the

position vector and ω_c is the complex frequency. At this point, we are left with an eigenvalue problem for the eigenvalues $\lambda = -i\omega_c$ (Jain et al. (1984)). For a viscolestic medium, some of these eigenvalues have a real negative part, indicating attenuation. Furthermore, solving the equation in the time domain, we find that there are eigenvalues which are approximately equal to minus the reciprocal of the relaxation time of each of the attenuation mechanisms (Carcione (2015)).

In the code, time integration is computed with a 4th-oder Runge-Kutta method, which approximates Equation 2.40 as

$$\bar{\mathbf{v}}^{n+1} = \bar{\mathbf{v}} + \frac{dt}{6}\left(\Delta_1 + 2\Delta_2 + 2\Delta_3 + \Delta 4\right), \tag{2.43}$$

where

$$\begin{aligned}
\Delta_1 &= \mathbf{H}\bar{\mathbf{v}}^n + \bar{\mathbf{f}}^n \\
\Delta_2 &= \mathbf{H}\left(\bar{\mathbf{v}}^n + \frac{dt}{2}\Delta_1\right) + \bar{\mathbf{f}}^{n+1/2} \\
\Delta_3 &= \mathbf{H}\left(\bar{\mathbf{v}}^n + \frac{dt}{2}\Delta_2\right) + \bar{\mathbf{f}}^{n+1/2} \\
\Delta_4 &= \mathbf{H}\left(\bar{\mathbf{v}}^n + dt\Delta_3\right) + \bar{\mathbf{f}}^{n+1}.
\end{aligned} \tag{2.44}$$

Spatial derivatives are computed with a Fourier pseudospectral method. Assuming that $v(x)$ is a continuos function, it can be approximated by the truncated series

$$v_N(x) = \sum_{r=0}^{N-1} \tilde{v}_r \psi_r(x), \tag{2.45}$$

where spectral functions ψ_r are

$$\psi_r(x) = \exp(ikx) \tag{2.46}$$

and the spectral coefficients $\tilde{v}_r$ are taken such that on a discrete, equidistant, set of gridpoints $x_1, x_2, \ldots, n_{N-1}$,

$$v_N(x_j) = v(x_j), \quad j = 0, 1, \ldots, N-1. \tag{2.47}$$

k_r is the discrete wavenumber

$$k_r = \frac{2\pi r}{Ndx}, \quad r = 0, 1, \ldots, N-1. \tag{2.48}$$

Therefore the spectral functions are

$$\psi_r(x_j) = \exp(2\pi irj/N). \tag{2.49}$$

The periodicity of the functions ψ_r implies that a wave exiting from one side will re-enter from

the other one. This phenomenon is called wraparound and it is the reason for which any grid will have to be extended with damping layers on all sides.
Given the condition 2.47, the set of equations

$$v(x_j) = \sum_{r=0}^{N-1} \tilde{v}_r \exp(2\pi i r j/N) \tag{2.50}$$

will be equivalent to

$$\tilde{v}_r = \frac{1}{N} \sum_{j=0}^{N-1} v(x_j \exp(2\pi i r j/N) \tag{2.51}$$

This method is convenient, since the computation of the derivatives reduces to a multiplication of the coefficients $\tilde{v}_r$ by factors ik_r. In fact

$$\partial_1 \psi_r(c) = ik_r \psi_r(x), \tag{2.52}$$

so that

$$\partial_1 v_N(x) = \sum_{r=0}^{N-1} ik_r \tilde{v}_r \psi_r(x). \tag{2.53}$$

The coefficients $\tilde{v}_r$ are computed with the fast Fourier transform.

Chapter 3

Active Cross-Hole Monitoring Experiment

In this chapter we present modelling of all steps of a cross-hole monitoring experiment. The aim is to monitor the propagation of the CO_2 plume, by detecting the seismic velocity anomalies due to the presence of the carbon dioxide. We consider a synthetic, yet realistic, 2D geological model consisting of a sandstone aquifer, with shaly sandstone intrusions. We model the injection of the carbon dioxide using STOMP software. From the output of this simulation, we compute seismic velocities and attenuation factors with a mesoscopic rock-physics theory. Using a viscoelastic code, we then compute synthetic cross-hole seismograms, of which we perform an inversion for direct waves.

3.1 Geological Setting

As in Carcione et al. (2012) we consider a sandstone aquifer, part of an anticlinal structure, with shaly intrusions, embedded on the top and bottom by very low permeability shales. The formation has its top at 700 m b.s.l, its bottom at 1500 m and extends for 800 m in the horizontal direction. Furthermore, it is very heterogenous and we assume that its grains are a mixture of quartz and clay, with clay contents ranging from 7% in the aquifer to 70% in the sealing shale, matching the values found at the Sleipner field (see section 2.3.1, Table 2.1). We consider two wells separated by 150 m, where sources and receivers are located. Maps of clay content, porosity, permeability and the position of the wells can be seen in Figure 3.1. As for the elastic properties of the medium, we consider a grain density of 2650 kg/m^3 for both grain types. Bulk and shear moduli of the clay grains are 25 Gpa and 20 Gpa respectively, while those for the sand grains are of 39 Gpa and 40 Gpa. The domain is divided in 315x315 square cells, with a spacing of 2.5 m in both horizontal (x) and vertical (z) direction.

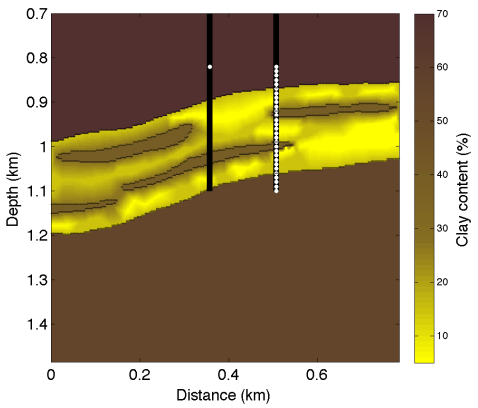

(a) Clay Content

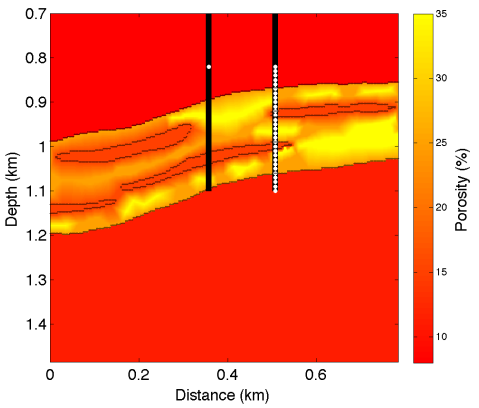

(b) Porosity

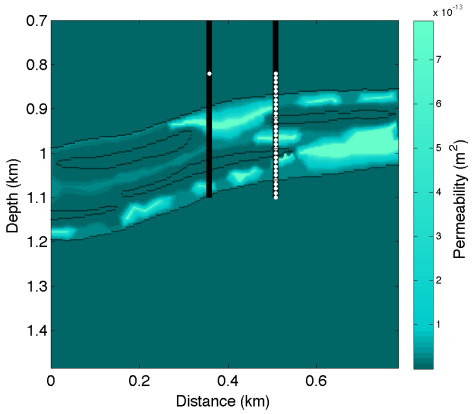

(c) Permeability

Figure 3.1: Maps of the properties of the synthetic anticline: (a) clay content, (b) porosity and (c) permeability and positions of the two wells.

Zone/Rock Type	ϕ	κ (m^2)	α (1/m)	m	S_{lr}
1/Shale	0.09	1e-12 m^2	0.16	1.667	0.2
2/Shaly Sandstone	0.12	1e-12 m^2	0.16	1.667	0.2
3/Sandstone	0.36	1e-17m^2	2.84	1.667	0.2

Table 3.1: Properties of the three rocktypes in the simplified aquifer.

3.2 Fluid Flow Simulation

We simulated the injection and propagation of the carbon dioxide using STOMP commercial software described in section 2.2. Due to the complexity of the medium and the fine grid required by the following steps of the project, parametrisation of the finite-difference solver was far from trivial. Therefore, as a first step, we considered a simplified domain, in which we identified three "zones", corresponding to three different types of rock: sand, shale and shaly sandstone. A map of this "zoned" aquifer can be seen in Figure 3.2 and the properties of each rocktype are summarised in Table 3.1

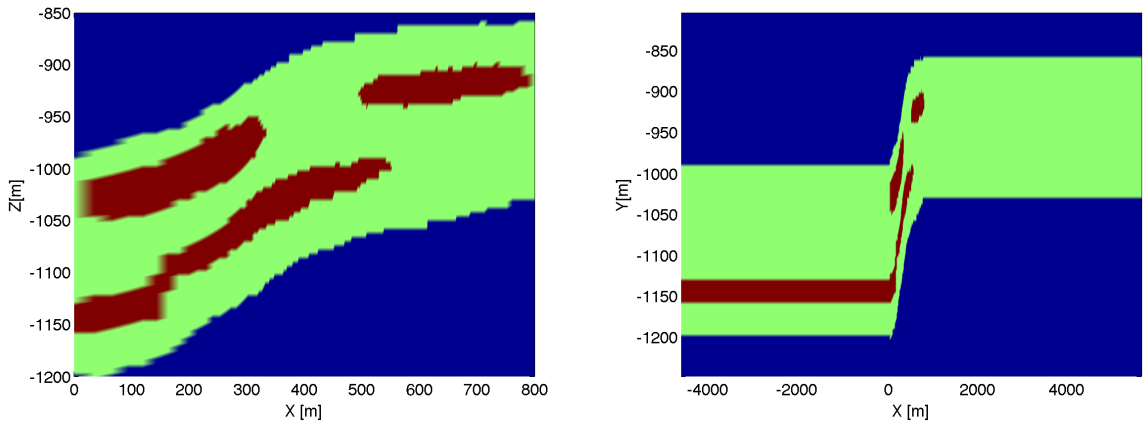

(a) Zoom of the simplified aquifer

(b) Entire domain

Figure 3.2: Map of the simplified, "zoned" aquifer (a) and of the full domain on which the fluid flow simulation is launched (b).

Using this simplified geology, we were able to setup the best grid, initial and boundary conditions as well as the capillary parameters of the rocks. As for the grid, we assume that the aquifer is infinitely extended in the horizontal direction. Practically, this means extending the domain in the x-direction enough (50 km) to minimise the effects of the boundary conditions. In order to reduce the number of grid points and therefore the computational needs, we applied a grid which is very refined, with a spacing of 2 m, in the area of interest between the two wells and then let the distance between nodes increase progressively. We assume that the extension consists of a sandstone layer, embedded in shale. One of the shaly intrusions is extended on the left-hand side all the way to the border of the domain. A picture of the simulation domain is shown in 3.2 (b).

The initial conditions are hydrostatic, with hydrostatic pressure P_h proportional to the density of the brine $\rho_b = 1040 kg/m^3$ and depth h. $P_h = \rho_b g h$. We assume that the medium is fully saturated with brine before injection. We inject pure CO_2 at the point (499, -1026) m for two years at a rate of 26.8 T/d, that is 9.8 MT/a. Since the rocktypes here considered are those at the Sleipner field, we use the capillary curves and their parametrisation used for the test described in section 2.3.1.. That is, we consider a Van Genuchten relation for both capillary pressure and relative permeability curves, with the Mualem approximation. We take the pore size distribution parameter m and the residual brine saturation to be the same on the entire domain; on the other hand, we consider two different values of capillary entry head α; a lower one for the shale and shaly sandstone and a higher one for the sandstone. A picture of the values of α can be seen in figure 3.3.

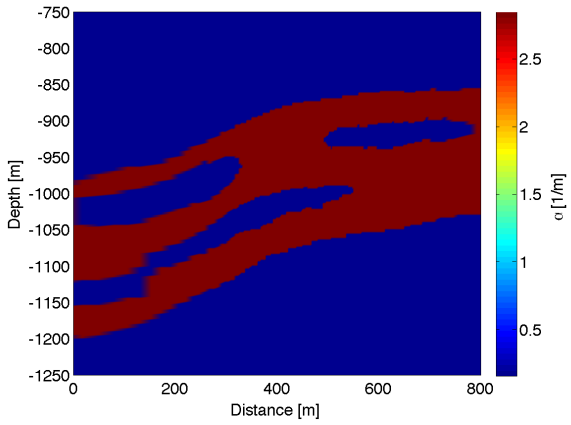

Figure 3.3: Map of the values of Alpha

The simulation ran smoothly and in figure 3.4 we can see the profiles for pressure and saturation after 1 (a) and 2 (b) years of injection. We can see how the CO_2 plume propagated easily in the permeable sandstone, while it hardly entered the silty mudstone intrusions, except close to the injection node.

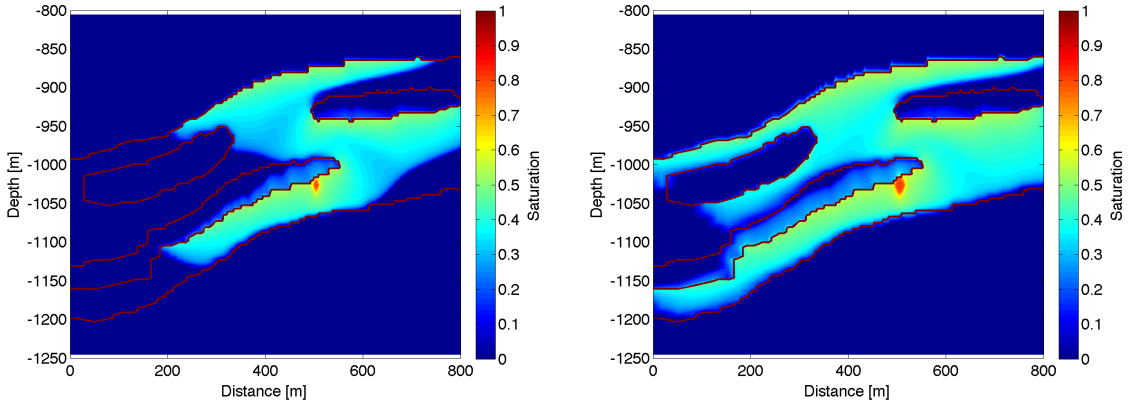

(a) Gas Saturation after 1 year

(b) Gas saturation after 2 years

Figure 3.4: Gas saturation in the simplified aquifer after 1 (a) and 2 (b) years of injection

We used the same grid, initial and boundary conditions and source parameters for the inhomogenous geological model. As for the capillary parameters, we "masked" the complex domain with the simplified one, using the same curves. The results of the simulation after 1 year of injection for gas saturation (a), pore pressure (b), gas density (c) and viscosity (d) are shown in Figure 3.5. The values of the density of the gas-phase confirm that the CO_2 is in supercritical state. Finally, we interpolated these results using a natural neighbour method, to match the regular 315 x 315 mesh used in all the following steps.

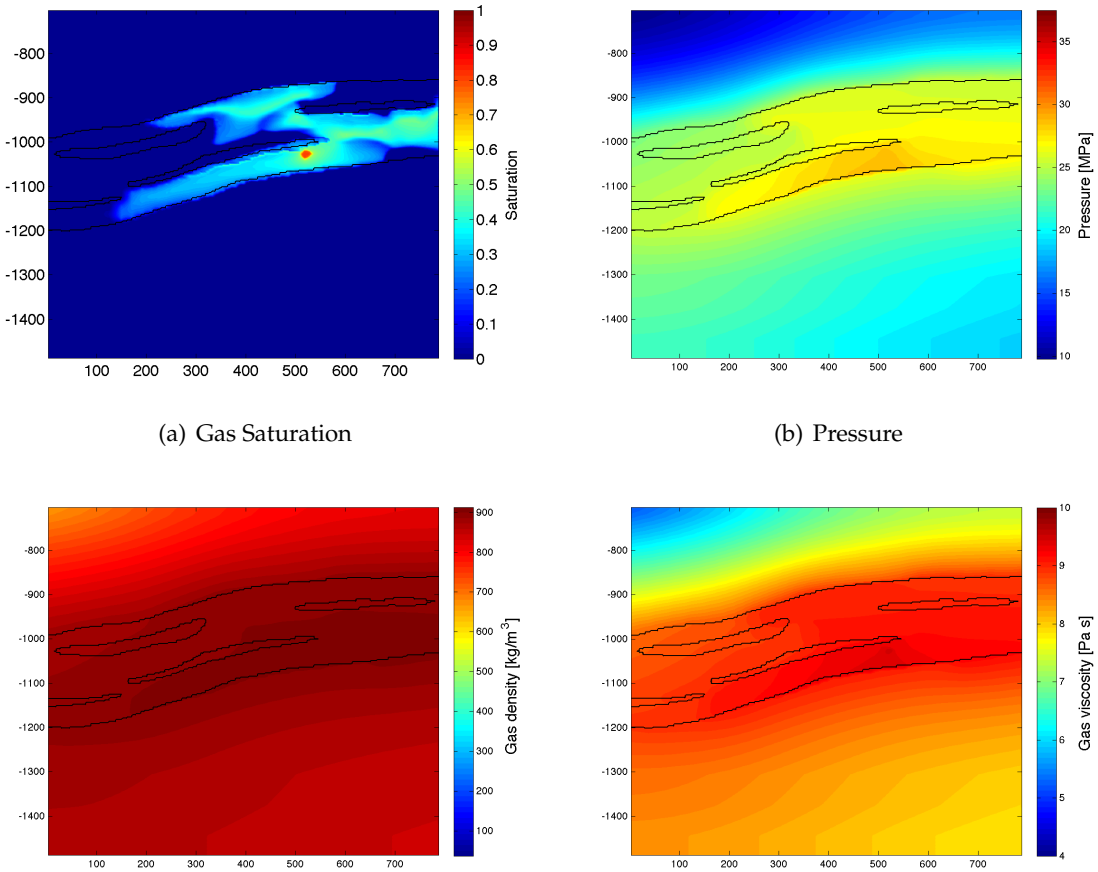

(a) Gas Saturation

(b) Pressure

(c) Gas density

(d) Gas viscosity

Figure 3.5: Results of the fluid.flow simulation after one year of injection. Maps of gas saturation (a), pore pressure (b) and gas density (c) are shown.

3.3 Seismic Velocities: White's Model

The presence of the CO_2 changes the elastic properties of the medium, affecting the propagation of both P- and S- waves. In fact, the presence of a second less dense and less stiff fluid in a medium is the main factor affecting the dispersion and attenuation of seismic waves (Picotti et al. (2010)). This is due to the the induced fluid-flow that can arise due to pore pressure gradients caused by high frequency waves propagating in the medium (Pride et al. (2004)), Picotti et al. (2010)). In fact, while at low frequencies relaxation lengths are large enough to consider the pore pressure almost constant (*relaxed regime*), at high frequencies, the relaxation length is short and differences in pore pressure can occur, leading to fluid flow (*unrelaxed regime*). Therefore, at low frequencies Gassman modulus can well describe the attenuation, while at higher frequencies it does not. This loss mechanism is particularly significant when one of the two fluids is very stiff and the other is very compliant, as in the case of water and carbon dioxide (Carcione et al. (2006)). White's theory (White (1975), Carcione et al. (2003b)) allows to compute seismic phase velocities and attenuation factors of a partially saturated medium as a function of

porosity, permeability, gas saturation, fluid viscosity and clay content. White considers water-filled cubes of porous medium of size l, with a gas-filled sphere of radius r_0. For simplicity of calculations, he then considers two concentrical spheres, the outer of which has the same volume of the cube. Therefore, the radius $r_1 > r_0$ of the outer sphere is $r_1 = l/(4\pi/3)^{1/3}$. Gas saturation can therefore be computed as $S_g = r_0^3/r_1^3$. We have to point out a weak point of the theory; in fact, when $r_0 \geq l$, corresponding to a gas saturation $S_g \geq \pi/6 = 0.52$ the gas pockets touch each other. Therefore, for gas saturations above 0.52 the theory is not strictly valid. The two main assumptions are that the radius r_1 is much larger than the radius of the grains and much smaller than the wavelength. Under these assumptions, the complex P- and S-wave velocities are:

$$v_P = \sqrt{\frac{K + 4\mu/3}{\rho}}, \quad v_S = \sqrt{\frac{\mu}{\rho}} \tag{3.1}$$

where K is the complex bulk modulus, μ is the complex shear modulus and ρ is the bulk density.

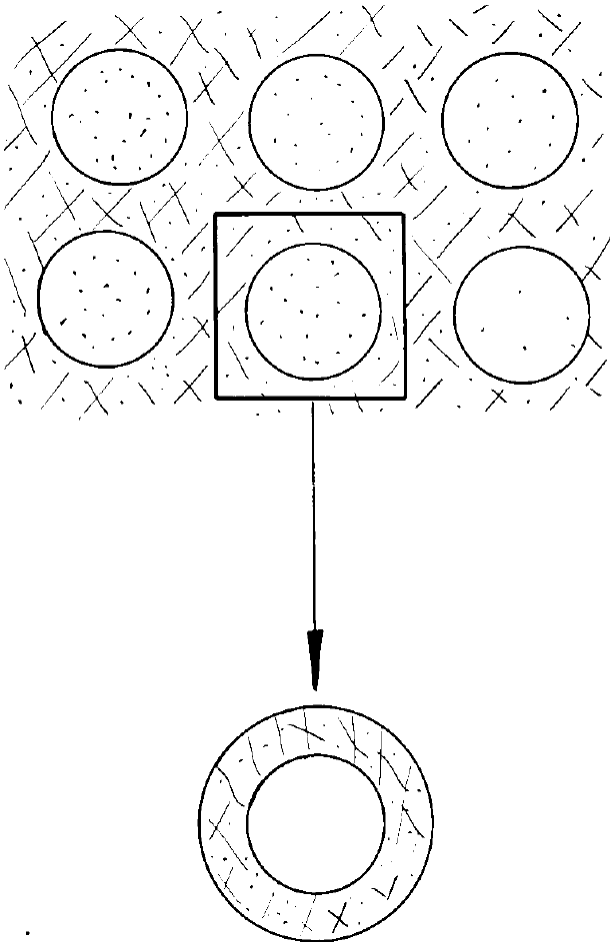

Figure 3.6: Representation of White's model. From White (1975)

The latter is the average of the solid grain ρ_s and fluid component ρ_f of the bulk:

$$\rho = (1-\phi)\,\rho_s + \phi\rho_f = (1-\phi)\left[(1-C)\,\rho_q + C\rho_c\right] + \phi\left[S_g\rho : g + \left(1-S_g\right)\rho_b\right], \tag{3.2}$$

where C is the clay content and S_g is the gas saturation.
We now derive expressions for the complex bulk and shear moduli. Since we consider the solid grains of the matrix to be a mixture of quartz and clay, this affects their bulk and shear moduli. We assume that these moduli are equal to the arithmetic average of the upper and lower Hashin-Strickman bounds (Hashin and Shtrikman (1963), Carcione et al. (2012)). The dry-rock bulk and shear moduli K_m and μ_m are obtained with a Krief model (Carcione (2015)):

$$K_m = K_s\,(1-\phi)^{\mathcal{A}(1-\phi)}, \quad \mu_m = \frac{\mu_s}{K_s}K_m, \tag{3.3}$$

where $\mathcal{A}$ is a dimensionless pore compliance parameter depending on the shape of the pores; for spherical pores it assumes a value of 2, with increasing values as the pores become more crack-like (David and Zimmerman (2011), Le Ravalec and Guéguen (1996)). If we assume that the dry-rock and grain moduli are the same in the region, as well as permeability, we can write the complex bulk modulus as

$$K = \frac{K_\infty}{1 - K_\infty W}, \tag{3.4}$$

where K_∞ is a -high frequency- bulk modulus when there is no fluid flow between the patches. W is the compliance:

$$W = \frac{3i\alpha\kappa\,(R_1 - R_2)}{b^3\omega\left(\eta_b Z_b - \eta_g Z_g\right)}\left(\frac{M_g}{K_{Gg}} - \frac{M_b}{K_{Gb}}\right), \tag{3.5}$$

where permeability κ is the average permeability of the shaly sandstone given, as a function of clay content by (Carcione et al. (2000))

$$\frac{1}{\kappa} = \frac{1-C}{\kappa_q} + \frac{C}{\kappa_c} = \frac{(\phi)^2}{\phi^3}\left[(1-C)^2 + C^2B^2\right], \tag{3.6}$$

where κ_q and κ_c are the partial permeabilities of quartz and clay respectively:

$$\kappa_q = \frac{r_q^2\phi^3}{45\,(\phi)^2\,(1-C)} \quad \text{and} \quad \kappa_c = \frac{r_c^2\phi^3}{45\,(1-\phi)^2\,C}. \tag{3.7}$$

As for the other quantities in equation 3.5

$$
\begin{aligned}
R_1 &= \frac{\left(K_{Gg} - K_m\right)\left(3K_{Gb} + 4\mu_m\right)}{K_{Gb}\left(3K_{Gg} + 4\mu_m\right) + 4\mu_m\left(K_{Gg} - K_2\right)S_g}, \\
R_2 &= \frac{\left(K_{Gb} - K_m\right)\left(3K_{Gg} + 4\mu_m\right)}{K_{Gb}\left(3K_{Gg} + 4\mu_m\right) + 4\mu_m\left(K_{Gg} - K_{Gb}\right)S_g}, \\
Z_1 &= \frac{1 - \exp\left(-2\gamma_1 a\right)}{\left(\gamma_1 a - 1\right) + \left(\gamma_1 a + 1\right)\exp\left(-2\gamma_1 a\right)}, \\
Z_2 &= \frac{\left(\gamma_2 b + 1\right) + \left(\gamma_2 b - 1\right)\exp\left[2\gamma_2\left(b - a\right)\right]}{\left(\gamma_2 b + 1\right)\left(\gamma_2 a - 1\right) - \left(\gamma_2 b - 1\right)\left(\gamma_2 a + 1\right)\exp\left[2\gamma_2\left(b - a\right)\right]}, \\
\gamma_j &= \sqrt{\frac{i\omega\eta_j}{\kappa K_{Aj}}} \\
K_{Aj} &= \frac{K_m}{K_{Gj}} M_j, \quad j = g, l,
\end{aligned}
$$

where ω is the angular frequency, η_j are the fluid viscosities with subscript j=g for gas and l for liquid, α is the Biot-Willis coefficient and M is a parameter:

$$
\alpha = 1 - \frac{K_m}{K_s}, \quad M_j(K_{fj}) = \left(\frac{\alpha - \phi}{K_s} + \frac{\phi}{K_f}\right)^{-1}, \tag{3.8}
$$

K_{Gg} and K_{Gb} are the Gassman (low-frequency) bulk moduli of the gas and brine saturated patches respectively.

$$
K_{Gj} = \frac{K_s - K_m + \phi K_m\left(K_s/K_{fj} - 1\right)}{\phi - K_m/K_s + \phi K_s/K_{fj}}, \quad j = g, l, \tag{3.9}
$$

where K_{fj} are the bulk moduli of the fluids. The high-frequency bulk modulus $K_\infty$when there is no fluid flow is then given by (Carcione et al. (2006))

$$
K_\infty = \frac{K_{Gb}\left(3K_{Gg} + 4\mu_m\right) + 4\mu_m\left(K_{Gg} - KGb\right)S_g}{\left(3K_{Gg} + 4\mu_m\right) - 3\left(K_{Gg} - K_{Gb}\right)S_g} \tag{3.10}
$$

In isotropic media, the phase velocity of homogenous waves and the corresponding quality factor are

$$
v_{phase} = \left[\mathrm{Re}\left(\frac{1}{v}\right)\right]^{-1}, \quad Q = \frac{\mathrm{Re}(v^2)}{Im(v^2)} \tag{3.11}
$$

where v is the complex velocity of the wave mode and ω is the angular frequancy ω=$2\pi f$. The quality factor associated with White's bulk modulus is

$$
Q = \frac{\mathrm{Re}(K)}{\mathrm{Im}(K)}, \tag{3.12}
$$

White's theory does not predict any shear dissipation. However, as proved by Picotti et al.

(2010), White's theory can be approximated, at least well enough to compute synthetic seismograms, with the standard linear solid, also called Zener model (Zener (1948)), which is described in section 2.4, equations 2.29 and 2.31., as it is used in the seismic modelling. In fact, both describe anelasticity in the frequency domain as a relaxation peak. We can therefore represent the complex shear modulus μ with a Zener element having a peak frequency f_0, which we take equal to the dominant frequency of the seismic source.

In Figure 3.7, we show bulk density, wave velocity and quality factors as a function of gas saturation for pure sandstone at a frequency of 80 Hz. The bulk density decreases as gas saturation increases, as expected. Furthermore, the bulk modulus decreases, causing a decrease in P-wave velocities. S- waves velocities are less affected by the presence of the gas. Finally, quality factors show a minimum at saturation 0.18. The fact that they remain constant after saturation 0.4 confirms that the model is not accurate at large saturations.

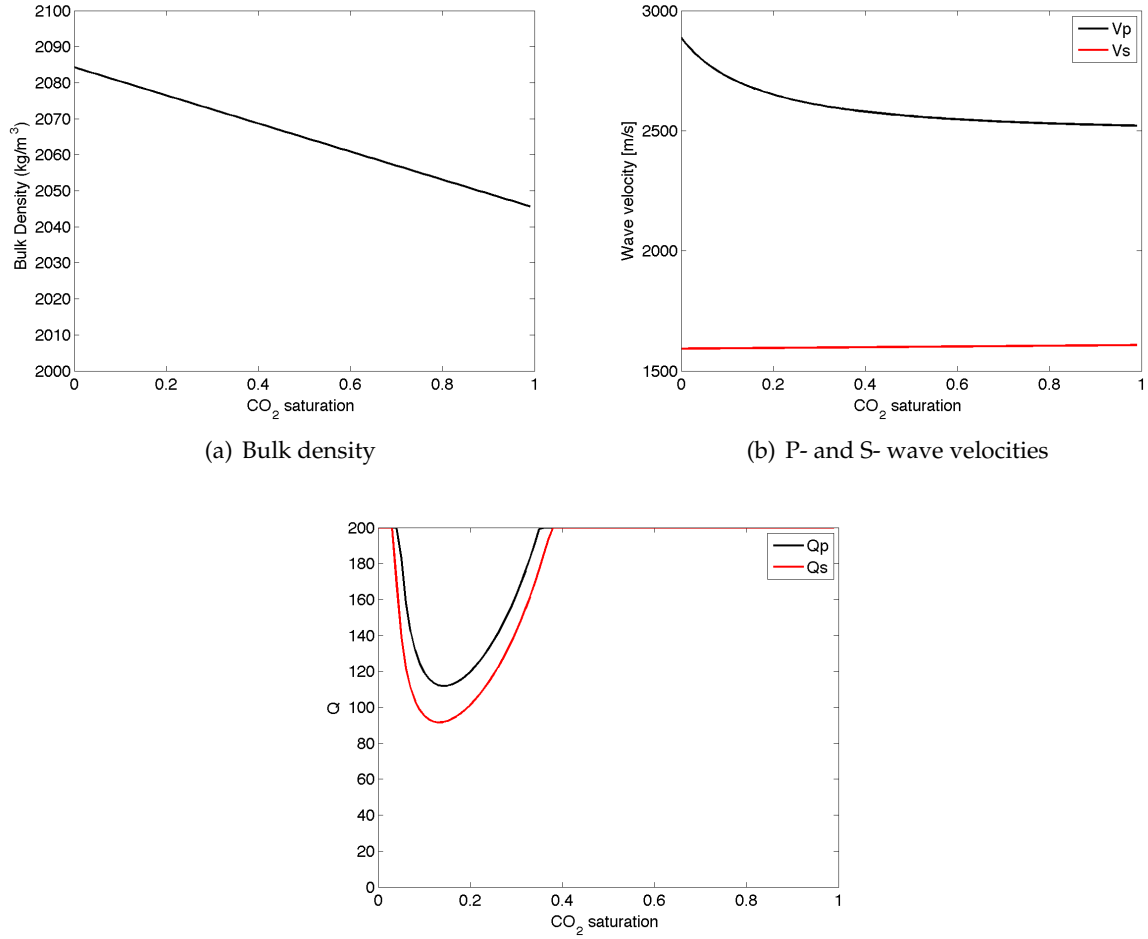

(a) Bulk density

(b) P- and S- wave velocities

(c) Quality factors

Figure 3.7: Graphs showing variations of the bulk density (a), P- and S- wave velocities (b) and quality factors (c) as a function of gas saturation.

Figure 3.8 shows plots of the wave velocities and bulk densities before and after one year of

injection. As expected, we notice that the difference in P-wave velocities is in the order of 200 m/s, which can be detected with a tomography on direct arrivals. In Figure 3.9 one can see the quality factors for P- and S-waves after one year injection.

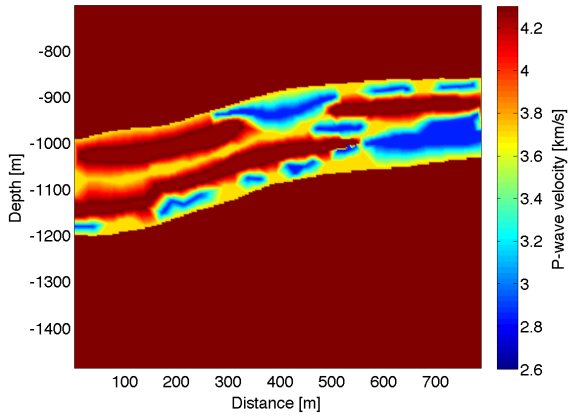

(a) P-wave velocity before injection

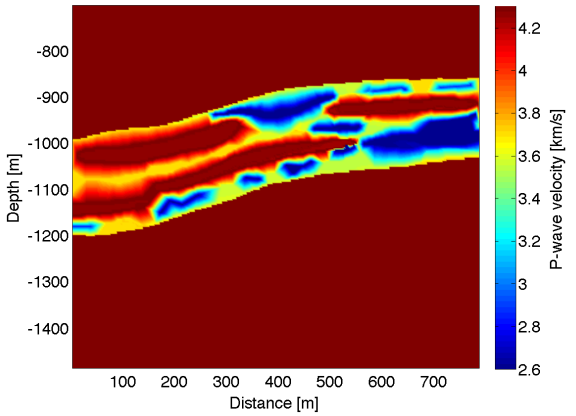

(b) P-wave velocity after injection

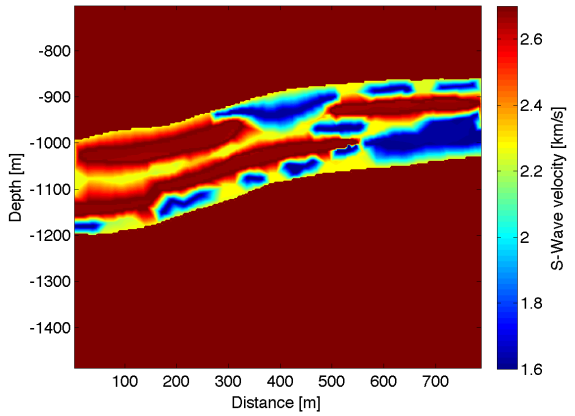

(c) S-wave velocity before injection

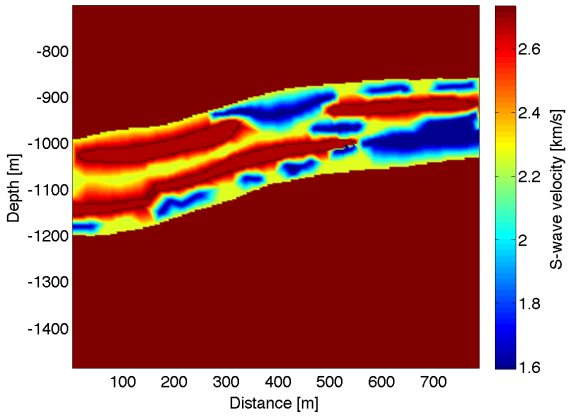

(d) S-wave velocity after injection

Figure 3.8: P- and S- wave velocities before (a) (c) and after (b) (d) injection.

3.4 Seismic Modelling

The synthetic seismograms are computed with the viscoelastic code described in section 2.4. We perform 90 shots in the left-hand side well, starting from a depth of 750 m with a spacing of 5 m. We consider explosive sources, with a dominant frequency of the Ricker wavelet set to 80 Hz. Figure 3.10 (a) shows the source wavelet. Since we need to pick the maximum amplitude to perform the tomography, we delay the onset of the recording until the maximum of the source wavelet is reached at 0.0179 s. We record for 0.3 s, with a sampling rate of 0.5 ms.
In order to avoid wraparound (see section 2.4.2, Equation 2.49), we extend the grid by 16 points and set these to be perfectly matched layers. The seismogram for shot n. 75, when the source is located at 1125 m depth, showing the significant velocity anomalies in the direct waves, can be

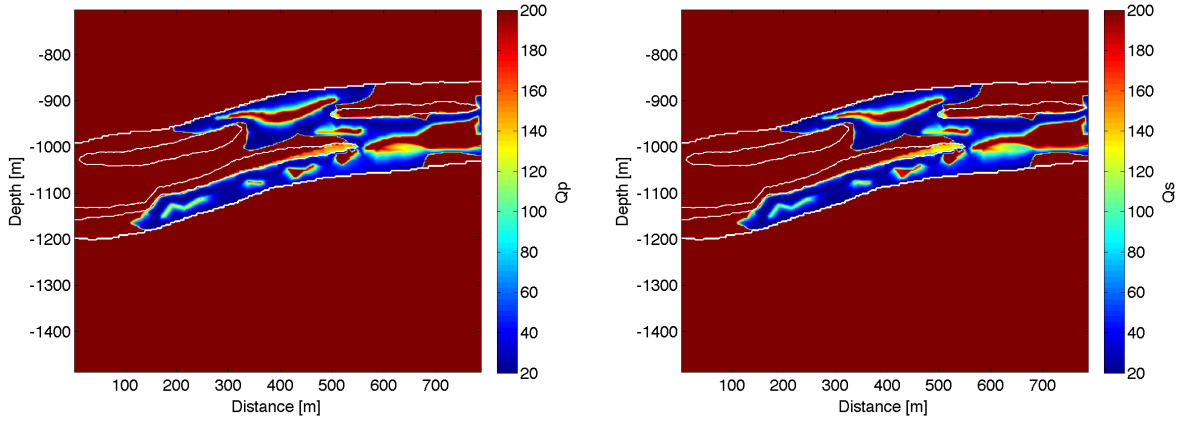

(a) Qp

(b) Qs

Figure 3.9: Quality factors after 1 year injection for P- (a) and S- (b) waves.

seen in Figure 3.10 (b). The velocity anomalies are even more visible in Figure 3.10 (c), which shows a snapshot of the vertical component of the wavefield at time t=100 ms for shot n. 25.

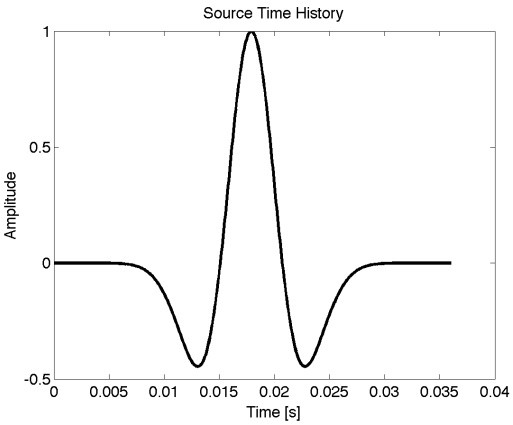

(a) Source time history

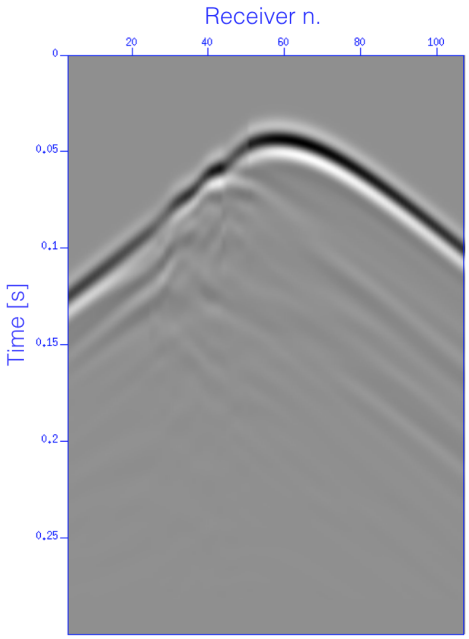

(b) Synthetic seismogram

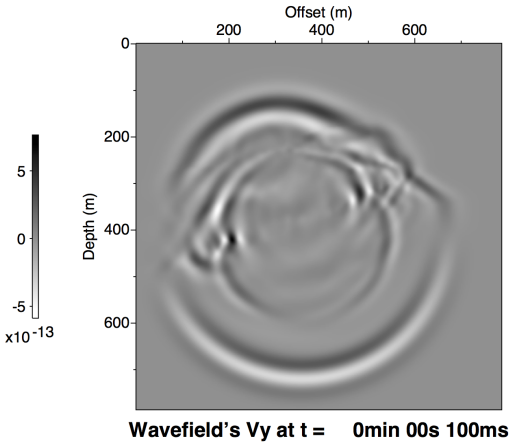

(c) Snapshot of the vertical component

Figure 3.10: (a) Source time history of the sources; dominant frequency is 80 Hz and the maximum amplitude is reached at 17.9 ms. (b) Seismogram for shot n. 75 and (c) Snapshot at t=100 ms. The source is located at a depth of 1125 m. There are visible anomalies in the velocities of the first arrivals.

3.5 Tomographic Inversion

We now invert the synthetic seismograms using CAT3D software, developed by G. Bohm et al. (a description of the software is given, for example, in Accaino et al. (2005) and Vesnaver et al. (1999)). Traveltime tomography is based on minimising the traveltime of a picked event in the seismogram. In our case, we invert the first arrivals, which in a cross-hole experiment are the direct waves. We therefore implemented an automatic picking algorithm of the maximum amplitude values of the first arrivals. The time at which these maximums occur are the input of the inversion algorithm. We invert for the area between the two wells (150 m apart), in the depth interval from 800 to 1300 m. We discretise the domain with a 10x34 regular grid, therefore each square has a size of 15 m. The grid is staggered twice in both directions by a third of a cell, i.e. 5 m. The staggered grid will therefore be of 30x102 cells, with each square cell having size of 5 m. As stated in Vesnaver and Böhm (2000) and Böhm and Vesnaver (1999), averaging the results of a low resolution grid, staggered once or more, allows to increase resolution and reduce ambiguity in the solution. In fact, a staggered grid combines the low number of parameters of a coarse grid and therefore its fast convergence and low ambiguity, with the resolution of a fine one. The initial model is set to be homogenous with a P-wave velocity of 3500 m/s. Since the velocity anomalies we want to detect are mainly horizontal, to avoid smearing effects, we consider only those rays which have an angle lower than 30° with respect to the horizontal. Ray coverage is sufficient, with 6058 rays, well distributed over the entire domain, as can be seen in Figure 3.12 (a), showing the ray density.

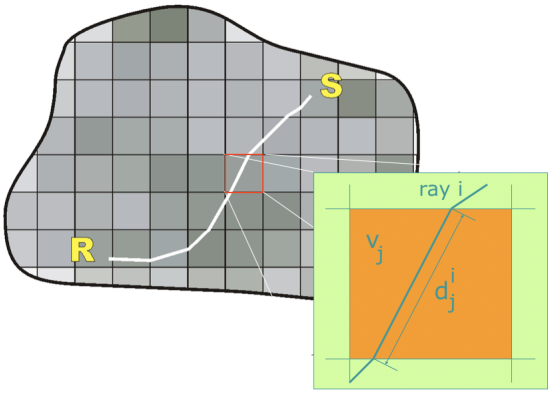

Figure 3.11: Schematic representation of the discretisation of the raypath for the tomography (after Bohm (2012))

The difference between computed and picked traveltimes is minimised with a Simulation Reconstruction Technique (SIRT, see Stewart (1991)) algorithm for 200 iterations, after which the RMS reaches an acceptable value (see Figure 3.12). Given that the traveltime from source S to receiver R (see Figure 3.11 is given by

$$t^i = \sum_{j=1}^{m} d_j^i s_j, \tag{3.13}$$

the SIRT algorithm updates the slowness s by Δs of the pixel j at each iteration i

$$\Delta s_j = \frac{1}{N} \sum_{i=1}^{N} \left(\frac{\Delta t^i d_j^i}{\sum_{j=1}^{M} \left(d_j^i \right)^2} \right), \tag{3.14}$$

where Δt^i is the residual in i-th ray, N is the total number of rays and M is number of pixels. This algorithm is not the fastest, but the averaging over all the rays allows to get smoother images.

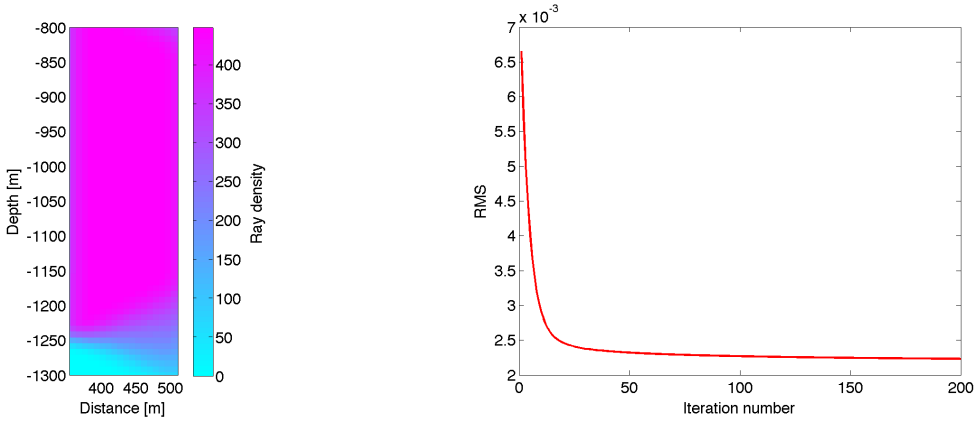

(a) Ray density

(b) RMS vs iteration number

Figure 3.12: (a) Paths of the straight rays across the two wells. (b) Curve of the values of the RMS versus the iteration number. The algorithm shows good convergence.

The results of the inversion, together with the map of P-wave velocity computed with White's model, can be seen in 3.13

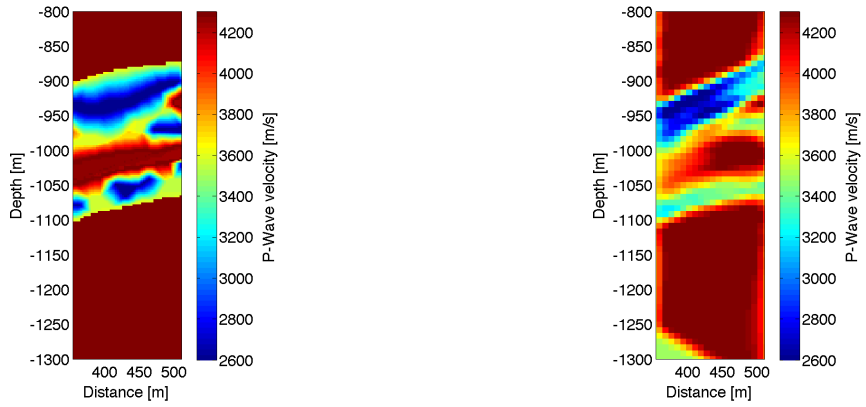

(a) P-wave velocity from White's model

(b) Results of the tomography

Figure 3.13: (a) P-wave velocities from White's model, in the domain to be inverted. (b) Reconstructed P-wave velocities. The two maps show good agreement, with the main anomalies well reconstructed.

We evaluate the reliability of the tomography by analysing its residuals. The mean RMS is

1.3 and the residuals look well distributed around zero in a gaussian-like trend, as shown in Figure 3.14(a). Figure 3.14(b) shows an example of fit of the computed versus picked traveltimes for shot number 55.

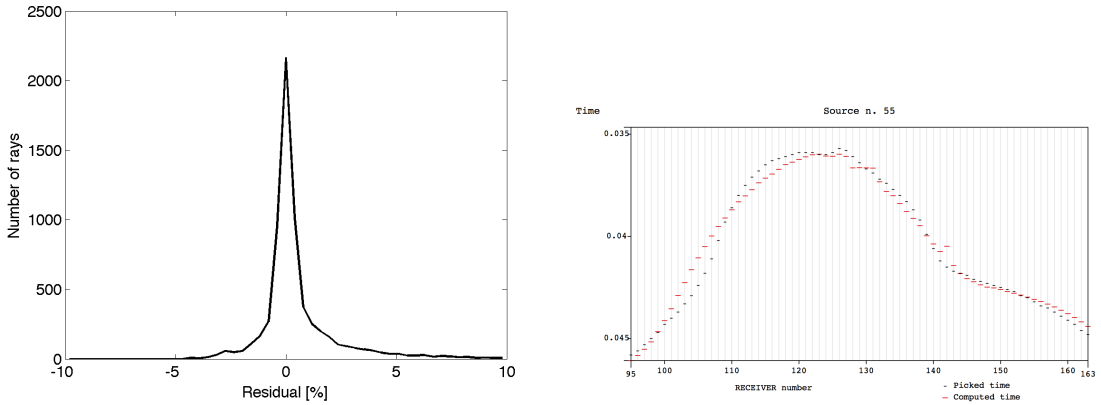

(a) Residual distributionl

(b) Picked and computed traveltimes

Figure 3.14: (a) Distribution of the residuals between picked and computed traveltimes. (b) Example of picked and computed traveltimes for shot n. 55.

Chapter 4

Passive Seismic Monitoring

NOTE: this chapter has been published as Carcione, J. M., Da Col, F., Currenti, G., Cantucci, B. (2015). Modeling techniques to study CO 2-injection induced micro-seismicity. International Journal of Greenhouse Gas Control, 42, 246-257.

In this chapter we present a modelling technique of a passive seismic monitoring experiment. In fact, passive seismic emissions caused by fluid injection can also be used to monitor the propagation of the CO_2 plume and eventual leakages, on the basis of the induced micro-cracks by the fluid front (e.g., Vesnaver et al. (2010); Oye et al. (2013)), since the fluid pressure may exceed the fracture pressure in many parts of the reservoir and emit P and S waves. In fact, induced seismic events of low magnitude are present during and after the injection (e.g., Urbancic et al. (2009); Oye et al. (2013)); Martínez-Garzón et al. (2013)). Moreover, micro-seismic data can be used to estimate the hydraulic diffusivity of the medium (Shapiro et al. (1997); Angus and Verdon (2013)). In this study, we first obtain the tensile and shear seismic sources generated by CO_2 injection in an infinite layer on the basis of an analytical solution of pressure diffusion obtained by Mathias et al. (2011)) and an emission criterion based on the stiffness properties of the medium. Fluid injection in a borehole causes an increase of the pore pressure in rocks, which implies a decrease of the effective stress, which, low enough, can trigger micro-earthquakes in zones of weakness. Tensile and shear failures occur as a consequence of the injection (Rutqvist et al. (2008); Stanchits et al. (2011)) and the common criterion to decide failure is based on a critical fluid pressure for fracturing that exceeds a given tectonic stress. Rutqvist et al. (2008) conclude that it is essential to have an accurate estimate of the in situ stress field to use this criterion. It is easier to establish the failure criterion on the basis of the strength of the rock, since this information (stiffness moduli) can be obtained from seismic data. The criterion we adopt here is the following. If the pore pressure exceeds the tensile and/or shear strength of the rock, defined by very small Young and shear moduli, there is emission whose strength is proportional to the excess pressure. These thresholds are assumed to vary on a fractal manner based on the von-Kármán correlation function (e.g. Carcione and Gei (2009)).

Langenbruch and Shapiro (2014) show that the elastic heterogeneity of rocks obtained from sonic and density logs along boreholes causes significant fluctuations of fracture reactivation and opening pressures. As a result fluctuations of principal stress magnitudes are of fractal nature. Correlation lengths of 1 m are assumed on the basis that the heterogeneities are smaller than the wavelength of a seismic signal. In the case of fine layering values from tens of cm to 1 m are realistic. The stiffness moduli can be obtained from seismic and sonic-log data or from ultrasonic experiments on cores. Other criteria exist to determine the emission, for instance, Rozhko (2010) uses the effective-stress law and the Coulomb yielding stress; the parameters are obtained from geo-mechanical triaxial laboratory measurements. Application of the injection technology near urban areas may involve seismic hazards (e.g., Sminchak et al. (2002)). Super-critical CO_2 is lighter than water and may cause pressure buildup leading to seismicity. The injection pressure at the well-head should not exceed a maximum which has to be calculated to assure that the pore pressure does not initiate new fractures or propagate existing fractures inducing micro-earthquakes of a given magnitude. The hydraulic diffusivity of the medium can be obtained from the envelope of events by representing the distance of the events to the injection point as a function of the emission times. The calculated diffusivity can then be used to estimate the formation permeability. Then, we simulate wave propagation of P and S waves, by using a forward modeling algorithm based on the pseudospectral method (Carcione et al. (2006); Carcione (2015)), to obtain microseismic data. Finally, we consider the location of the microseismic sources. A partial review of the method used so far to locate hypocenters of microseismic data can be found in Haldorsen et al. (2013). In particular they use a full-waveform migration algorithm and an imaging condition based on a semblance-weighted deconvolution between two or more reconstructed source signatures, requiring similarity and simultaneity of the reconstructed signatures. It is not clear if this method deals with asynchronous sources. Here, we outline an automatic technique to image asyn- chronous micro-earthquake sources, which should provide an image of the CO_2 cloud, by using reverse-time migration based on the Fourier pseudospectral method (e.g., Baysal et al. (1983)).

4.1 Fluid-flow modelling

To obtain the pore pressure around a well due to CO_2 injection in a brine saturated formation, we use the analytical solution (Sol. 1, immiscible fluids) derived by Mathias et al. (2009). In their work, they formulate the two-phase problem, as a function of time and radial (horizontal) distance in a formation of thickness H and radius R. We assume that (i) the pressure is constant along the vertical direction, (ii) capillary pressure are neglected, (iii) the CO_2 and brine phases are immiscible, (iv) relative permeability is linear with the saturation, (v) the properties are uniform, and (vi) the radial extent is much greater than the hole radius. Under these assumptions,

the problem is

$$\frac{\partial}{\partial t}\left[\phi\rho_g\left(H-h\right)\right]=-\frac{1}{r}\frac{\partial}{\partial r}\left[r\rho_g\left(H-h\right)q_g\right], \tag{4.1}$$

$$\frac{\partial}{\partial t}\left(\phi\rho_l h\right)=-\frac{1}{r}\frac{\partial}{\partial r}\left(r\rho_l h q_l\right), \tag{4.2}$$

with the flows q governed by Forchheimer's equation

$$\frac{\mu_\gamma}{\kappa_\gamma}q_\gamma+b\rho_\gamma q_\gamma|q_\gamma|=-\frac{\partial p}{\partial r},\quad ,\gamma=l,g, \tag{4.3}$$

where b is the Forchheimer parameter and p is the pressure.
This solution gives the pressure as a function of time and radial (horizontal) distance. On the basis of the list of symbols given here below, the solution is.

$$\hat{p}\left(\hat{t},\hat{r}\right)=\begin{array}{ll} E\left(2/\gamma\right)-\frac{1}{2}\ln\left(\frac{x}{2\gamma}\right)-1+\frac{1}{\gamma}+\frac{\beta}{\sqrt{xt}}, & \text{if } x\leq 2\gamma \\ E\left(2/\gamma\right)-\sqrt{\frac{x}{2\gamma}}+\frac{1}{\gamma}, & \text{if } 2\gamma<x\leq 2/\gamma \\ E\left(x\right), & \text{if } x>2/\gamma, \end{array} \tag{4.4}$$

where

$$E(x)=\begin{array}{ll} \frac{1}{2\gamma}E_1\left(\frac{\alpha x}{4\gamma}\right. & \left.\hat{t}\leq\hat{t_c}\right), \\ \frac{2\hat{t}}{\alpha\hat{R}^2}-\frac{1}{\gamma}\left[\frac{3}{4}-\frac{1}{2}\ln\left(\frac{\hat{R}^2}{x\hat{t}}\right)-\frac{(\gamma x-2)\hat{t}}{2\gamma\hat{R}^2}\right], & \hat{t}>\hat{t_c}, \end{array} \tag{4.5}$$

where $E_1(x)=-E_i(-x)$ is the exponential integral, which we recall

$$E_1\left(x\right)=\int_z^\infty\frac{e^{-t}}{t}dt \tag{4.6}$$

while the non-dimensional variables are

$$\hat{t}=\frac{m_0 t}{2\pi\left(1-S_{lr}\right)\phi H r_0^2\rho_g},\quad \gamma=\frac{\mu_g}{\kappa_g\mu_b},\quad \hat{R}=\frac{R}{r_0}, \tag{4.7}$$

$$\hat{p}=\frac{2\pi H\rho_g\kappa_r\kappa\left(p-p_i\right)}{m_0\eta_g},\quad \hat{r}=\frac{r}{r_0},\quad \hat{t}_c=\frac{\alpha\hat{R}^2}{2.246\gamma}, \tag{4.8}$$

$$\alpha=\frac{m_0\eta\left(C_r+C_l\right)}{2\pi\left(1-S_{lr}\right)H\rho_g\kappa_g\kappa},\quad \beta=\frac{m_0\kappa\kappa_g b b_r}{2\pi h r_0\mu_g},\quad x=\frac{\hat{r}}{\hat{t}}. \tag{4.9}$$

Eq. 4.4 assumes that the radial extent of the CO_2 plume is much smaller than R (closed formation). The whole solution corresponds to Eqs. 20 and 42 in Mathias et al. (2011). Mathias et al. (2009) provide a solution for the CO_2 brine interface elevation, which translated to saturation is

$$S_g=\begin{array}{ll} 1-S_{lr} & x\leq 2\gamma, \\ \frac{1-S_{lr}}{\gamma-1}\left(\gamma-\sqrt{\frac{2\gamma}{x}}\right), & 2\gamma<x<2/\gamma, \\ 0, & x\geq 2/\gamma, \end{array} \tag{4.10}$$

The symbols in equations 4.4 to 4.10 are listed here below.

b = Forchheimer parameter, m^{-1}

b_r = Relative Forchheimer parameter

C_r = Rock compressibility, Pa^{-1}

C_l = Brine compressibility, Pa^{-1}

η_g = CO_2 viscosity, Pa s

η_l = Brine viscosity, Pa s

κ_g = CO_2 relative permebility

κ = Permeability, m^2

m_0 = mass injection rate, kg s^{-1}

r_0 = Well radius, m

S_{lr} = residual aqueous saturation

Units are given in the SI system. A generalization should consider a non-linear pressure equation, since the permeability depends on the pressure field, meaning that the diffusivity varies with pressure. The reason is that cracks re-open when the pore pressure exceeds a given threshold. There are several permeability-pressure models ranging from exponential laws (e.g., Palmer et al. (1996)) to power laws (Gangi and Carlson (1996)). Shapiro and Dinske (2009) and Hummel and Shapiro (2012) use basically a model similar to that of Gangi and Carlson (1996).

We consider the Utsira Sand formation at the Sleipner field in the North Sea. At the injection site it has 280 m thickness (top at 820 m and bottom 1100 m b.s.l.). The sea bottom is located at nearly z_b = 100 m depth and the caprock is a sealing unit, a silty-mudstone layer approximately 200 m thick (Arts et al., 2008). We consider an injection point in the middle of the aquifer at z_0 = 960 m. The hydrostatic pressure is $p_H = \rho_b g z$, with ρ_b =1040 kg/m^3, the density of brine and g =9.81 m/s^2 , the gravity constant. We obtain 8.4 MPa, 9.8 MPa and 11.2 MPa at the top, z_0 and bottom, respectively. The confining pressure is $p_c = \bar{\rho} g z_b + g(z - z_b)$, where $\bar{\rho}$= 2100 kg/m^3 is the average sediment density (taken from well logs). We obtain 15.8 MPa, 18.8 MPa and 21.6 MPa at the top, z_0S and bottom, respectively. The medium and fluid properties to simulate the injection are given in Table 4.1. The permeability is an effective value because the formation contains low-permeability mudstone layers, (as in the example in section 2.3 and Arts et al. (2008)). The analytical solution (Mathias et al., 2011) is compared to numerical simulations using the TOUGH2 ECO2N commercial software (Pruess et al. (1999); Pruess (2011)). In fact, STOMP was not able to solve problems relative permeability is linear with saturation and therefore it was not able to reproduce the results of the semi-analytical solution. We consider van Genuchten curves for capillary pressure and relative permeability, with m=0.46, α=0.521 1/m. The linear

ϕ	0.36
κ	0.2 D
κ_{rg}	0.3
C_l	0.38 1/GPa
C_r=1/K_m	0.73 GPa
η_g	0.0847 x 10^{-3}Pa s
η_l	0.000963 Pa s
ρ_c	869 kg/m^3
S_{lr}	0.5
m_0	300 kg/s
p_i	9.8 MPa
r_0	0.2 m
H	280 m
R	20 km
b	0
b_2	0

Table 4.1: Material properties and dimensions.

relative permeability functions are

$$\kappa_{rl} = \kappa_{rl0}\left(\frac{1-S-S_{lr}}{1-S_{gc}-S_{lr}}\right), \quad \kappa_{rg} = \kappa_{rg0}\left(\frac{S-S_{gc}}{1-S_{gc}-S_{lr}}\right), \tag{4.11}$$

where S_{gc} is the critical gas saturation and κ_{rl0} and κ_{rg0} are endpoint relative permeabilities. In this simulation, S_{gc}=0, κ_{rl0}=1 and κ_{rg0}=0.3. TOUGH2 ECO2N also considers thermal effects by solving in addition the heat transport equation; the thermal conductivity of the medium is k_t = 2.5 W/m/°C and its specific heat capacity c_p=1000 J/kg/°C. The system is assumed to be initially free of CO_2 at a temperature of 40°C with an hydrostatic pressure uniformly distributed in the radial direction. The reservoir obeys at its sides to impermeable and adiabatic boundary conditions. The constant mass flux m_0 of pure supercritical CO_2 is injected at the well boundary. The radially symmetric computational domain is vertically divided in 14 equally spaced layers of 20 m thickness. In the radial direction, the domain is divided in 456 cells, whose spacing is finer (5 mm) near the well and coarser (1500 m) at the outermost boundary. The radial symmetry makes the problem basically two-dimensional. Figure 4.1 shows the pressure (a) and saturation (b) profiles for different injection times. Comparisons with these non-isothermal numerical results confirm that the analytical isothermal solution provides acceptable estimates of pressure buildup.

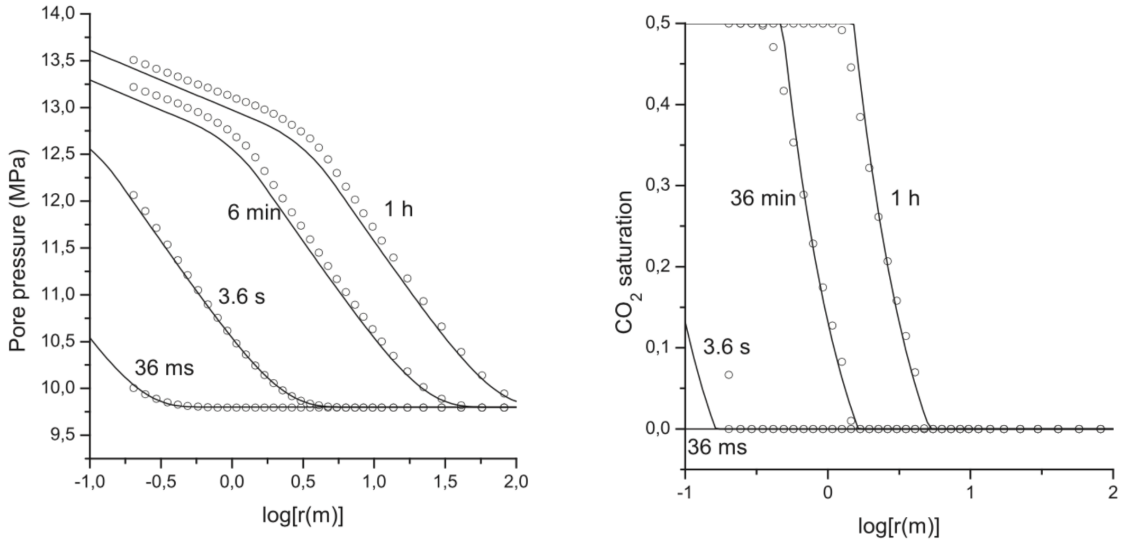

(a) Pressure

(b) Saturation

Figure 4.1: CO_2 injection in sand. Pressure (a) and saturation (b) profiles as a function of the radial distance from the well at different injection times, where the solid lines correspond to the analytical solution and the open circles refer to simulations obtained with the commercial software TOUGH2 ECO2N. The fluids are immiscible.

4.2 Emission Model

Induced seismicity by fluid injection in a porous rock depends on the properties of the medium, basically on the relation between the fluid pressure and the elastic properties of the skeleton. When the fluid pressure reaches the fracture pressure, the dry-rock stiffnesses decrease dramatically (e.g., Shapiro (2003); Carcione et al. (2006)). A realistic expression of the dry-rock Young and shear moduli, Y_m and μ, respectively, has the form

$$A = a - b \exp -p_e/p^*, p_e = p_c - np \tag{4.12}$$

(Shapiro (2003); Carcione (2015)), where p_c, p and p_e are the confining, pore and effective pressures, respectively, a, b and p^* are constants, and n is the effective stress coefficient. Constants a, b, p^* and n define the strength of the medium to an applied pore pressure and are found by fitting experimental data versus confining and pore pressures. The rock emits elastic energy at a given fracture pressure p, which we assume to occur at a small stiffness, i.e., if $A = \gamma a$, where $\gamma \ll 1$. Then,

$$P = \frac{1}{n}\left(p_c - p^* \ln \frac{b}{a\,(1-\gamma)}\right). \tag{4.13}$$

$Y_m = \mu = \gamma a$ imply tensile and shear sources, respectively, whose strength is proportional to the pressure difference $p - P_T$ (tensile) and $p - P_S$ (shear). There is tensile emission when $p > P_T$ and shear emission when $p > P_S$. The confining pressure is related to the vertical stress. It is implicitly assumed that there is a differential stress and/or anisotropy (vertical compaction)

to generate shear failure. Rutqvist et al. (2008) found that shear failure usually occurs at a lower injection pressure than tensile hydro-fracturing. We assume that $P_S < P_T$ and a fractal behaviour of these thresholds around an average value obtained from 4.13.

Let ΔP_m be the maximum deviation from the background value $P_0.p$ at R is first subjected to the variations $(\Delta P)^r$, such that

$$\Delta P_m \leq (\Delta P)^r \leq \Delta P_m \tag{4.14}$$

here (ΔP_m) is obtained from a random generator, and the superindex "r" denotes random. (Random numbers between 0 and 1 are generated and then scaled to the interval [-1, 1]ΔP_m.) The fractal variations can be described by the von Kármán auto-covariance function. The exponential function used by Rothert and Shapiro (2003) is a particular case of this function, which is widely used in seismic applications (e.g., Carcione et al. (2003a)). The corresponding wavenumber-domain spectrum of the von Kármán function is

$$S(k_1 k_2) = C(1 + k^2 l^2)^{-(\nu + d/2)}, \tag{4.15}$$

where $k = \sqrt{k_1^2 + k_2^2}$ is the wavenumber, l is the correlation length, ν (0<ν<1) is the self-similarity coefficient, C is a normalisationconstant, and D is the Euclidean dimension. The von Kármán correlation function describes self-affine, fractal processes of fractal dimension d + 1 - ν at scales smaller than l.

Correlation lengths can be determined from the power spectral density of physical rock properties determined from well-logging data, such as sonic logs (e.g., Holliger (1997)). The threshold P is then calculated as

$$P = P_0 \pm \Delta P(x, y), \tag{4.16}$$

where

$$\widetilde{\Delta P}^r(k_1, k_2) = \left(\widetilde{\Delta P}\right)^r (k_1, k_2) S(k_1, k_2). \tag{4.17}$$

with $(\widetilde{\Delta P})^r(k_1, k_2)$ being the Fourier transform of $(\Delta P)^r(x, y)$. The tilde denotes the space Fourier transform. The variation range ΔP around the mean value may determine the number of events. The larger this range the higher this number.

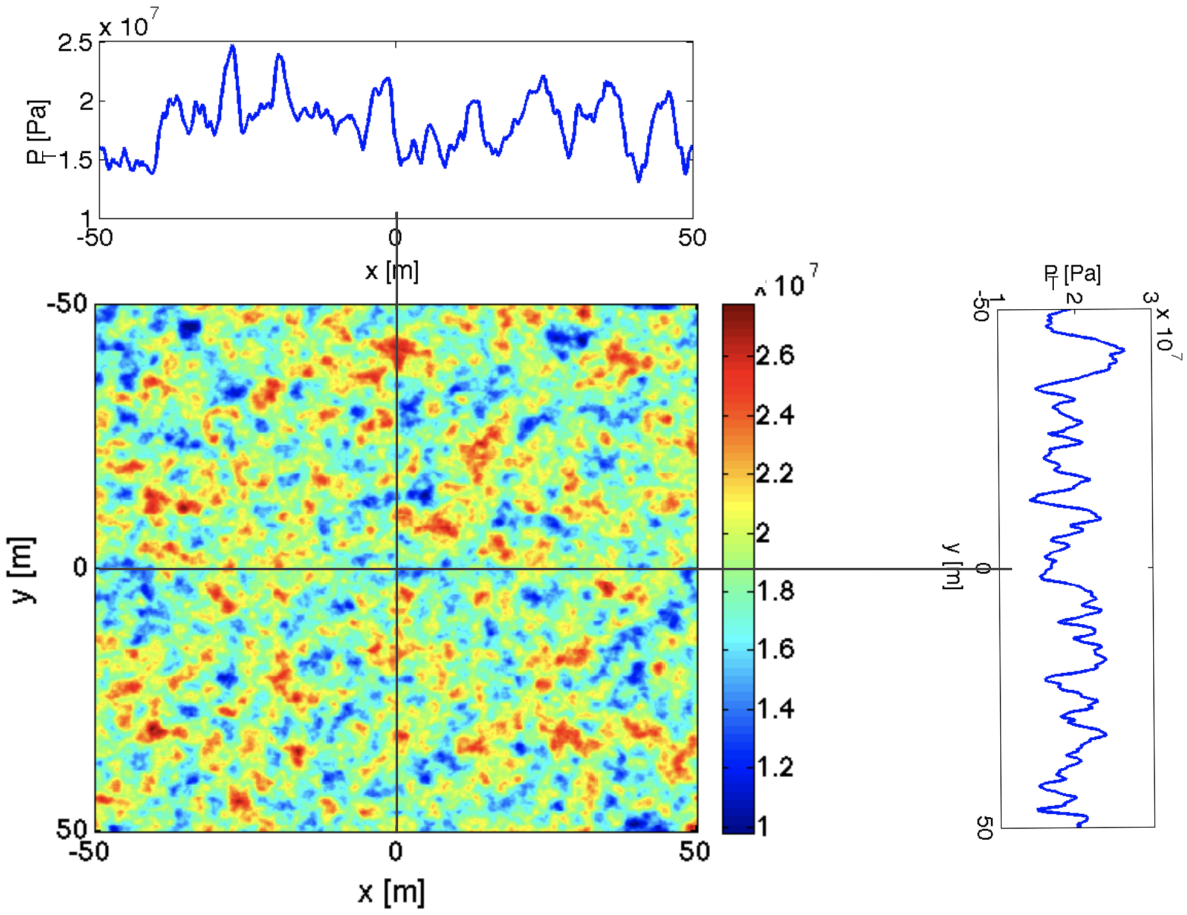

Figure 4.2: Random distribution of the failure criterion P_T (in MPa) based on the Young modulus. The medium is divided into 375 x 375 cells.

The approach is different from that of Rothert and Shapiro (2003), who consider only reactivation of pre-existing fractures and no tensile opening. These authors discretize the space and consider a single threshold. Here, each cell emits only one time; after the cell has emitted its stiffness is set to a very high value. Rocks are in a subcritical state of stress in some regions. Fracture occurs when the pore pressure is close but smaller than the confining pressure. At the fracture pressure the rock starts to break which means that the rock stiffness is approximately zero but not zero. Once the fracture pressure is determined, the threshold stiffness can be estimated from Equation 4.16. Most fracture models are based on equations of the form $P = \zeta(p_c - p) + p$ (Hubbert and Willis, 1957), where ζ is the effective stress ratio (also termed matrix stress coefficient) set to ζ=1/3 by Hubbert and Willis (1957) but allowed to vary with depth, in the range 0.3-1.0, by Pennebaker et al. (1968), from values of 0.3 for shallow layers to values near 1.0 at larger depths. Moreover, fracture pressures can vary randomly according to the rock stiffness locally. Here, we consider variations as in Rothert and Shapiro (2003).

We assume that at infinite effective pressure the dry-rock moduli are given by the upper limits

$$K_0 = K_s(1-\phi) \quad \text{and} \quad \mu_0 = \mu_s(1-\phi) \tag{4.18}$$

where K_s = 37 GPa and μ_s = 35 GPa are the grain bulk and shear moduli, (Carcione et al., 2006). Since the Young modulus is related to the bulk and shear moduli as $Y = 9K\mu/(3K+\mu)$, we obtain K_0 = 23.7 GPa, μ_0 =22.4 GPa and Y_0 = 51.1 GPa. The moduli 4.12,

$$Y_m = 51.1 - 50.6\exp(-p_e/0.35) \quad \text{and} \quad \mu_m = 22.4 - 22.37exp(-p_e/0.30), \tag{4.19}$$

with n=0.8 yields K_m =1.37 GPa and m =0.82 GPa at z=z_0, are in agreement with the experimental values (Carcione et al. (2006)), where a and b are given in GPa and p^* is given in MPa in Equation 4.19. Assuming γ= 0.03, the mean values 4.13 are

$$P_T = 14.4\text{MPa} \quad \text{and} \quad P_s = 12.4\text{MPa}. \tag{4.20}$$

Figure 4.2 shows a vertical section of the fractal distribution of P_T, where the medium has 375 x 375 cells with a grid spacing of 100m/375=0.26m along the horizontal and vertical directions. The fractal parameters are $P_0 = P_T$ ($P_0 = P_S$ in the shear case), with P_m =60 % P_0 = 0.18, l=1 m and d=2. If P_T or P_S are smaller or equal than 9.94 MPa (slightly above p_i), we set their value to 9.94 MPa, since at hydrostatic values of the pore pressure we assume no emission. Figure 4.3 shows the tensile (a) and shear (a) emission sources after one hour of injection, where the events are 4006 and 22,009, respectively. The location of the events as a function of the emission time is represented in Figure 4.4, where the solid line corresponds to

$$r = \sqrt{4\pi Dt} \tag{4.21}$$

(Shapiro et al. (1997)), with D = 0.137 m^2/s, where D is the hydraulic diffusivity. It can be seen that from a distance of 50 m the density of events is strongly decreasing. This signature occurs due to the small spatial extent of the model. Moreover, there are many events at the distance of the triggering front. These events correspond to cells where the initially selected critical pressure is below the value of 9.94 MPa. The triggering front corresponds to this isobar in both the shear and the tensile events. This is why the triggering front in both cases is identical. Thus, the difference of critical pressure magnitudes for tensile and shear events have only an effect on the density of the events. We use an equation based on poroelasticity to estimate the value of D. According to Biot theory, an approximation for a single fluid is

$$D = \frac{ME_m\kappa}{E_g\eta_g} \tag{4.22}$$

(Shapiro et al. (1997),Carcione (2015)) where

$$
\begin{aligned}
M &= \frac{K_s}{1-\phi-K_mK_s+\phi K_s/K_f}, \\
E_m &= K_m + \frac{4}{3}\mu_m, \\
E_G &= E_m + \bar{\alpha}^2 M, \\
\bar{\alpha} &= 1 - \frac{K_m}{K_s},
\end{aligned}
\tag{4.23}
$$

where K_f is an effective fluid bulk modulus Assuming ϕ=0.36, K_m =1.37 GPa, μ_m=0.82 GPa, K_s= 37 GPa, K_f=0.3 GPa and η= 0.000963 Pa s, we obtain D = 0.13 m^2/s, since the presence of CO_2 implies a lower value of K_f. Conversely, Equation 4.22 can be used to estimate the permeability if the poroelastic properties and effective fluid modulus are known.

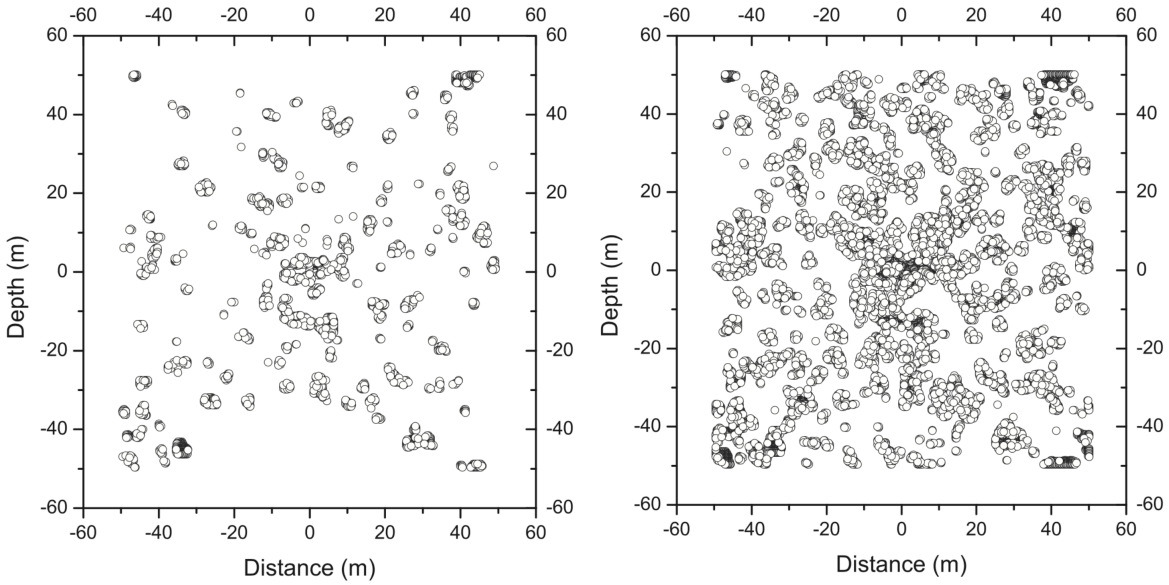

(a) Tensile sources (b) Shear sources

Figure 4.3: Cloud of tensile (a) and shear (b) events.

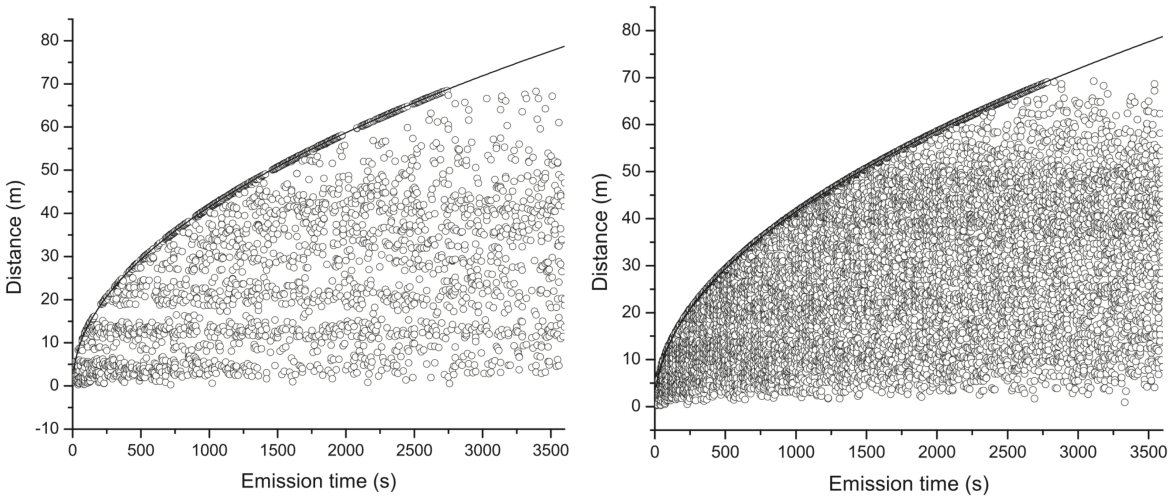

(a) Tensile sources (b) Shear sources

Figure 4.4: Location of the tensile (a) and shear (b) events as a function of the emission time, where the solid lines corresponds to Equation 4.22 with D = 0.137 m2 /s..

4.3 Seismic Modeling

The numerical modeling theory and code used to compute passive micro-seismograms is illustrated in Section 2.4.

As for the source implementation, the moment-tensor components in 3D space are

$$M_{ij} = M_0 m_{ij} \delta x \delta y \delta z g(t), \tag{4.24}$$

where m_0 is the moment tensor, δ is Dirac delta and $g(t)$ is the source time history, which satisfies

$$\int_0^{+\infty} |\dot{g}| dt = 1, \tag{4.25}$$

(Carcione et al., 2014a,b). The discrete version of the moment- tensor components are

$$M_{ij} = \frac{M_0}{dxdydz} m_{ij} g(t), \tag{4.26}$$

where dx,dy,dz are the grid spacings (dy =1 in our 2D case).

The moment-tensor theory describing tensile and shear sources is given, for instance, in Vavryčuk (2011). We have

$$\sqrt{2}\mathbf{m} = \begin{pmatrix} 2n_1\nu_1 & n_1\nu_2 + n_2\nu_1 & n_1\nu_3 + n_3\nu_1 \\ n_1\nu_2 + n_2\nu_1 & 2n_2\nu_2 & n_2\nu_3 + n_3\nu_2 \\ n_1\nu_3 + n_3\nu_1 & n_2\nu_3 + n_3\nu_2 & \nu_3\nu_3 \end{pmatrix} \tag{4.27}$$

where

$$
\begin{aligned}
n_1 &= -\sin(\delta)\sin(\phi), \\
n_2 &= \sin(\delta)\cos(\phi), \\
n_3 &= -\cos(\delta),
\end{aligned}
\tag{4.28}
$$

$$
\begin{aligned}
\nu_1 &= (\cos\lambda\cos\phi + \cos\delta\sin\lambda\sin\phi)\cos\varphi - \sin\delta\sin\phi\sin\varphi, \\
\nu_2 &= (\cos\lambda\sin\phi + \cos\delta\sin\lambda\cos\phi)\cos\varphi - \sin\delta\cos\phi\sin\varphi, \\
\nu_3 &= -\sin\lambda\sin\delta\cos\varphi - \cos\delta\sin\varphi
\end{aligned}
\tag{4.29}
$$

where here δ, λ and ϕ are the dip, rake and strike angles, respectively, and φ is the slope angle describing the tensility of the source, such that φ = 90° for pure extensive sources, φ = 0° for shear sources and φ = -90° for pure compressive sources. The components satisfy $m_{ij}m_{ij}$ = 1, where implicit summation is assumed. This implies $\sqrt{2}$ normalization in Equation 4.27. Equations 2.34 become then

$$
\begin{aligned}
\dot{\sigma}_{xx} &= k(v_{x,x} + v_{z,z} + e_1) + \mu(v_{z,z} - v_{z,z} + e_2) + M_{xx}, \\
\dot{\sigma}_{zz} &= k(V - x, x + v_{z,z} + e_1) - \mu(V - x, x - v_{z,z} + e_2) + M_{zz}, \\
\dot{\sigma}_{xz} &= \mu(v_{x,z} + v_{z,x} + e_3) + M_{x,z}.
\end{aligned}
\tag{4.30}
$$

For φ=0, we recover the usual moment-tensor components describing shear faulting:

$$
\begin{aligned}
\sqrt{2}m_{11} &= -\left(\sin\delta\cos\lambda\sin 2\phi + \sin 2\delta\sin\lambda\sin^2\phi\right), \\
\sqrt{2}m_{12} &= \left(\sin\delta\cos\lambda\cos 2\phi + \frac{1}{2}\sin 2\delta\sin\lambda\sin 2\phi\right), \\
\sqrt{2}m_{13} &= -\left(\cos\delta\cos\lambda\cos\phi + \cos 2\delta\sin\lambda\sin\phi\right), \\
\sqrt{2}m_{22} &= \left(\sin\delta\cos\lambda\sin 2\phi - \sin 2\delta\sin\lambda\cos^2\phi\right), \\
\sqrt{2}m_{23} &= -\left(\cos\delta\cos\lambda\sin\phi - \sin 2\delta\sin\lambda\cos\phi\right),
\end{aligned}
\tag{4.31}
$$

$$
\sqrt{2}m_{33} = \sin 2\delta\sin\lambda. \tag{4.32}
$$

Here we consider the 2D case and pure tensile and shear sources In the first case, we assume φ=λ=ϕ=90°, giving

$$
\sqrt{2}m_{xx} = 2\sin^2\delta, \quad \sqrt{2}m_{zz} = 2cos^2\delta, \quad \sqrt{2}m_{xz} = \sin 2\delta, \tag{4.33}
$$

while shear sources are described by φ=0 and λ=ϕ=90° giving

$$
\sqrt{2}m_{xx} = -\sin 2\delta, \quad \sqrt{2}m_{zz} = \sin 2\delta, \quad \sqrt{2}m_{xz} = -\cos 2\delta. \tag{4.34}
$$

We compute the unrelaxed moduli k and μ for partial saturation, we consider Gassmann

equations by which

$$k = K_m + \bar{\alpha}^2 M, \tag{4.35}$$

where $K_m = C_s$, and $\bar{\alpha}$ and m are given in Equation 4.23 (e.g., Carcione, 2015). The effective fluid bulk modulus is given by Wood equation,

$$K_f = \left(\frac{S_g}{K_g} + \frac{1 - S_g}{K_l} \right)^{-1}, \tag{4.36}$$

where K_g and K_l=1/C_l are the bulk moduli of CO_2 and brine, respectively.
On the other had, the density is

$$\rho = (1 - \phi)\, \rho_s + \phi \left[S_g \rho_g + \left(S_g \right) \rho_l \right]. \tag{4.37}$$

where ρ_s, ρ_g and ρ_l are the solid, CO_2 and brine densities, respectively.
Then, the P- and S- wave velocities are given by Equation 3.1, but here K and μ are real valued as this model,unlike White's, does not account for attenuation. We consider a numerical mesh with n_x =n_z = 231 gridpoints and a grid spacing dx = dz =5 m. The medium is homogeneous with the properties v_P = 1170 m/s, v_S = 650 m/s and ρ = 2017 kg/m^3 (from Equation 4.37), matching those of the Utsira formation (Carcione et al., 2006). The source time history is

$$g(t) = \left(u - \frac{1}{2} \right) e^{-u}, \quad u = \left[\frac{\pi \left(t - t_s \right)}{T} \right]^2, \tag{4.38}$$

where T is the period of the wave and we take t_s = 1.4 T. The peak frequency is f_p = 1/T = 25 Hz. The time step of the Runge-Kutta algorithm is 1 ms. Tensile sources are described by Equation 4.33 with δ= 0 and shear sources are described by Equation 4.34 with δ=$\pi/2$. Daugherty and Urbancic (2009) report magnitudes M_w from -2.3 to 0 for events caused by CO_2 injection. Moment magnitude is related to the seismic moment m_0 as m_0 = $10^{1.5\, M_w + 9}$ for m_0 expressed in J (Joule). We consider events with M_w = -1, i.e., m_0 = $10^{7.5}$ J, although different magnitudes can be modelled as well. Then, the non-zero components are M_{zz} = 1.8 MJ (tensile source) and M_{xz} = 0.9 MJ (shear source). Figure 4.5 shows a snapshot where the radiation pattern and relative amplitudes of the two types of sources can be observed. Theoretical expressions and representations of the radiation patterns are given in Vavryčuk (2011).

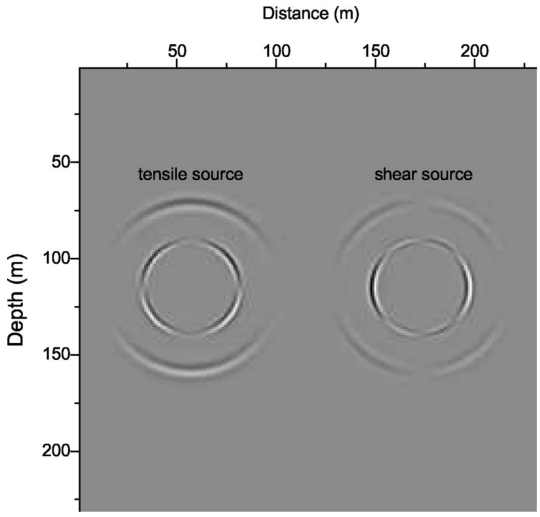

Figure 4.5: Snapshot of the vertical component of the particle velocity at 0.4 s, showing the radiation patterns of the tensile and shear sources. The maximum value is 8.4 mm/s.

To illustrate a simulation, we consider the interval 3000-3020 s, with 52 shear sources and 6 tensile sources. Figure 4.6 shows the model and a snapshot at 3000.5 s corresponding to the first three shear sources and a tensile source, all synchronous with onset times of 3000.056 s. The time parameter of the relaxation mechanisms is $\tau_0 = 1/(2\ \pi\ 25\ \text{Hz})$. In this simulation, absorbing strips are active to damp the wave fields reaching the sides, top and bottom of the mesh to avoid wraparound (50 nodes at the sides and 40 nodes in the vertical direction). For simplicity, we assume a formation with average dry-rock properties given by Equations 4.35 and 4.36, with the properties reported above and K_c = 25 MPa (Carcione et al., 2006), K_w = 2.63 GPa, ρ_s = 2650 kg/m^3 , ρ_g = 869 kg/m^2 and ρ_l = 1040 kg/m^3 . Figure 4.7 shows the P- and S-wave velocities and bulk density as a function of the radial distance, based on the saturation shown in Figure 4.1. It is worth to note the remarkable change in the velocity of the compressional wave due to the replacement of water near the well by CO_2 with a very low bulk modulus. However, at 3000 s the CO_2 is practically confined around a few meters from the well and the rest of the formation is still saturated with brine. The synthetic seismogram and time histories are shown in Figure 4.8 (a) and (b), respectively. The solid and dashed lines correspond to the receivers located at 330 m and 430 m and indicated with a letter V in the figure. The events correspond to the four sources whose snapshots are displayed in Figure 4.6. Figure 4.9 shows the time histories recorded at receivers 1 (left) and 2 (right) shown in Figure 4.8, where we have assumed lossless media, i.e., $Q_\nu = \infty$. The corresponding simulation in the lossy case is displayed in Figure 4.10, where it is clear that the wavefield has been attenuated and some events can be too weak to be detected. The P and S events of the 58 sources and the reverberations in the layer can be observed in these seismic traces.

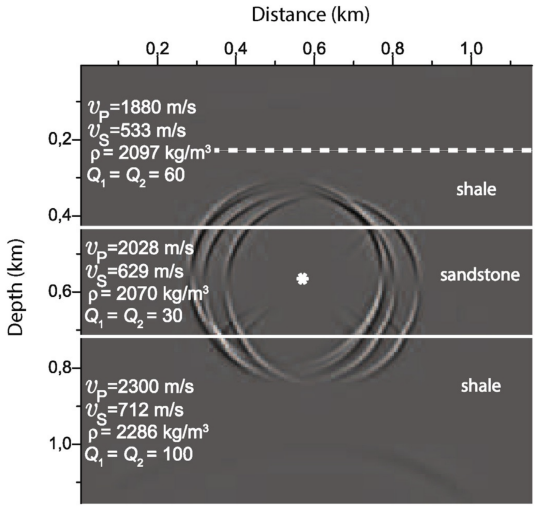

Figure 4.6: Geological model and snapshot at 3000.05 s, where three shear sources and one tensile source are active. The unrelaxed velocities, density and loss parameters are shown. The star indicates the injection point and the dashed line represents the receivers.

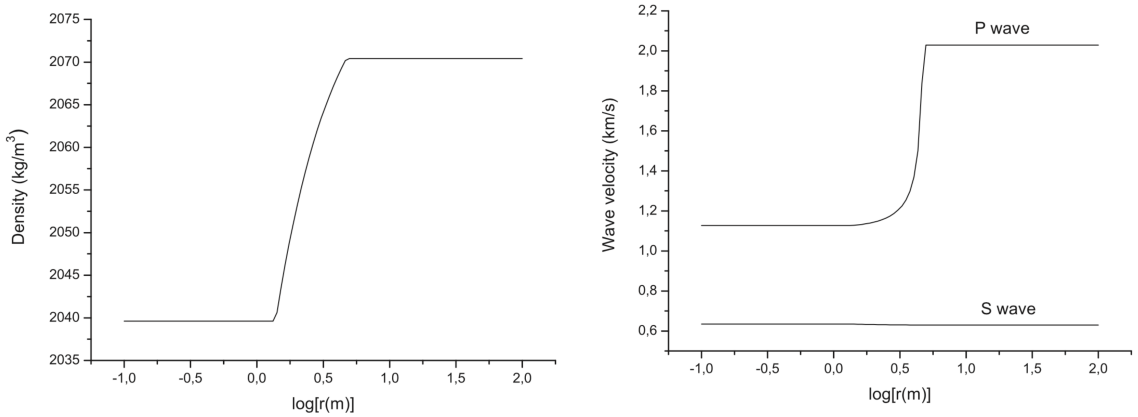

(a) Density

(b) Wave velocity

Figure 4.7: Unrelaxed wave velocities and density as a function of the radial distance at 3000 s from the onset of injection.

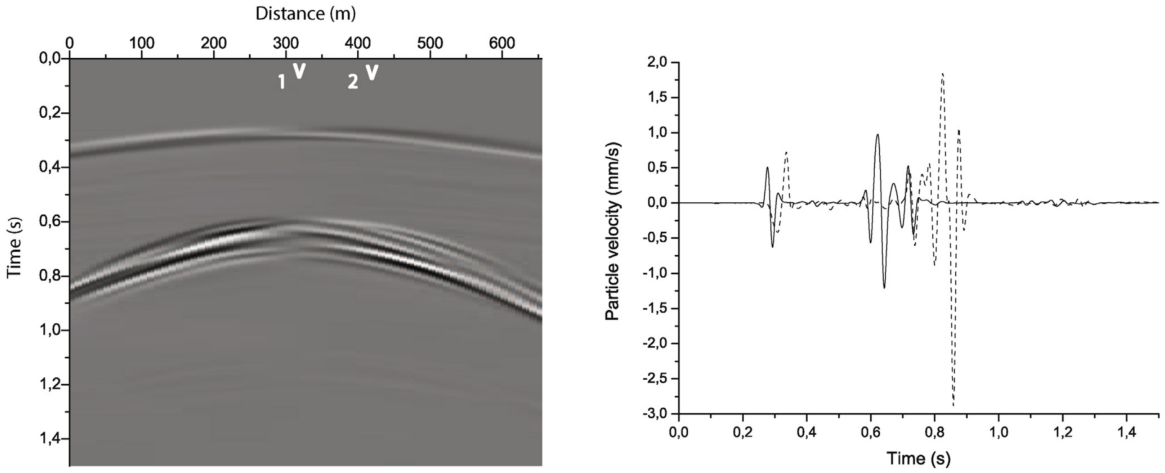

(a) Synthetic Seismogram

(b) Time History

Figure 4.8: Synthetic seismogram (a) and time history at the two receivers indicated with a V letter (b); receiver 1 (solid line) and receiver 2 (dashed line).

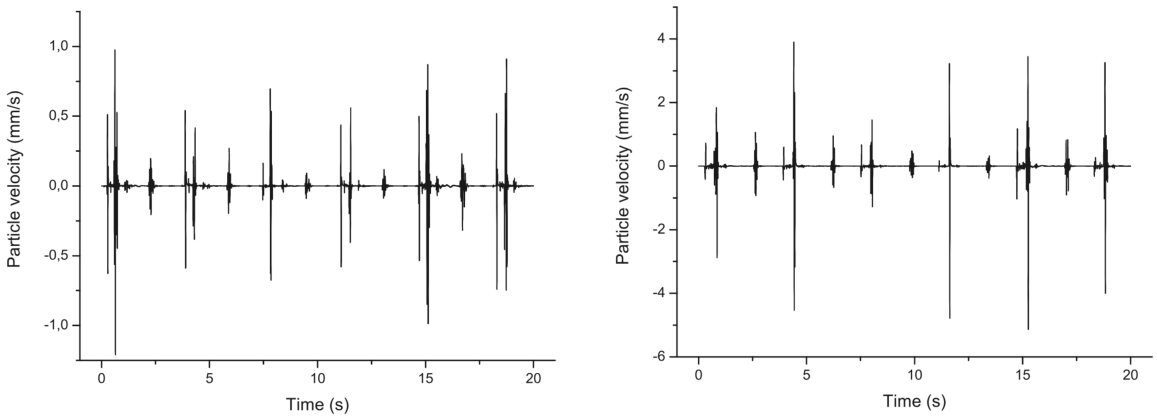

(a) Receiver 1

(b) Receiver 2

Figure 4.9: Time histories recorded at receivers 1(a) and 2(b) shown in Figure 4.8. The media are lossless.

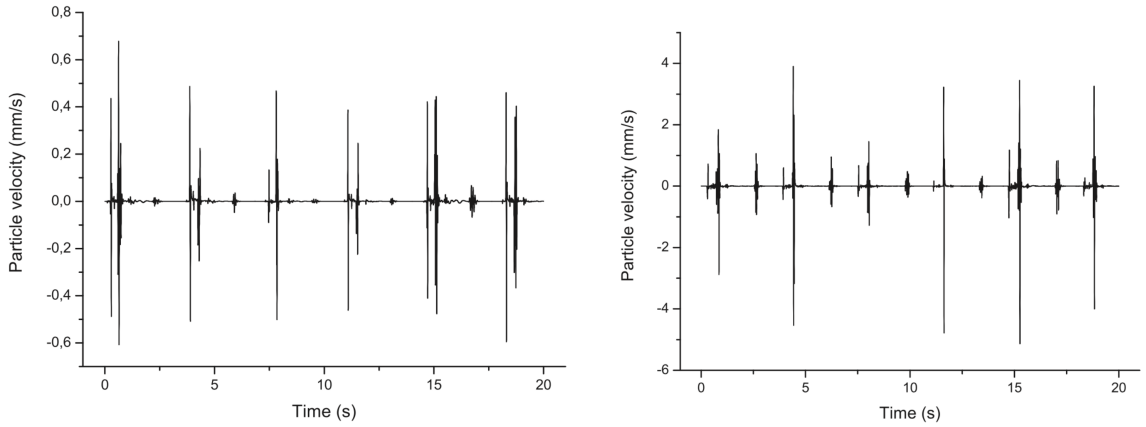

(a) Receiver 1 (b) Receiver 2

Figure 4.10: Time histories recorded at receivers 1 (a) and 2 (b) shown in Figure 4.8. The media are lossy.

4.4 Seismic Imaging: Reverse-time Migration

Modeling is essential to map the location of the sources. Here, we briefly outline a possible method based on reverse-time migration (for instance, McMechan (1982)) and an imaging condition, that we shall develop in a future work in more detail. To illustrate the method, we assume that the P and S wave fields have been separated. We note that the wave equation given in section 2.4.1 cannot be back propagated with ease due to the presence of seismic attenuation. First, it is difficult to obtain an attenuation model from seismic data with enough accuracy to correct for amplitude loss and velocity dispersion. Second, that equation is not time reversible, although there are a few techniques based on Q compensation to deal with seismic loss in migration algorithms, e.g. Zhu et al. (2014).
A time-reversible 2D elastic wave equation is the impedance-matching equation

$$\begin{aligned}\ddot{v}_x &= c_P \partial_x c_P \left(\partial_x v_x + \partial_z v_z\right) - 2 c_S \partial_x c_S \partial_z v_z + c_S \partial_z c_S \left(\partial_z v_x + \partial_x v_z\right), \\ \ddot{v}_z &= c_P \partial_z c_P \left(\partial_x v_x + \partial_z v_z\right) - 2 c_S \partial_z c_S \partial_x v_x + c_S \partial_x c_S \left(\partial_z v_x + \partial_x v_z\right),\end{aligned} \tag{4.39}$$

Carcione et al. (1994), where∂_i is the spatial derivative with respect to x_i and c_P and c_S are the P- and S-wave velocities. Since each discontinuity at the subsurface can generate unwanted secondary fields, it is desirable to suppress these effects. Equation 4.39 is the result of using the density as a parameter so that there is no discontinuity in acoustic impedance.
If the wave field can be separated into P and S waves (e.g., Robertsson and Curtis (2002)), so that these fields can be migrated separately, the wave equation for each mode is

$$\ddot{\psi} = c \left(\partial_x c \partial_x + \partial_z \partial_z\right) \psi \tag{4.40}$$

(Carcione et al. (2003a) Gajewski and Tessmer (2005)) where c is the wave velocity, which may correspond to P waves or to S waves.
The discretization of Equation 4.40 in a uniform mesh with square cells and based on an $O(2, \infty)$-scheme is

$$\frac{\psi_{i,j}^{n+1} - 2\psi_{i,j}^{n} + \psi_{i,j}^{n-1}}{dt^2} = c\left(\partial_x c \partial_x + \partial_z c \partial_z\right)\psi \tag{4.41}$$

(e.g. Abramowitz and Stegun (1964)), where $t = ndt$ and the spatial derivatives are computed with the Fourier pseudospectral method, as in section 2.4.2 (Baysal et al. (1983)).
Back-propagation is performed from Equation 4.41 as

$$\psi_{i,j}^{n-1} = 2\psi_{i,j}^{n} - \psi_{i,j}^{n+1} + cdt^2\left(\partial_x c \partial_x - \partial_z z \partial_z\right)\psi \tag{4.42}$$

The elastic wave Equation 4.39 can easily be discretized and its back-propagation version obtained in the same manner. In the migration process, the seismogram is a time-dependent boundary condition in Equation 4.42. The time step dt is equal to the sample rate of the data. The seismic trace is applied at each receiver in reverse time and the propagation goes back in time until the origin time, where the best focusing occurs. The reverse modeling sums the energy of all receivers, enhancing the signal-to-noise ratio. The imaging condition is that of Gajewski and Tessmer (2005), i.e., the origin times of the events are given by the time where maximum focusing (maximum amplitude) occurs. In our case, this is performed for each grid point of the mesh and we choose a number of sources whose relative amplitudes exceed a given threshold. The problem is that the sources are not synchronous. A simple method applied here considers the maximum amplitudes at the grid as a function of the back propagation time.
Let us consider a simple example consisting in three sources of dissimilar strength activated at different onset times. The mesh has 220 x 220 points with grid spacing of 10 m along the horizontal and vertical directions. The seismic velocity model consists of a layer with a velocity of 2 km/s embedded in a background medium of velocity 2.5 km/s. The source central frequency is f_p = 25 Hz and $t_s = 1.2/f_p$. The forward modeling uses dt = 1 ms and the field is propagated 0.8 s and recorded at a horizontal line of receivers at 300 m depth. Figure 4.11 shows a snapshot at 320 ms (a) and the seismogram (b), where we can see that each source is activated at different times. Each source has a different strength: in relative terms it is 1.2 (source 1), 1 (source 2) and 1.5 (source 3). In Figure 4.11a, from left to right the source-onset times have a delay of 0, 160 ms and 100 ms, while their maxima have a delay of 49, 209 and 149 ms, respectively, where 49 is t_s /dt (see Equation 4.38). Then, a proper imaging of each source occurs by back propagating (800 - 49) ms = 751 ms (source 1), (800 - 209) ms = 591ms (source 2) and (800 - 149) ms = 651 ms (source 3), where 800 ms is the maximum propagation time of the seismogram.

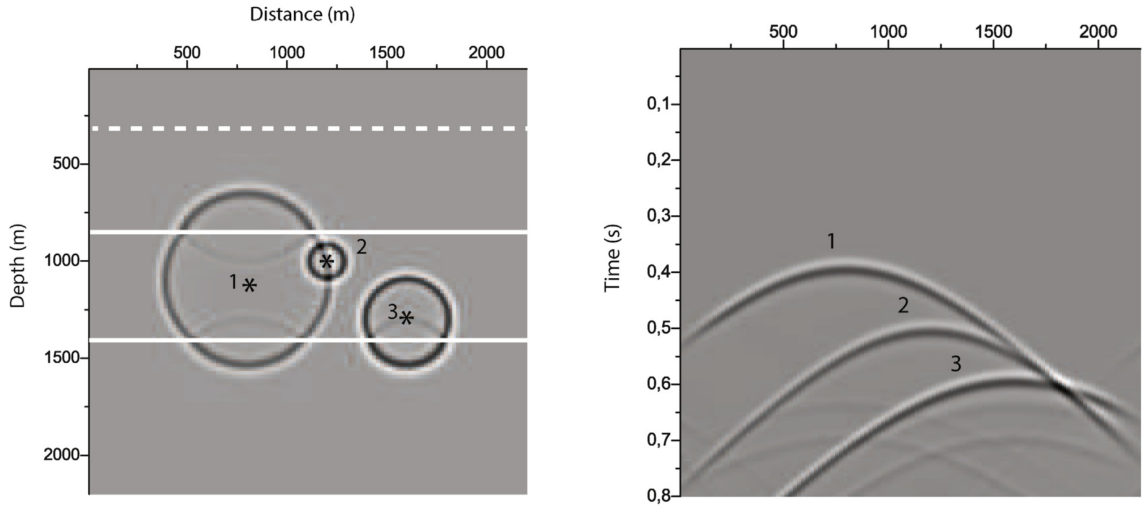

(a) Snapshot

(b) Seismogram

Figure 4.11: Snapshot (a) and seismogram (b) corresponding to three sources activated at different onsets. The location of the sources is indicated by stars and the seismic events are labeled by the source that has generated them. The dashed lines are the receivers.

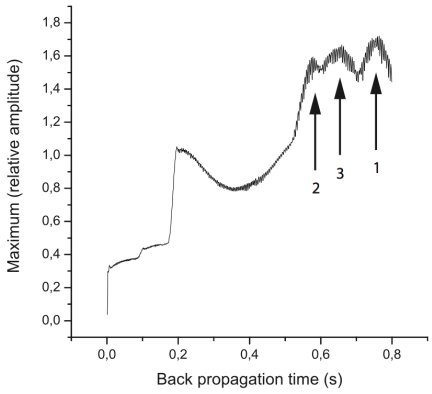

Figure 4.12: Wave field maxima at the images obtained by reverse-time migration as a function of the back propagation time. The numbers correspond to the sources in Figure 4.11

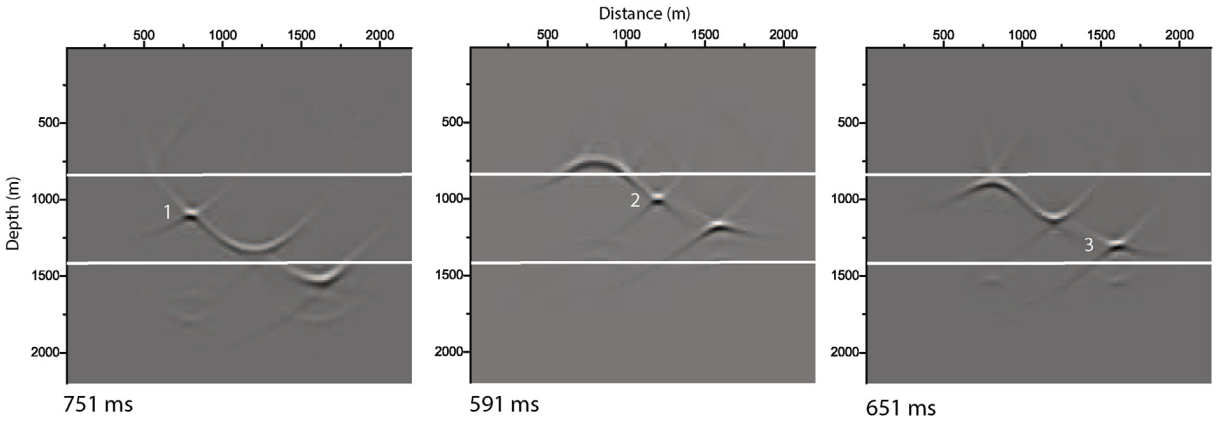

Figure 4.13: Reverse-time migration images at different back propagation times,where the wave field has been focused at each source location.The numbers indicate the sources.

We represent in Figure 4.12 the maximum amplitudes of the images as a function of the back propagation times, where the three maxima correspond to the sources. The maxima occur at the grid points where the sources were implemented. The reverse-time migration images are shown in Figure 4.13. The source numbers and propagation times for an optimal focusing are indicated. It is clear that when the wave field is focused almost at a point, a source has been located. The method is far from being perfect since wave-field constructive interference can enhance the amplitudes at some points where no source is present. Therefore, this imaging method can miss some sources of the CO_2 cloud. A pattern recognition algorithm (Joswig (1990)), or an alternative technique, as for instance, seismic interference (Sava (2011)), could be used in addition to determine the source locations.

Conclusions

In the first chapter of this thesis, we gave a motivation to the project. In fact, climate change and its effects on our planet are one of the main challenges mankind will have to face in the coming decades. It is essential to implement policies which reduce carbon emissions from industrial activities, energy production and transportation. However, since hydrocarbons are and still will be in the foreseeable future the main source of energy, an effective reduction in carbon emissions is most likely not economically viable. Therefore, other strategies to mitigate the effects of the excessive carbon have been explored; one of the most promising ones is storing carbon dioxide in geological repositories. In particular, deep saline aquifers offer the largest storage capacity, as the interaction between the supercritical CO_2 and the brine gives place to unique trapping mechanisms which allow very large amounts of carbon dioxide to stay stored for very long periods of time.

In Chapter 2, we presented the theory of two-phase flow, under the Darcy approximation, used to describe the propagation of the CO_2 in the brine. In all numerical experiments presented further in the thesis, rocks composed of a mixture of quartz and clay grains are considered. Their hydraulic properties are well described by the Van Genuchten model for capillary pressure- and relative permeability-saturation relations. Simulations were run using a finite-difference commercial simulator, called STOMP, to assess its ability to describe all three main trapping mechanisms occurring in the first few years after the onset of injection. The structural trapping occurs when a seal forbids the buoyant carbon dioxide to migrate upwards. Capillary trapping happens after the end of the injection, when the brine invades the CO_2 plume, isolating part of it in ganglia. Finally, dissolution trapping occurs a few decades after the onset of injection, when the CO_2 dissolves in the brine by molecular diffusion, increasing its density and giving place to a convective instability. In fact, the higher density fluid tends to fall to the bottom of the formation in the form of fingers.

Time-lapse monitoring of the CO_2 is essential to assess whether there is the chance of any leakages in the caprock. To do this, we use seismic techniques, since the presence of the CO_2 changes the elastic properties of the medium and therefore P- and S- wave velocities and attenuation factors. In the last section of this chapter we present the full-wave solver with which we compute the synthetic seismograms. Anelasticity is described by introducing memory variables, which are related to the relaxation times of a standard linear solid, in the velocity-strain

relations.
In Chapter 3 we present a synthetic, yet realistic, example of monitoring with a cross-hole seismic setup. The geologic formation considered is a heterogenous sandstone aquifer with shaly intrusions embedded in shaly mudstone. Two wells are drilled, 150 m apart where sources and receivers al located.
We inject CO_2 for one year, simulating its propagation with STOMP commercial software. The effects of the presence of CO_2 on the elastic properties of the medium are modeled with White's mesoscopic theory, which allows to compute P-wave velocities and attenuation factors from the porosity, permeability and clay content of the rock, together with the viscosity of the two fluids as output by STOMP. Since White's theory does not account for attenuation of shear waves, we computed these using a Zener module. Based on the output of White's model, we assessed that the seismic velocity anomalies due to the presence of the CO_2 are large enough to be detected with seismic tomography of direct waves. We computed synthetic cross-hole seismograms using the full-wave solver outlined in Chapter 2. After picking the first arrivals, we perform a traveltime tomography which successfully maps the main velocity anomalies.
in Chapter 4 we presented a simple model to monitor the propagation of the CO_2 plume by finding the location of the micro-earthquakes generated by the overpressure. We consider a homogenous sandstone aquifer, in which a constant rate of pure CO_2 is injected for one hour. Under the main assumption that the two fluids are immiscible and that capillary pressure can be neglected, the fluid flow was simulated with a semi-analytical solution which describes the pressure build-up in the formation and the location of the brine-CO_2 interface as a function of radial distance from the well. Based on the stiffness of the medium, we then computed an average threshold pore pressure, above which the pore will fail, emitting seismic energy. We then distributed the values of the threshold pressure fractally on the grid and we were therefore able to compute the location of the emitting points. Furthermore, the hydraulic diffusivity of the medium was obtained from the envelope of events by representing the distance of the events to the injection point as a function of the emission times. The seismic velocities were computed using Wood's equation, which does not account for attenuation. In these simulation, the quality factors are therefore assumed.
The moment tensors of the sources were then computed, considering only pure shear and tensile emissions and intensity proportional to the difference between the pore pressure and the failure pressure. Modelling of the seismic emissions was performed using the same viscoelastic modelling code presented in Chapter 2 . Finally, the seismic energy produced by the asynchronous sources is redatumed back to the emitting points by means of a reverse-time migration algorithm. The location of these emitting points approximates the position of the CO_2 plume.

The success of these methodologies is subject to a correct description of the physical phenomena involved and use of geophysical methods. In fact, the aim of this thesis was to assess

whether we acquired sufficient knowledge to correctly describe all steps of a carbon storage experiment. We can therefore affirm that, in the next future, we are ready to apply these techniques to real data.

Aknowledgments

I miei ringraziamenti vanno innanzitutto ai colleghi Flavio Accaino e Walter Bohm. Il primo, per il supporto con seismic unix e per avermi insegnato l'arte della polemica; il secondo per il grande aiuto che mi ha dato per fare la tomografia. Un grande ringraziamento va anche ai miei compagni di dottorato Valeria, Chiara e Michele, che mi hanno sempre comunicato tempestivamente richieste della segreteria o burocratiche, su cui sono notoriamente abbastanza distratto. L'esperienza piú bella nel corso del dottorato é stata senz'altro la missione sull'OGS Explora a largo di Malta, a cui sono stato invitato a partecipare da Angelo Camerlenghi.
Il flusso a due fasi coinvolge della fisica non proprio intuitiva. Se ne sono venuto fuori é grazie a Diogo Bolster che nel corso di una summer school in Corsica, mentre gli altri si godevano il meritato riposo in spiaggia, si intratteneva con me e COMSOL per lunghe ore.
Ringrazio poi naturalmente la mia famiglia, che mi ha sopportato e tirato su nei tanti, tantissimi momenti di frustrazione e sconforto. Un grazie del tutto speciale va a Francesca, che mi sopporta proprio sempre e si prende il peggio di me, lamentandosi il giusto.

Bibliography

Abramowitz, M. and Stegun, I. A. (1964). *Handbook of mathematical functions: with formulas, graphs, and mathematical tables*, volume 55. Courier Corporation.

Accaino, F., Böhm, G., and Tinivella, U. (2005). Tomographic inversion of common image gathers. *First Break*, 23(3):39–44.

Angus, D. and Verdon, J. (2013). Using microseismicity to estimate formation permeability for geological storage of co 2. *ISRN Geophysics*, 2013.

Arendt, A., Bolch, T., Cogley, J., Gardner, A., Hagen, J., Hock, R., Kaser, G., Pfeffer, W., Moholdt, G., Paul, F., et al. (2012). Randolph glacier inventory [v2. 0]: A dataset of global glacier outlines, global land ice measurements from space, boulder colorado, usa. *Digital Media*.

Arts, R., Chadwick, A., Eiken, O., Thibeau, S., and Nooner, S. (2008). Ten years' experience of monitoring co2 injection in the utsira sand at sleipner, offshore norway. *First Break*, 26:65–72.

Arts, R., Eiken, O., Chadwick, A., Zweigel, P., Van der Meer, L., and Zinszner, B. (2004). Monitoring of co 2 injected at sleipner using time-lapse seismic data. *Energy*, 29(9):1383–1392.

Baysal, E., Kosloff, D. D., and Sherwood, J. W. (1983). Reverse time migration. *Geophysics*, 48(11):1514–1524.

Bennion, D. B., Bachu, S., et al. (2006). Supercritical co2 and h2s-brine drainage and imbibition relative permeability relationships for intercrystalline sandstone and carbonate formations. In *SPE Europec/EAGE Annual Conference and Exhibition*. Society of Petroleum Engineers.

Bohm, G. (2012). Cat 3d user manual: Version 4.0. Technical report, National Institute of Oceanography and Experimental Geophysics, Trieste, Italy.

Böhm, G. and Vesnaver, A. L. (1999). In quest of the grid. *Geophysics*, 64(4):1116–1125.

Bonan, G. B. (2008). Forests and climate change: forcings, feedbacks, and the climate benefits of forests. *science*, 320(5882):1444–1449.

Bromhal, G. S., Sams, W. N., Jikich, S., Ertekin, T., and Smith, D. H. (2005). Simulation of co 2 sequestration in coal beds: The effects of sorption isotherms. *Chemical Geology*, 217(3):201–211.

Brooks, R. H. and Corey, A. T. (1964). Hydraulic properties of porous media and their relation to drainage design. *Trans. ASAE*, 7(1):26–0028.

Bruant, R., Guswa, A., Celia, M., and Peters, C. (2002). Safe storage of co2 in deep saline aquifers. *Environmental Science and Technology- Washington DC*, 36(11):240A–245A.

Bruce, R. (1972). Hydraulic conductivity evaluation of the soil profile from soil water retention relations. *Soil Science Society of America Journal*, 36(4):555–561.

Carcione, J., Böhm, G., and Marchetti, A. (1994). Simulation of a cmp seismic section. *Journal of Seismic Exploration*, 3(4):381–396.

Carcione, J. M. (2015). *Wave fields in real media: Wave propagation in anisotropic, anelastic, porous and electromagnetic media*, volume 38. Elsevier.

Carcione, J. M., Finetti, I. R., and Gei, D. (2003a). Seismic modeling study of the earth's deep crust. *Geophysics*, 68(2):656–664.

Carcione, J. M. and Gei, D. (2009). Theory and numerical simulation of fluid-pressure diffusion in anisotropic porous media. *Geophysics*, 74(5):N31–N39.

Carcione, J. M., Gei, D., Picotti, S., and Michelini, A. (2012). Cross-hole electromagnetic and seismic modeling for co 2 detection and monitoring in a saline aquifer. *Journal of petroleum science and engineering*, 100:162–172.

Carcione, J. M., Gurevich, B., and Cavallini, F. (2000). A generalized biot–gassmann model for the acoustic properties of shaley sandstones. *Geophysical Prospecting*, 48(3):539–557.

Carcione, J. M., Helle, H. B., and Pham, N. H. (2003b). White's model for wave propagation in partially saturated rocks: Comparison with poroelastic numerical experiments. *Geophysics*, 68(4):1389–1398.

Carcione, J. M., Kosloff, D., and Kosloff, R. (1988). Wave propagation simulation in a linear viscoelastic medium. *Geophysical Journal International*, 95(3):597–611.

Carcione, J. M., Picotti, S., Gei, D., and Rossi, G. (2006). Physics and seismic modeling for monitoring co2 storage. *Pure and Applied Geophysics*, 163(1):175–207.

Chadwick, R., Zweigel, P., Gregersen, U., Kirby, G., Holloway, S., and Johannessen, P. (2004). Geological reservoir characterization of a co 2 storage site: the utsira sand, sleipner, northern north sea. *Energy*, 29(9):1371–1381.

Chavent, G. and Jaffré, J. (1986). *Mathematical models and finite elements for reservoir simulation: single phase, multiphase and multicomponent flows through porous media*. Elsevier.

Christopher, C. A., Iliffe, J., and Americas, B. (2006). Reservoir seals: How they work and how to choose a good one. In *CO2SC Symposium, Lawrence Berkeley National Laboratory, Berkeley, California*.

Darcy, H. (1856). *Les fontaines publiques de la ville de Dijon: exposition et application...* Victor Dalmont.

Daugherty, J. and Urbancic, T. (2009). Passive microseismics: a valuable technique for monitoring co 2 injections. In *AAPG Hedberg Conference Geological Carbon Sequestration: Prediction and Verification, Vancouver, BC, Canada*.

David, E. and Zimmerman, R. W. (2011). Elastic moduli of solids containing spheroidal pores. *International Journal of Engineering Science*, 49(7):544–560.

Ennis-King, J., Preston, I., and Paterson, L. (2005a). Onset of convection in anisotropic porous media subject to a rapid change in boundary conditions. *Physics of Fluids (1994-present)*, 17(8):084107.

Ennis-King, J. P., Paterson, L., et al. (2005b). Role of convective mixing in the long-term storage of carbon dioxide in deep saline formations. *Spe Journal*, 10(03):349–356.

Falkowski, P., Scholes, R., Boyle, E., Canadell, J., Canfield, D., Elser, J., Gruber, N., Hibbard, K., Högberg, P., Linder, S., et al. (2000). The global carbon cycle: a test of our knowledge of earth as a system. *Shaascience*, 290(5490):291–296.

Friedmann, S. J. (2007). Site characterization and selection guidelines for geological carbon sequestration. In *UCRL-TR-234408*, pages 1–27. University of California, Lawrence Livermore National Laboratory.

Gajewski, D. and Tessmer, E. (2005). Reverse modelling for seismic event characterization. *Geophysical Journal International*, 163(1):276–284.

Gangi, A. F. and Carlson, R. L. (1996). An asperity-deformation model for effective pressure. *Tectonophysics*, 256(1-4):241–251.

Haas, J. and John, L. (1976). Thermodynamics properties of the coexisting phases and thermochemical properties of the nacl component in boiling nacl solutions. *US, Geol. Surv., Bull.*, 1421.

Haldorsen, J. B., Brooks, N. J., and Milenkovic, M. (2013). Locating microseismic sources using migration-based deconvolution. *Geophysics*, 78(5):KS73–KS84.

Hashin, Z. and Shtrikman, S. (1963). A variational approach to the theory of the elastic behaviour of multiphase materials. *Journal of the Mechanics and Physics of Solids*, 11(2):127–140.

Holliger, K. (1997). Seismic scattering in the upper crystalline crust based on evidence from sonic logs. *Geophysical Journal International*, 128(1):65–72.

Holloway, S. (2001). Storage of fossil fuel-derived carbon dioxide beneath the surface of the earth. *Annual Review of Energy and the Environment*, 26(1):145–166.

Hubbert, M. and Willis, D. (1957). Mechanics of hydraulic fracturing: Aime petroleum trans., v. 210. disc.

Hummel, N. and Shapiro, S. (2012). Microseismic estimates of hydraulic diffusivity in case of non-linear fluid-rock interaction. *Geophysical Journal International*, 188(3):1441–1453.

Hunt, J. R., Sitar, N., and Udell, K. S. (1988). Nonaqueous phase liquid transport and cleanup: 2. experimental studies. *Water Resources Research*, 24(8):1259–1269.

Jain, M., Iyengar, S., and Subramanyam, G. (1984). Variable mesh methods for the numerical solution of two-point singular perturbation problems. *Computer methods in applied mechanics and engineering*, 42(3):273–286.

Joswig, M. (1990). Pattern recognition for earthquake detection. *Bulletin of the Seismological Society of America*, 80(1):170–186.

Juanes, R., EJ, S., FM, O., and MJ, B. (2006). Impact of relative permeability hysteresis on geological co2 storage. *Water Resources Research*, 42(12).

Kovscek, A. and Wang, Y. (2005). Geologic storage of carbon dioxide and enhanced oil recovery. i. uncertainty quantification employing a streamline based proxy for reservoir flow simulation. *Energy Conversion and Management*, 46(11):1920–1940.

Kumar, A., Noh, M. H., Ozah, R. C., Pope, G. A., Bryant, S. L., Sepehrnoori, K., Lake, L. W., et al. (2005). Reservoir simulation of co 2 storage in aquifers. *Spe Journal*, 10(03):336–348.

Kundu, P. and Cohen, I. (2004). Fluid mechanics, 759 pp.

Kunze, R., Uehara, G., and Graham, K. (1968). Factors important in the calculation of hydraulic conductivity. *Soil Science Society of America Journal*, 32(6):760–765.

Land, C. S. (1968). Calculation of imbibition relative permeability for two- and three-phase flow from rock properties. *Society of Petroleum Engineers Journal*, 8(2):149–156.

Langenbruch, C. and Shapiro, S. (2014). Gutenberg-richter relation originates from coulomb stress fluctuations caused by elastic rock heterogeneity. *Journal of Geophysical Research: Solid Earth*, 119(2):1220–1234.

Le Ravalec, M. and Guéguen, Y. (1996). High-and low-frequency elastic moduli for a saturated porous/cracked rock-differential self-consistent and poroelastic theories. *Geophysics*, 61(4):1080–1094.

Martínez-Garzón, P., Bohnhoff, M., Kwiatek, G., Zambrano-Narváez, G., and Chalaturnyk, R. (2013). Microseismic monitoring of co2 injection at the penn west enhanced oil recovery pilot project, canada: Implications for detection of wellbore leakage. *Sensors*, 13(9):11522–11538.

Matear, R. J. and Elliott, B. (2004). Enhancement of oceanic uptake of anthropogenic co2 by macronutrient fertilization. *Journal of Geophysical Research: Oceans*, 109(C4).

Mathias, S. A., de Miguel, G. J. G. M., Thatcher, K. E., and Zimmerman, R. W. (2011). Pressure buildup during co2 injection into a closed brine aquifer. *Transport in porous media*, 89(3):383–397.

Mathias, S. A., Hardisty, P. E., Trudell, M. R., and Zimmerman, R. W. (2009). Approximate solutions for pressure buildup during co2 injection in brine aquifers. *Transport in Porous Media*, 79(2):265–284.

McMechan, G. A. (1982). Determination of source parameters by wavefield extrapolation. *Geophysical Journal International*, 71(3):613–628.

Meyer, C., McClintock, R., Silvestri, G., and Spencer, R. (1993). Asme steam tables: thermodynamic and transport properties of steam. *American Society of Mechanical Engineers, New York*.

Millington, R. and Quirk, J. (1961). Permeability of porous solids. *Transactions of the Faraday Society*, 57:1200–1207.

Moore, J. C., Battino, R., Rettich, T. R., Handa, Y. P., and Wilhelm, E. (1982). Partial molar volumbes of gases at infinite dilution in water at 298.15 k. *Journal of Chemical and Engineering Data*, 27(1):22–24.

Mualem, Y. (1976a). Hysteretical models for prediction of the hydraulic conductivity of unsaturated porous media. *Water resources research*, 12(6):1248–1254.

Mualem, Y. (1976b). A new model for predicting the hydraulic conductivity of unsaturated porous media. *Water resources research*, 12(3):513–522.

Nutting, P. G. (1930). Physical analysis of oil sands. *AAPG Bulletin*, 14(10):1337–1349.

Oak, M. et al. (1990). Three-phase relative permeability of water-wet berea. In *SPE/DOE Enhanced Oil Recovery Symposium*. Society of Petroleum Engineers.

Oye, V., Aker, E., Daley, T. M., Kühn, D., Bohloli, B., and Korneev, V. (2013). Microseismic monitoring and interpretation of injection data from the in salah co 2 storage site (krechba), algeria. *Energy Procedia*, 37:4191–4198.

Palmer, I., Mansoori, J., et al. (1996). How permeability depends on stress and pore pressure in coalbeds: a new model. In *SPE Annual Technical Conference and Exhibition*. Society of Petroleum Engineers.

Peaceman, D. W. (2000). *Fundamentals of numerical reservoir simulation*, volume 6. Elsevier.

Pennebaker, E. et al. (1968). An engineering interpretation of seismic data. In *Fall Meeting of the Society of Petroleum Engineers of AIME*. Society of Petroleum Engineers.

Pentland, C. H., El-Maghraby, R., Iglauer, S., and Blunt, M. J. (2011). Measurements of the capillary trapping of super-critical carbon dioxide in berea sandstone. *Geophysical Research Letters*, 38(6).

Picotti, S., Carcione, J. M., Rubino, J. G., Santos, J. E., and Cavallini, F. (2010). A viscoelastic representation of wave attenuation in porous media. *Computers & Geosciences*, 36(1):44–53.

Pride, S. R., Berryman, J. G., and Harris, J. M. (2004). Seismic attenuation due to wave-induced flow. *Journal of Geophysical Research: Solid Earth*, 109(B1).

Pruess, K. (2011). Eco2m: a tough2 fluid property module for mixtures of water, nacl, and co2, including super-and sub-critical conditions, and phase change between liquid and gaseous co2. *Lawrence Berkeley National Laboratory*.

Pruess, K. and Garcia, J. (2002). Multiphase flow dynamics during co2 disposal into saline aquifers. *Environmental Geology*, 42(2-3):282–295.

Pruess, K., Oldenburg, C., and Moridis, G. (1999). Tough2 user's guide version 2. *Lawrence Berkeley National Laboratory*.

Robertsson, J. O. and Curtis, A. (2002). Wavefield separation using densely deployed three-component single-sensor groups in land surface-seismic recordings. *Geophysics*, 67(5):1624–1633.

Rothert, E. and Shapiro, S. A. (2003). Microseismic monitoring of borehole fluid injections: Data modeling and inversion for hydraulic properties of rocks. *Geophysics*, 68(2):685–689.

Rozhko, A. Y. (2010). Role of seepage forces on seismicity triggering. *Journal of Geophysical Research: Solid Earth*, 115(B11).

Rutqvist, J., Birkholzer, J., and Tsang, C.-F. (2008). Coupled reservoir–geomechanical analysis of the potential for tensile and shear failure associated with co 2 injection in multilayered reservoir–caprock systems. *International Journal of Rock Mechanics and Mining Sciences*, 45(2):132–143.

Sava, P. (2011). Micro-earthquake monitoring with sparsely sampled data. *Journal of Petroleum Exploration and Production Technology*, 1(1):43–49.

Shapiro, S. and Dinske, C. (2009). Scaling of seismicity induced by nonlinear fluid-rock interaction. *Journal of Geophysical Research: Solid Earth*, 114(B9).

Shapiro, S. A. (2003). Elastic piezosensitivity of porous and fractured rocks. *Geophysics*, 68(2):482–486.

Shapiro, S. A., Huenges, E., and Borm, G. (1997). Estimating the crust permeability from fluid-injection-induced seismic emission at the ktb site. *Geophysical Journal International*, 131(2):F15–F18.

Shi, J. and Durucan, S. (2005). Co2 storage in deep unmineable caol seams. *Oil & gas science and technology*, 60(3):547–558.

Smetacek, V., Klaas, C., Strass, V. H., Assmy, P., Montresor, M., Cisewski, B., Savoye, N., Webb, A., d'Ovidio, F., Arrieta, J. M., et al. (2012). Deep carbon export from a southern ocean iron-fertilized diatom bloom. *Nature*, 487(7407):313–319.

Sminchak, J., Gupta, N., Byrer, C., and Bergman, P. (2002). Issues related to seismic activity induced by the injection of co2 in deep saline aquifers. *Journal of Energy & Environmental Research*, 2:32–46.

Span, R. and Wagner, W. (1996). A new equation of state for carbon dioxide covering the fluid region from the triple-point temperature to 1100 k at pressures up to 800 mpa. *Journal of physical and chemical reference data*, 25(6):1509–1596.

Spycher, N., Pruess, K., and Ennis-King, J. (2003). Co2- h2o mixtures in the geological sequestration of co 2. i. assessment and calculation of mutual solubilities from 12 to 100 c and up to 600 bar. *Geochimica et cosmochimica acta*, 67(16):3015–3031.

Stanchits, S., Mayr, S., Shapiro, S., and Dresen, G. (2011). Fracturing of porous rock induced by fluid injection. *Tectonophysics*, 503(1):129–145.

Stewart, R. R. (1991). *Exploration seismic tomography: Fundamentals*. Society of Exploration Geophysicists.

Tignor, K., Allen, M., Boschung, S., Nauels, J., Xia, A., Bex, Y., Midgley, V., and Eds, P. (2013). The physical science basis. contribution of working group i to the fifth assessment report of the intergovernmental panel on climate change. *Change, IPCC Climate*, page 1535.

Urbancic, T., Daugherty, J., and Baig, A. (2009). Microseismic monitoring of a carbon sequestration field test. In *AGU Fall Meeting Abstracts*, volume 1, page 07.

Van Genuchten, M. T. (1980). A closed-form equation for predicting the hydraulic conductivity of unsaturated soils. *Soil science society of America journal*, 44(5):892–898.

Vavryčuk, V. (2011). Tensile earthquakes: Theory, modeling, and inversion. *Journal of Geophysical Research: Solid Earth*, 116(B12).

Vesnaver, A. and Böhm, G. (2000). Staggered or adapted grids for seismic tomography? *The Leading Edge*, 19(9):944–950.

Vesnaver, A., Lovisa, L., and Böhm, G. (2010). Joint 3d processing of active and passive seismic data. *Geophysical Prospecting*, 58(5):831–844.

Vesnaver, A. L., Böhm, G., Madrussani, G., Petersen, S., and Rossi, G. (1999). Tomographic imaging by reflected and refracted arrivals at the north sea. *Geophysics*, 64(6):1852–1862.

White, J. (1975). Computed seismic speeds and attenuation in rocks with partial gas saturation. *Geophysics*, 40(2):224–232.

White, M. D., Bacon, D. H., McGrail, B. P., Watson, D. J., White, S. K., and Zhang, Z. (2012). Stomp subsurface transport over multiple phases: Stomp-co2 and stomp-co2e guide: Version 1.0. Technical report, Pacific Northwest National Laboratory (PNNL), Richland, WA (US).

Zener, C. (1948). *Elasticity and anelasticity of metals*. University of Chicago press.

Zhu, T., Harris, J. M., and Biondi, B. (2014). Q-compensated reverse-time migration. *Geophysics*, 79(3):S77–S87.

Zweigel, P., Arts, R., Lothe, A. E., and Lindeberg, E. B. (2004). Reservoir geology of the utsira formation at the first industrial-scale underground co2 storage site (sleipner area, north sea). *Geological Society, London, Special Publications*, 233(1):165–180.